Numerical modeling on thermal interaction between thermal plasma and solid powder for materials processing

メタデータ	言語: eng 出版者: 公開日: 2020-01-09 キーワード (Ja): キーワード (En): 作成者: メールアドレス: 所属:
URL	http://hdl.handle.net/2297/00056494

This work is licensed under a Creative Commons Attribution-NonCommercial-ShareAlike 3.0 International License.

DOCTORAL THESIS

NUMERICAL MODELING ON
THERMAL INTERACTION BETWEEN THERMAL PLASMA AND
SOLID POWDER FOR
MATERIAL PROCESSING

KANAZAWA UNIVERSITY
GRADUATE SCHOOL OF NATURAL SCIENCE AND TECHNOLOGY
ELECTRICAL ENGINEERING AND COMPUTER SCIENCE

STUDENT ID 1624042016

YULIANTA SIREGAR

SUPERVISERS
PROF. YASUNORI TANAKA
PROF. YOSHIHIKO UESUGI
PROF. TATSUO ISHIJIMA
Dr. YUSUKE NAKANO

JUNE, 2019

Contents

Acknowledgement xv

Chapter1 Introduction 1

1.1 Plasma state 1

1.1.1 Overview of plasma 1

1.1.2 Concept of temperature in a plasma 2

1.1.3 Different types of plasma by temperature 4

1.2 Inductively coupled thermal plasma torch 7

1.3 Objective of this thesis 9

1.4 Composition of the thesis 11

References in chapter 1 13

Chapter2 Influence of input power in Ar/H_2 thermal plasma with Si powder by simulation 17

2.1 Introduction 17

2.2 Configuration of Inductively Coupled Thermal Plasma torch 18

2.3 Modeling of the Inductively Coupled Thermal Plasma with Powder Injection 19

2.3.1 Modelling Assumptions 19

2.3.2 Governing equation 20

2.3.3 Calculation condition 22

2.4 Calculation results 24

2.4.1 The Temperature Distribution of Thermal Plasma 24

2.5 Summary of chapter 2 31

References in chapter 2 33

Chapter3 Numerical Parametric Investigation on Temperature Distribution in Ar/O_2 Induction Thermal Plasmas with Ti Powder Injection -Inclusion of Particle Evaporation- 37

3.1 Introduction 37
3.2 Configuration of inductively coupled thermal plasmatorch 39
3.3 Modeling 41
3.3.1 Assumptions 41
3.3.2 Governing equation for Ti particle 42
3.3.3 The drag force coefficient and heat transfer coefficient 44
3.3.4 The drag force coefficient and heat transfer coefficient 44
3.3.5 Governing equation for thermal plasma region 45
3.3.6 Interaction between Ti particle and thermal plasma 47
3.3.7 Thermodynamic properties of Ar/O_2 mixture and Ti vapor 49
3.3.8 Calculation condition 53
3.4 Calculation results 56
3.4.1 Influence of operation parameters reduced to lower values 56
3.4.2 Influence of operation parameters increased to higher values 62
3.4.3 Particle behavior 68
3.5 Summary of chapter 3 73
References in chapter 3 75
Chapter4 Numerical study of temperature and gas flow fields in Ar-O_2 tandem-type inductively coupled thermal plasma with Ti feedstock powder injection 79
4.1 Introduction 79
4.2 Configuration of Tandem-coil Induction Thermal Plasma Torch 81
4.3 Modelling of Tandem-coil Induction Thermal Plasma 84
4.3.1 Modelling assumptions 84
4.3.2 Governing equation for Ti feed powder 85
4.3.3 Governing equation for tandem-coil induction thermal plasma . . . 88
4.3.4 Interaction between Ti particles and tandem coil thermal plasma . 90
4.3.5 Thermodynamic and transport properties of Ti bulk, Ar-O_2-Ti system 93
4.3.6 Boundary condition 94
4.3.7 Calculation conditions for single-frequency coil ICTP and tandem coil ICTP 102

4.4 Calculation Results 105
4.4.1 Temperature distribution of thermal plasma 105
4.4.2 Mass fraction distribution of titanium vapour and gas flow pattern . 123
4.4.3 Particle behaviour 132
4.5 Summary of chapter 4 137
References in chapter 4 139
Chapter5 Conclusions 143
5.1 Introduction 143
5.2 Summary of results 144
5.2.1 Influence of input power in Ar/H_2 thermal plasma with Si powder by simulation 144
5.2.2 Numerical Parametric Investigation on Temperature Distribution in Ar/O_2 Induction Thermal Plasmas with Ti Powder Injection-Inclusion of Particle Evaporation- 144
5.2.3 Numerical study of temperature and gas flow fields in Ar-O_2 tandem-type inductively coupled thermal plasma with Ti feedstock powder injection 145
5.3 Future researches 146

List of Figures

1.1 States of materials. 2
1.2 Maxwell-Boltzmann distribution of velocities in argon atom. 3
1.3 Classification of plasmas by electron temperature and electron density. . . 5
1.4 Configuration of ICTP torch. 6

2.1 Configuration of ICTP torch. 18
2.2 The temperature distribution of 99% Ar-1%H_2 ICTPs with Si powder injection at input powers of 20 kW, 30 kW, and 40 kW. 25
2.3 Radial temperature distribution of 99% Ar-1%H_2 ICTP at an axial position of 250 mm with Si powder injection. 26
2.4 Axial temperature distribution of 99% Ar-1%H_2 ICTP at an radial position of 5 mm with Si powder. 26
2.5 Diameter variation for 35 kinds of Si particles injected with different 7 initial diameters and 5 different initial positions as a function of axial position in 99% Ar-1%H_2 ICTPs. 28
2.6 Mass fraction distribution of 99% Ar-1%H_2 ICTPs with Si powder injection at input powers of 20 kW, 30 kW and 40 kW. 29
2.7 Streamlines in 99% Ar-1%H_2 ICTPs with Si powder injection at input powers of 20 kW, 30 kW, and 40 kW. 30

3.1 Configuration of inductively coupled thermal plasma torch used in the calculation. 40
3.2 Initial positions of particle injections and particle size distribution. 41
3.3 Molar fraction of thermal plasma in 90%Ar+10%O_2 at a pressure of 300 Torr. 50
3.4 Molar fraction of thermal plasma in 89%Ar+9%O_2 +9%Ti at a pressure of 300 Torr. 51

3.5 Specific heat at constant pressure for Ar-O_2 thermal plasma with Ti vapor at a pressure of 300 Torr. 51
3.6 Electrical conductivity for Ar-O_2 thermal plasma with Ti vapor at a pressure of 300 Torr. 52
3.7 Viscosity for Ar-O_2 thermal plasma with Ti vapor at a pressure of 300 Torr. 52
3.8 Temperature distribution of Ar-O_2 thermal plasma with Ti powder injection for reduced sheath gas flow rate (a), feedstock feeding rate (b), input power (c) from the reference condition at a pressure of 300 Torr. 57
3.9 Radial temperature distribution of Ar-O_2 thermal plasma with Ti powder injection at axial positions of 250 mm for reduced sheath gas flow rate (a), feedstock feeding rate (b), input power (c) from the reference condition. . . 58
3.10 Axial temperature distribution of Ar-O_2 thermal plasma with Ti powder injection at radial positions of 5 mm for reduced sheath gas flow rate (a), feedstock feeding rate (b), input power (c) from the reference condition. . . 58
3.11 Streamline in Ar-O_2 thermal plasma with Ti powder injection for reduced sheath gas flow rate (a), feedstock feeding rate (b), input power (c) from the reference condition at a pressure of 300 Torr. 59
3.12 Mass fraction distribution of Ti vapor in Ar-O_2 plasma with Ti powder injection for reduced sheath gas flow rate (a), feedstock feeding rate (b), input power (c) from the reference condition at a pressure of 300 Torr. . . 61
3.13 Temperature distribution in Ar-O_2 thermal plasma with Ti powder injection for increased sheath gas flow rate (d), feedstock feeding rate (e), input power (f) from the reference condition at a pressure of 300 Torr. 63
3.14 Radial temperature distribution of Ar-O_2 thermal plasma with Ti powder injection for increased sheath gas flow rate (d), feedstock feeding rate (e), input power (f) at axial positions of 250 mm. 64
3.15 Axial temperature distribution of Ar-O_2 thermal plasma with Ti powder injection for increased sheath gas flow rate (d), feedstock feeding rate (e), input power (f) at radial positions of 5 mm. 64

3.16 Streamline in Ar-O_2 thermal plasma with Ti powder injection for increased sheath gas flow rate (d), feedstock feeding rate (e), input power (f) from the reference condition at a pressure of 300 Torr. 65
3.17 Mass concentration distribution of Ti vapor in Ar-O_2 thermal plasma with Ti powder injection for increased sheath gas flow rate (d), feedstock feeding rate (e), input power (f) from the reference condition at a pressure of 300 Torr. 67
3.18 Time variation in particle diameters of 35 Ti particles injected into Ar-O_2 ICTP for the reference condition. Particles have initial 5 different diameters. The different curves with the same initial diameter indicates the results of particle diameters injected at different initial 7 radial positions as indicated in Fig. 3.2. 70
3.19 An example of particle temperature history flying of a single Ti particle in Ar-O_2 ICTP under the reference condition. Temperatures for 3 shells in a single particle are indicated here. 71
3.20 Time variation in particle diameters of 35 Ti particles injected into Ar-O_2 ICTP with 0.5 g/min feeding rate. Particles have initial 5 different diameters. The different curves with the same initial diameter indicates the results of particle diameters injected at different initial 7 radial positions as indicated in Fig. 3.2. 72

4.1 Configuration ICTP torch with (a) 8-turn coil and (b) 12-turn coil. 83
4.2 Definition of (a) Single-frequency coil and (b) Tandem double-frequency coil. 85
4.3 Definition of parameters for temperature inside a titanium particle. 88
4.4 Particle size distribution and particle injection positions. 92
4.5 Number density of (a) 90%Ar-10%O_2 and (b) 89%Ar-10%O_2-1%Ti thermal plasmas at a pressure of 300 Torr. 97
4.6 Specific heat of 100%Ar gas, 90%Ar-10%O_2 gas mixture, 89%Ar-10%O_2-1%Ti gas mixture and 100%Ti vapor as a function of temperature at 300 Torr pressure. 98

4.7 Thermal conductivity of 100%Ar gas, 90%Ar-10%O_2 gas mixture, 89%Ar-10%O_2-1%Ti gas mixture and 100%Ti vapor as a function of temperature at 300 Torr pressure. 99
4.8 Viscosity of 100%Ar gas, 90%Ar-10%O_2 gas mixture, 89%Ar-10%O_2-1%Ti gas mixture and 100%Ti vapor as a function of temperature at 300 Torr pressure 100
4.9 A full-set of boundary conditions. 101
4.10 Temperature distribution in Ar-O_2 single-frequency coil ICTP with Ti powder injection at different gap lengths of (a) 20 mm, (b) 30 mm, (c) 40 mm, and (d) 60 mm. The coil is operated at an input power of 25 kW at a frequency of 450 kHz. 107
4.11 Axial temperature distribution at radial position of 25 mm in Ar-O_2 single-frequency coil ICTP with Ti powder injection at different gap lengths of (a) 20 mm, (b) 30 mm, (c) 40 mm, and (d) 60 mm. The coil is operated at an input power of 25 kW at a frequency of 450 kHz. 108
4.12 Radial temperature distribution at axial position of 230 mm in Ar-O_2 single-frequency coil ICTP with Ti powder injection at different gap lengths of (a) 20 mm, (b) 30 mm, (c) 40 mm, and (d) 60 mm. The coil is operated at an input power of 25 kW at a frequency of 450 kHz. 109
4.13 Power density distribution in Ar-O_2 single-frequency ICTP with Ti powder injection at different gap lengths of (a) 20 mm, (b) 30 mm, (c) 40 mm, and (d) 60 mm. The coil is operated at an input power of 25 kW at a frequency of 450 kHz. 110
4.14 Temperature distribution in Ar-O_2 tandem double-frequency ICTP by an 8-turn coil with Ti powder injection at different gap lengths of (a) 20 mm, (b) 30 mm, (c) 40 mm, and (d) 60 mm. The upper coil is operated at an input power of 10 kW at a frequency of 450 kHz, while the lower coil is operated at 15 kW and 300 kHz. 113

4.15 Axial temperature distribution at a radial position of 25 mm in Ar-O_2 tandem double-frequency ICTP by an 8-turn coil with Ti powder injection at different gap lengths of (a) 20 mm, (b) 30 mm, (c) 40 mm, and (d) 60 mm. The upper coil is operated at an input power of 10 kW at a frequency of 450 kHz, while the lower coil is operated at 15 kW and 300 kHz. 114

4.16 Radial temperature distribution at an axial position of 230 mm in Ar-O_2 tandem double-frequency ICTP by an 8-turn coil with Ti powder injection at different gap lengths of (a) 20 mm, (b) 30 mm, (c) 40 mm, and (d) 60 mm. The upper coil is operated at an input power of 10 kW at a frequency of 450 kHz, while the lower coil is operated at 15 kW and 300 kHz. 115

4.17 Power density distribution in Ar-O_2 tandem double-frequency ICTP by an 8-turn coil with Ti powder injection at different gap lengths of (a) 20 mm, (b) 30 mm, (c) 40 mm, and (d) 60 mm. The upper coil is operated at an input power of 10 kW at a frequency of 450 kHz, while the lower coil is operated at 15 kW and 300 kHz. 116

4.18 Temperature distribution in Ar-O_2 tandem double-frequency ICTP by a 12-turn coil with Ti powder injection at different gap lengths of (a) 20 mm, (b) 30 mm, (c) 40 mm, and (d) 60 mm. The upper coil is operated at an input power of 10 kW at a frequency of 450 kHz, while the lower coil is operated at 15 kW and 300 kHz. 119

4.19 Axial temperature distribution at the radial position of 25 mm in Ar-O_2 tandem double-frequency ICTP by a 12-turn coil with Ti powder injection at different gap lengths of (a) 20 mm, (b) 30 mm, (c) 40 mm, and (d) 60 mm. The upper coil is operated at an input power of 10 kW at a frequency of 450 kHz, while the lower coil is operated at 15 kW and 300 kHz. 120

4.20 Radial temperature distribution at an axial position of 230 mm in Ar-O_2 tandem double-frequency ICTP by a 12-turn coil with Ti powder injection at different gap lengths of (a) 20 mm, (b) 30 mm, (c) 40 mm, and (d) 60 mm. The upper coil is operated at an input power of 10 kW at a frequency of 450 kHz, while the lower coil is operated at 15 kW and 300 kHz. 121

4.21 Power density distribution in Ar-O_2 tandem double-frequency ICTP by a 12-turn coil with Ti powder injection at different gap lengths of (a) 20 mm, (b) 30 mm, (c) 40 mm, and (d) 60 mm. The upper coil is operated at an input power of 10 kW at a frequency of 450 kHz, while the lower coil is operated at 15 kW and 300 kHz. 122

4.22 Mass fraction distribution of Ti vapour in Ar-O_2 single-frequency ICTP by an 8-turn coil with Ti powder injection at different gap lengths of (a) 20 mm, (b) 30 mm, (c) 40 mm, and (d) 60 mm. The coil is operated at an input power of 25 kW at a frequency of 450 kHz. 124

4.23 Streamlines in Ar-O_2 single-frequency ICTP by an 8-turn coil with Ti powder injection at different gap lengths of (a) 20 mm, (b) 30 mm, (c) 40 mm, and (d) 60 mm. The coil is operated at an input power of 25 kW at a frequency of 450 kHz. 125

4.24 Mass fraction distribution of Ti vapour in Ar-O_2 tandem double-frequency ICTP by an 8-turn coil with Ti powder injection at different gap lengths of (a) 20 mm, (b) 30 mm, (c) 40 mm, and (d) 60 mm. The upper coil is operated at an input power of 10 kW at a frequency of 450 kHz, while the lower coil is operated at 15 kW and 300 kHz. 128

4.25 Streamlines in Ar-O_2 tandem double-frequency ICTP by an 8-turn coil with Ti powder injection at different gap lengths of (a) 20 mm, (b) 30 mm, (c) 40 mm, and (d) 60 mm. The upper coil is operated at an input power of 10 kW at a frequency of 450 kHz, while the lower coil is operated at 15 kW and 300 kHz. 129

4.26 Mass fraction distribution of Ti vapour in Ar-O_2 tandem double-frequency ICTP by a 12-turn coil with Ti powder injection at different gap lengths of (a) 20 mm, (b) 30 mm, (c) 40 mm, and (d) 60 mm. The upper coil is operated at an input power of 10 kW at a frequency of 450 kHz, while the lower coil is operated at 15 kW and 300 kHz. 130

4.27 Streamlines in Ar-O_2 tandem double-frequency ICTP by an 12-turn coil with Ti powder injection at different gap lengths of (a) 20 mm, (b) 30 mm, (c) 40 mm, and (d) 60 mm. The upper coil is operated at an input power of 10 kW at a frequency of 450 kHz, while the lower coil is operated at 15 kW and 300 kHz. 131
4.28 Variation in diameters of 35 Ti particles in Ar-O_2 single-frequency ICTP by an 8-turn coil with 60 mm gap length. 134
4.29 Temperature history of Ar-O_2 in single-frequency coil ICTP with 60 mm gap length. 135
4.30 Variation in diameters of 35 Ti particles in Ar-O_2 tandem double-frequency ICTP by an 8-turn coil with 60 mm gap length. 136
4.31 Variation in diameters of 35 Ti particles in Ar-O_2 tandem double-frequency ICTP by 12-turn coil with 60 mm gap length. 136

List of Tables

2.1 Thermodynamic Properties of Silicon Powder 23

3.1 Thermodynamic properties of titanium powder 54
3.2 Calculation condition with lower value in parameters from reference. 54
3.3 Calculation condition with higher value in parameters from reference. . . . 55

4.1 Numerical conditions 103
4.2 Thermodynamic properties of titanium powder [37]. 104

Acknowledgement

I wish to express my higher gratitude and thankful to Prof. Yasunori Tanaka as my major professor. You always help me since the first day to answer my questions and concerns, large or small, and many valuable suggestions, discussions, support, personal guidance, and encouragement. I feel very privileged to have worked with him. Without his guidance, I would never have learned what I know about the thermal plasma, principles of plasma discharge and material processing, tandem thermal plasma technology, and I would certainly never have come this far. Thank you very much.

For finishing this thesis I am indebted to many people for their help in completing this study. First of all, I would like to thank my co-supervisor Prof. Yoshihiko Uesugi, Prof. Tatsuo Ishijima and Dr. Yusuke Nakano for many useful discussions and helps. To all members of the Electric Power and Environment Laboratory for answering my questions with concerns.

I would also like to thank to dean of Engineering Faculty and Head Departement of Electrical Engineering at University of Sumatera Utara, Indonesia, I sincerely appreciate their help as well. I am also thankful to all my friends of Dikti-Kanazawa University awardee in 2016 who also strive to finish their study. I hope we can continue being friend and support each other.

I am grateful to and for my wife and best friend, Nani Barorah Nasution who kept me motivated and support me during all the process, I hope we always remember how we strive and hold on to reach our dream. My most thankful is to my beloved son and daughter, Danish Juna Siregar and Dhakira Juna Siregar. I am nothing without your love and caring, both of you is the real true fighter, and I learn a lot from both of you. I know it must be hard in the beginning to learn and adapt to new culture and language, but both of you make me proud and always grateful to be your father. Thank you for being lovely children. I hope one day, I will back to Japan, to see you study here.

I thanks to my parents Rahim Siregar and Chairani Harahap, from them I learn that education can change path and mind, thank you for the inspiration and the work ethic you instilled in me, I will never be able to payback all the love you give and teach me. I thank to my father in law and mother in law Nasrun Naution and Yusnani Tambunan, for always support us. I thank my brothers (in-law) and sister (in-law) Irfan Siregar, Yenny Marlina, Cherry Siregar, Zainal Safri, Andy Siregar, Intan Suhaila, Dicky Zickrika Siregar, Faradilla Safitri Siregar and all my nephews for always being supportive and always care

Lastly, but the most influence I would like to thank Allah SWT, as written in Al-Quran Surah Al-Mujadalah verse 11 “Allah will raise to high ranks those of you who believe and are endowed with knowledge. Allah is well aware of all that you do”. I hope through this process, I will one of the person who Allah grant high ranks.

Abstract

Thermal interaction between feed rate powder and thermal plasma was calculated using the developed numerical model for inductively coupled thermal plasma (ICTP) with particle injection. The interaction between feed powder and thermal plasmas is greatly important to consider the stable establishment of the ICTP and effective heating and evaporation of injected particles, for example, for particle synthesis. Injected particles are heated by thermal plasma, and they are melted and evaporated to contaminate the thermal plasma, which influences the thermal plasma properties. The ICTP model was used in this research because it has benefit of good repeatability and no contamination process. Interactions between ICTP and injected powder are very complicated to be understood only by related experiments. The developed numerical model solves mass, momentum and energy conservation equations of thermal plasmas as well as mass transport equation for evaporated materials. In addition, particle motions were derived by solving the lagrange equation of motion. The temperature distribution inside the particles and phase transition from solid, liquid to gas of the particles were also taken into account.

Furthermore, numerical simulation in inductively coupled thermal plasma was made on the temperature distribution in argon (Ar)+ hydrogen (H_2) induction thermal plasma torch with silicon (Si) powder injection to obtain the temperature distribution and gas flow fields. The ICTP model was used in this research because it has benefit of good repeatability and no contamination process. The temperature distributions of thermal plasma and Si vapor distribution were compared at input powers of 20 kW, 30 kW, and 40 kW. Results indicated that higher input power increases the temperature of the thermal plasma with doughnut shape but it slightly enhances evaporation of the powder at the center axis of the plasma torch.

In addition, thermal interaction between titanium feedstock powder and thermal plasma was calculated using the developed numerical model for inductively coupled thermal plasma

(ICTP) with particle injection. The interaction between titanium powder and thermal plasmas is greatly important to consider the stable establishment of the ICTP and effective heating and evaporation of injected particles, for example, for particle synthesis. Injected particles are heated by thermal plasma, and they are melted and evaporated to contaminate the thermal plasma, which influences the thermal plasma properties. The developed numerical model solves mass, momentum and energy conservation equations of thermal plasmas as well as mass transport equation for evaporated materials. In addition, particle motions were derived by solving the Lagrange equation of motion. The temperature distribution inside the particles and phase transition from solid, liquid to gas of the particles were also taken into account. Finally, a parametric study was conducted to show the influence of different important physical parameters such as input power, sheath gas flow rate, and Ti powder feeding rate.

In this thesis, tandem ICTP is formed using two coil currents (upper coil and lower coil) in a single plasma torch, that was already developed for nanoparticle synthesis. The temperature distribution of the tandem ICTP and evaporation of feedstock Ti powder were obtained for different gap lengths between the upper and lower coil and coil turn numbers. Results indicate that increasing the gap length between the upper and lower coil produces two separately controlled high-temperature areas in tandem ICTP. This result suggests that tandem ICTP provides a temperature field that is favourable for particle evaporation of injected particles while maintaining ICTP in the upper region of the plasma torch for stable operation

Chapter 1

Introduction

1.1 Plasma state

1.1.1 Overview of plasma

The plasma state has fourth state of matter in the sequence: solid, liquid, gas and plasma, as depict in Fig. 1.1 When the material is heated, it changes from solid, to liquid, to gas phase, and then even becomes hotter. In solid state, molecules and atoms in the material onerously move because of very low kinetic energy. In liquid and gas states, neutral particles move freely in the space because the kinetic energy is higher than that of solid state. If the energy applied to matter is increased more from gas state, neutral particles can be splitted into electrons and ions, that is, ionization. This fourth state of matter is called ionized gas or "Plasma".

Ionized gas can be called a plasma if plasma has electrons, ions (positive and negative ions of molecules and atoms) and molecules and/or neutral atoms. Therefore, plasma is microscopically charged positively or negatively because it contain both positive and negative species. However, positive and negative charged particle move collectivity in plasma state. Furthermore, plasma containing the same number of positive and negative species. Hence, if characteristic length is much longer than the Debye length, plasma is electrically neutral in macroscopic view. In summary, *A plasma balance each other in positive and negative charges and plasma must be neutral particles which exhibits collective behavior*. This is a basic theory and useful definition of plasma [1].

As explained above, plasma has other neutral, electrons, and charged particles. The other particles is much heavier than mass of electron. Thus neutral particles and ions are

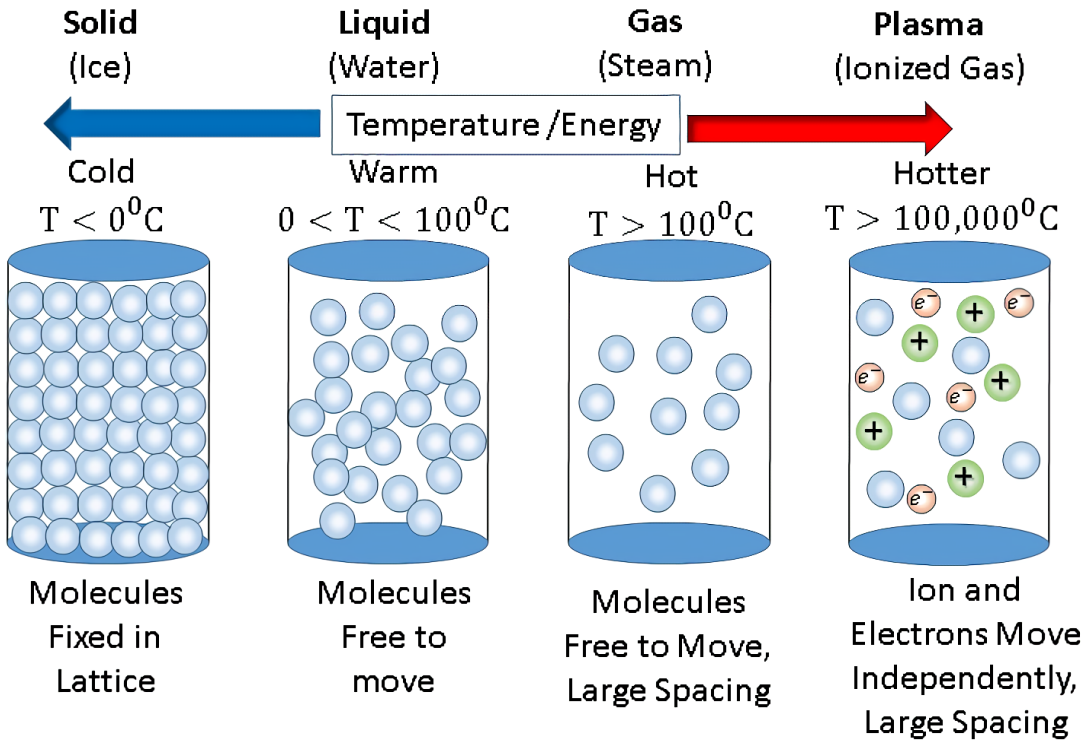

Fig. 1.1: States of materials.

often classified "heavy particle". The different kinetic energy in the plasma caused by the differences of electron, particle mass, and other heavy particle. Thus, electron and other heavy particle has different kinetic temperature as discussed in the following paragraph.

1.1.2 Concept of temperature in a plasma

Plasma consist of electrons, ions and neutral particles. Due to differences in the large mass between electrons and other heavy particles, the other heavy particle and electron can produce different kinetic energy (i.e. kinetic temperature). The kinetic temperature of other heavy particles and the electron are expressed as "heavy particle temperature" and "electron temperature", respectively. These temperatures in plasma are determined by average kinetic energy of the particle. If the Maxwell-Boltzmann distribution is followed by particles, the average kinetic energy can be expressed as follows [2, 3]:

$$\frac{1}{2}m\overline{v^2} = \frac{3}{2}kT \tag{1.1}$$

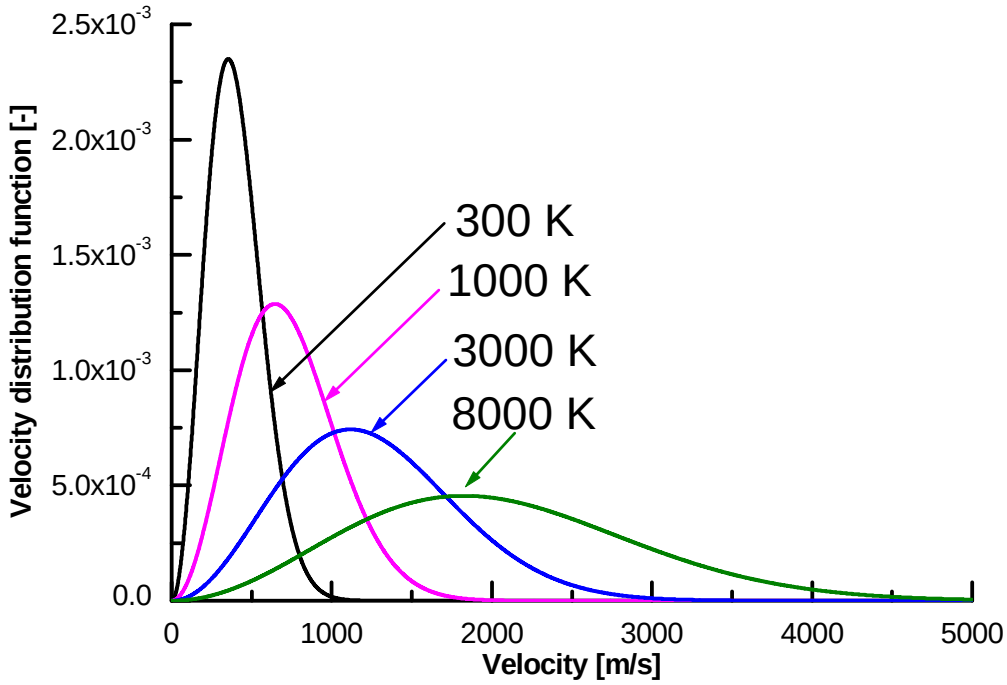

Fig. 1.2: Maxwell-Boltzmann distribution of velocities in argon atom.

where $(\overline{v^2})^{1/2}$ is root mean square velocity, m is the mass of particle , T is the kinetic temperature, and k is the Boltzmann constant. Thus, to explain kinetic energy or other parameters in the plasma on a macroscopic scale, microscopic properties have to be averaged. The velocity distribution function of the particle should be introduced in this purpose.

The velocity distribution function $f(\vec{v}, \vec{r}, t)$ depends on velocity $\vec{v}$ at that coordinate, the space coordinate $\vec{r}$, and time t. The velocity element $\vec{v} \rightarrow \vec{v} + d\vec{v}$ and number of particle dwelling in the volume element $dxdydz$ $(=d\vec{r})$ is given by following equation:

$$\Delta N = f(\vec{v}, \vec{r}, t) \cdot d\vec{v} \cdot d\vec{r} \tag{1.2}$$

$$n(\vec{r}, t) = \int f(\vec{v}, \vec{r}, t) d\vec{v} \tag{1.3}$$

where N is the total number of particle. Thus, the integration of Eq. (1.2) over the total velocity space gives the total particle number density $n(\vec{r}, t)$ The velocity distribution function $f(\vec{v}, \vec{r}, t)$ gives existence probability of particle at that velocity.

Distribution function is studies by the Maxwell-Boltzmann distribution function. If the energy of each particles are fully exchanged., collision frequency between each particles are very high. Meanwhile, this high collision frequency leads a plasma to complete-equilibrium state. Under the complete-equilibrium condition, the distribution function is isotropic, uniform, and steady. The number of particles having velocities between $v \rightarrow v + dv$, in random directions at an absolute temperature T is expressed by

$$\frac{dN(v)}{N_{\text{tot}}} = f(v)dv = \frac{4\pi v^2 dv}{(2\pi kT/m)^{3/2}} \exp\left(-\frac{mv^2}{2kT}\right) \tag{1.4}$$

As shown in Fig. 1.2, the Maxwell-Boltzmann distribution of velocities in Argon (Ar) atom. When the plasma reaches high temperature, particles in the plasma will reach high energy, thus the proportion of higher speed particles is increased.

The Maxwell-Boltzmann distribution function is very important property to decide the temperature in the plasma. There are several types of "temperature" in the plasma; heavy particle temperature, excitation temperature vibrational and rotational temperature of diatomic molecule, and electron temperature. Former two temperatures, heavy particle temperature and electron temperature, are caused on the kinetic energy of the translational motion of these particles. In the following section, classification of plasmas by electron temperature and electron density for simplicity.

1.1.3 Different types of plasma by temperature

Various kinds of plasma sources have been discovered and developed until now. Each type of plasma has unique electron density and temperature as depict in Fig. 1.3. Furthermore, "temperature" is a very important parameter for classifying plasma.

As explained above section, plasma has various type of temperature, heavy particle temperatures and electron are most basic temperature in plasmas. In this section, plasmas are classified based by temperature differences between heavy particle and electron.

When plasma is called "thermal equilibrium plasma (thermal plasma)", then heavy particle temperature is equal to electron temperature. The temperature of the gas is very high up to few thousands kelvin or few tens thousands kelvin by thermal plasma. Due to the high temperature, thermal plasma also has high chemical activity field. These high chemical activity field and high temperature sustain us to use thermal plasma for various types

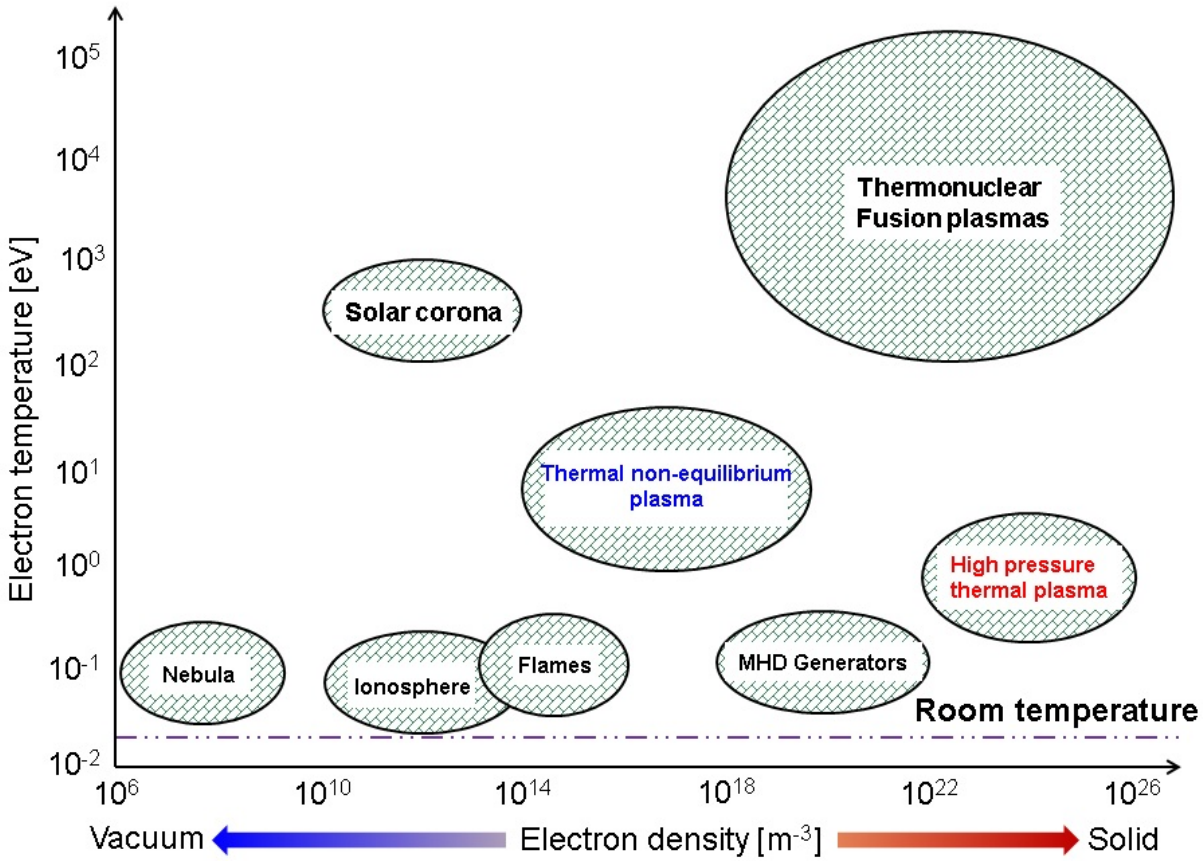

Fig. 1.3: Classification of plasmas by electron temperature and electron density.

of material processing such as deposition, combustion processes, surface modification, arc cutting and welding, and nanopowder synthesis Conversely, if heavy particle temperature is not equal to electron temperature, that plasma is "thermal non-equilibrium plasma". Non-thermal plasma has lower gas temperature compared with electron temperature.

Gas temperature in non-thermal plasma is close to room temperature. However, the electron temperature often have few eV for thermal non-equilibrium plasma. If gas temperature is lower than room temperature, that plasma is categorized into cryo-plasma. Non-thermal plasma is generally used for low temperature process such as medicine, sterilization, semiconductor manufacturing, and so on.

In contrast, if heavy particle temperature is not equal to electron temperature, that plasma is classified "thermal non-equilibrium plasma". Non-thermal plasma has lower gas temperature compared with electron temperature. Gas temperature in non-thermal plasma is close to room temperature. However, the electron temperature often have few eV for

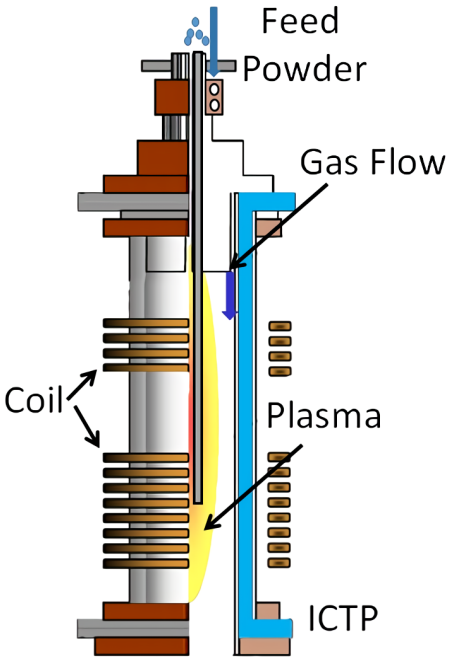

Fig. 1.4: Configuration of ICTP torch.

thermal non-equilibrium plasma. If gas temperature is lower than room temperature, that plasma is categorized into cryo-plasma. Non-thermal plasma is generally used for low temperature process such as medicine, sterilization, semiconductor manufacturing, and so on. The thermal plasma and its application are mainly discussed in this thesis.

1.2 Inductively coupled thermal plasma torch

An RF discharge can be maintained either by capacitive coupling or inductive coupling with the power source. An inductive coupling discharge is often called "inductively coupled (thermal) plasma", and maintained by the time-varying magnetic field generated by high frequency (e.g. few hundreds kHz to few MHz) coil-current [2]. The inductively coupled thermal plasma (ICTP) is firstly established by T. B. Reed [4]. In the ICTP torch, an induction coil is installed around quartz tube and it is connected to the RF power supply. An induction thermal plasma is established inside of the quartz tube. In this type of plasma source, the electrode and a plasma are spatially separated.

The high-pressure and high-power inductively coupled thermal plasma (ICTP) is widely used as a chemical reaction source and an effective heat source for various materials processing. One benefit of the ICTP is to have higher radical density and higher enthalpy without any impurity contamination because the high power ICTP is sustained by electromagnetic coupling without any electrodes. Another benefit of the ICTP in materials processing is that such an ICTP can provide a one-step direct processing including rapid evaporation of injected raw materials and then rapid cooling of evaporated materials. From the above benefits, the ICTP has been well adopted for synthesis of fullerene, fabrication of diamond films [1], materials surface modifications [2], and thermal barrier coatings [3], etc. Recently in addition, the ICTP is widely used for synthesis of nanometer's. For example, synthesis of TiO_2 nanoparticles [4] are continually receiving attention for use as phonic crystals, photocatalysts [5], gas sensors [6] and photovoltaic cells [7].

In the high-temperature field, the injected feedstock powder is heated to elevate its temperature, which results in its melting and then evaporation. The evaporation of feedstock material can change the temperature field because of powder consumption, and also the gas flow field due to mass source from the evaporation. In addition, the evaporated material can contaminates the ICTP, which can greatly change the thermodynamic and transport properties of the ICTP. Further, the above change in the properties can affect the temperature distribution and gas flow field in the ICTP. These sequential change from feedstock powder injection to evaporation in steady state is extremely complex $[8]^{-}$ [28]. . Using the calculated equilibrium composition, we computed the thermodynamic and transport properties such as the mass density, the enthalpy, the specific heat, the electrical conduc-

tivity, thermal conductivity and viscosity. In calculation of the transport properties, the first order approximation of Chapman-Enskog method was adopted [19] [20] [30] [31].

Figure 1.4 depicts the configuration of the inductively coupled thermal plasma torch used in this research. The plasma torch comprises two coaxial quartz tubes. Between the inner quartz tube and the outer quartz tube, cooling water flows to keep the wall temperature around 300 K. Around the outer quartz tube, an eight-turn induction coil is installed. To this coil, the radio-frequency (rf) coil current is supplied to generate electromagnetic field inside the plasma torch from an rf power source. The coil current frequency is 450 kHz. On the other hand, from the head of the plasma torch, gas mixture is supplied as a sheath gas. This sheath gas is supplied along the inner quartz tube wall with a swirl to prevent the plasma from contacting the inner quartz tube. The electromagnetic field generated by the coil current can accelerate an electron inside the torch, and a plasma can be formed there if the electron impact ionization occurs. At high pressure near atmospheric pressure, the thermal plasma with high gas temperature is generated without any electrode. This is called inductively coupled thermal plasma (ICTP). One feature of the ICTP is the high gas temperature, high enthalpy without any contamination from the electrodes. As for feedstock, titanium (Ti) feedstock powder was injected to the high temperature region of the ICTP directly through the water-cooled tube with Ar carrier gas flow. This water-cooled tube installed from the top of the plasma torch head deeply into the torch. For numerical calculation of ICTP with powder injections, the calculation space was set to the two-dimensional cylindrical $r - z$ cross section of this plasma torch.

1.3 Objective of this thesis

The high-pressure and high-power inductively coupled thermal plasma (ICTP) is widely used as a chemical reaction source and an effective heat source for various materials processing. One benefit of the ICTP is to have higher radical density and higher enthalpy without any impurity contamination because the high power ICTP is sustained by electromagnetic coupling without any electrodes. Another benefit of the ICTP in materials processing is that such an ICTP can provide a one-step direct processing including rapid evaporation of injected raw materials and then rapid cooling of evaporated materials. From the above benefits, the ICTP has been well adopted for synthesis of fullerene, fabrication of diamond films, materials surface modifications, and thermal barrier coatings, etc. Recently in addition, the ICTP is widely used for synthesis of nanometer's. For example, synthesis of TiO_2 nanoparticles are continually receiving attention for use as phonic crystals, photocatalysts, gas sensors and photovoltaic cells. To consider the process of nanoparticle synthesis, it is very important to understand thermal interaction between feedstock powder injected and high-temperature field in the ICTP.

On the other hands, in plasma torch, feedstock powder is injected to the high-temperature field, thereby causing its evaporation. The evaporated materials are subsequently cooled to achieve nucleation and thereafter to synthesize nanomaterials. During these processes, the ICTP sometimes becomes unstable because of disturbance from heavy-load injection of feedstock powder. In the worst case, the ICTP can be extinguished by an overly heavy-load injection of feedstock powder. To resolve this persistent difficulty, a tandem-type inductively coupled thermal plasma (tandem ICTP) has been developed. The tandem ICTP is established in a dielectric cylindrical tube with two coils. Powder injection is well known to affect the temperature field in the ICTP by powder evaporation. The materials evaporated into the thermal plasma can markedly change the thermodynamic and transport properties of the thermal plasma. This marked change in the properties can alter the temperature and the gas flow field in thermal plasmas.

The goal of this work is to develop of numerical model on thermal interaction between feedstock powder injected and high-temperature field and control the gas temperature because of disturbance from heavy-load injection of feedstock powder. In this work, the developed model is based on the PSI-Cell concept developed by Crowe *et al* [26]; it is

an extension of the work by Proulx and co-workers [27, 28]. In modeling, the following assumptions were made:

1. The plasma is in local thermodynamic equilibrium; consequently, all the temperatures such as the electron temperature, heavy particle temperature, and excitation temperatures are identical. In addition, the model assumes chemical equilibrium conditions for all reactions.

2. The plasma is optically thin for wavelengths greater than 200 nm. For wavelengths of less than 200 nm, 20% of the total emission coefficient is accounted for radiation loss to consider the effective light absorption [4, 29].

3. The flow is steady, laminar, and axis-symmetric, with negligible viscous dissipation.

4. For injected particles, the particle-particle interactions are neglected.

5. The particle radius is much larger than the mean free path of plasma components.

6. The particle is always spherical even during and after melting and evaporation.

7. Particle surface is uniformly heated from thermal plasmas. Thus, evaporation also uniformly occurs around the particle surface.

8. Effects of electric charging on the particle are neglected.

9. The rocket effect from ejected ablation vapor is neglected.

10. Titanium feedstock particles are evaporated by the heat from the thermal plasma

1.4 Composition of the thesis

This thesis is composed from following chapters. In first chapter, which is already described, fundamental informations of plasma were introduced. In second chapter, Interaction between feedstock powder and thermal plasma was investigated for Ar/H_2 thermal plasma with Si powder. In third chapter, Inclusion of particle evaporation feedstock evaporation were fundamentally investigated for Ar/O_2 Induction Thermal Plasmas with Ti Powder Injection. In fourth chapter, Interaction of heavy-load injection of feedstock powder with tandem ICTP were investigated for stable temperature distribution with Ar-O_2 and Ti feedstock powder injection. In final chapter, fifth chapter, is summary of this thesis.

References

[1] F. C. Chen : "Introduction to plasma physics " *New York: Plenum press* **1** (1974)

[2] M. I. Boulos, P. Fauchais and E. Pfender: "Thermal plasmas fundamentals and applications" *New York: Plenum Press* **1** (1994)

[3] M. A. Lieberman, and A. J. Lichtenberg : "Principles of plasma discharges and materials processing" *Wiley Interscience* **2** (2005)

[4] T. B. Reed : "Induction-coupled plasma torch" *J. Appl. Phys*, **32**, pp. 821–4 (1961)

[5] S. Gottlieb, N. Whrl, S. Schulz, V. Buck : "Simultaneous synthesis of nanodiamonds and graphene via plasma enhanced chemical vapor deposition (MW PE-CVD) on copper" *SpringerPlus* **5:568** pp.1-16 (2016)

[6] K.S. Kim, A. Moradian, J. Mostaghimi, G. Soucy : " Modeling of induction plasma process for fullerene synthesis: Effect of plasma gas composition and operating pressure" *Plasma Chemistry and Plasma Processing* **30** pp. 91-110 (2010)

[7] J. Mao, M. Liu, C.G. Deng, C.M. Deng, K.S. Zhou, Z.Q. Deng : "Preparation and distribution analysis of thermal barrier coatings deposited on multiple vanes by plasma spray-physical vapor deposition technology" *Journal of Engineering Materials and Technology, Transactions of the ASME* **139** (2017)

[8] Y. Tanaka and T. Sakuta : "Investigation of plasma-quenching efficiency of various gases using induction thermal plasma technique: effect of various gas injection on Ar thermal ICP" *Journal of Physics D: Applied Physics* **35** pp. 2149-2158 (2002)

[9] A. Mahmood, S.M. Ramay, Y.S. Al-Zaghayer, S. Atiq, I. Ahmad, M.A. Shar, S.D. Khan : "Study the structure and performance of thermal/plasma modified Au

nanoparticle-doped TiO_2 photocatalyst" *Modern Physics Letters B* **28** pp.1450208-1 - 1450208-12 (2014)

[10] P.B. Kuyyadi, K.J. Mahaveer : "Effect of crystallization on humidity sensing properties of sol-gel derived nanocrystalline TiO_2 thin films" *Elsevier* **516** pp. 2175-2180 (2008)

[11] P.-J. Chu, S.-Y. Wu, K.-C. Chen, J.-L. He, A. Yerokhin, A. Matthews : "Nano-structured TiO_2 films by plasma electrolytic oxidation combined with chemical and thermal post-treatments of titanium, for dye-sensitized solar cell applications" *Thin Solid Films* **519** pp. 1723-1728 (2010)

[12] E. Pfender and Y.C.Lee : "Particle dynamics and particle heat and mass transfer in thermal plasma, Part I: The motion of a sigle particle without thermal effects", *Plasma Chem. Plasma Process.* **5** pp. 211-237 (1985)

[13] Y. C. Lee, Y. P. Chyou and E. Pfender: "Particle dynamics and particle heat and mass transfer in thermal plasmas, Part II: Particle heat and mass transfer in thermal plasmas", *Plasma Chem. Plasma Process.* **5** pp. 391-414 (1985)

[14] Y. P. Chyou and E. Pfender : "Behavior of particulates in thermal plasma flows", *Plasma Chem. Plasma Process.*, **9**, pp. 45–71 (1989)

[15] C.T. Crowe, M.P. Sharma and D.E. Stock : "The particle source in cell (PSI-Cell) model for gas droplet flows" *J. Fluids Eng.* **99** pp. 325-332 (1977)

[16] P. Proulx, J. Mostaghimi and M.I. Boulos : "Plasma particle interaction effects in induction plasma modeling" under dense loading conditions *Int. J. Heat Mass Transfer* **28** pp. 1327-1336 (1985)

[17] P. Proulx, J. Mostaghimi and M.I. Boulos : "Heating of powder in an r.f. inductively coupled plasma under dense loading conditions" *Plasma Chem. Plasma Process.* **7** pp. 29-52 (1987)

[18] R.S. Devoto : "Transport coefficients of partially ionized argon" *Phys. Fluid* **10** pp. 354-364 (1967)

[19] Y. Tanaka, K.C Paul and T. Sakuta : "Thermodynamic and transport properties of N_2/O_2 mixtures at different admixture ratios" *T. IEE of Japan*, **120-PE**, pp.24-30 (2000)

[20] J.M. Yos : "Transport properties of nitrogen, hydrogen, oxygen and air to 30 000 K", *AVCO Technical Memorandum RAD-TM* **196401** pp.73 (1963)

[21] S. Chapman and T.G. Cowling : "The Mathematical Theory of Non-Uniform Gases Third Edition" *Cambridge University Press* (1970)

[22] M.I. Boulos, P. Fauchais and E. Pfender : "Thermal Plasma Fundamentals and Applications" *Plenum Press* **1** pp. 366-369 (1994)

Chapter 2

Influence of input power in Ar/H_2 thermal plasma with Si powder by simulation

2.1 Introduction

High-power and high-pressure inductively coupled thermal plasma (ICTP) has been widely used for various materials processing such as fabrication of diamond films [1], synthesis of fullerene [2], surface modification of materials, nanomaterial [3,4], nanocrystallites [5], nanopowder [6, 7] and thermal barrier coatings [8, 9]. Another important in ICTP is influence of input power. The ICTP can be a sufficient heat and chemical source to various materials processing with no contamination. In addition, the ICTP gives one-step direct processing with rapid evaporation of injected raw materials and also rapid cooling of evaporated materials. The rapid cooliing of evaporated material can enhance nucleation of vapor and produce nanoparticles in metastable phase or a non-equilibrium during nanoparticle synthesis with input power by numerical simulation.

During nanoparticle synthesis, feedstock solid power is often supplied into the ICTP to be evaporated. The evaporation rate depends on the temperature distribution and gas flow fields. However, the temperature distribution and gas flow field are also influenced by injected feedstock powder. To understand these complex processes, it is important to model the ICTP with power injection considering its evaporation. Previously, we have developed a numerical model to understand thermal interactions between thermal plasma and particles [10]– [12]. In this work, we studied the influence of input power on thermal

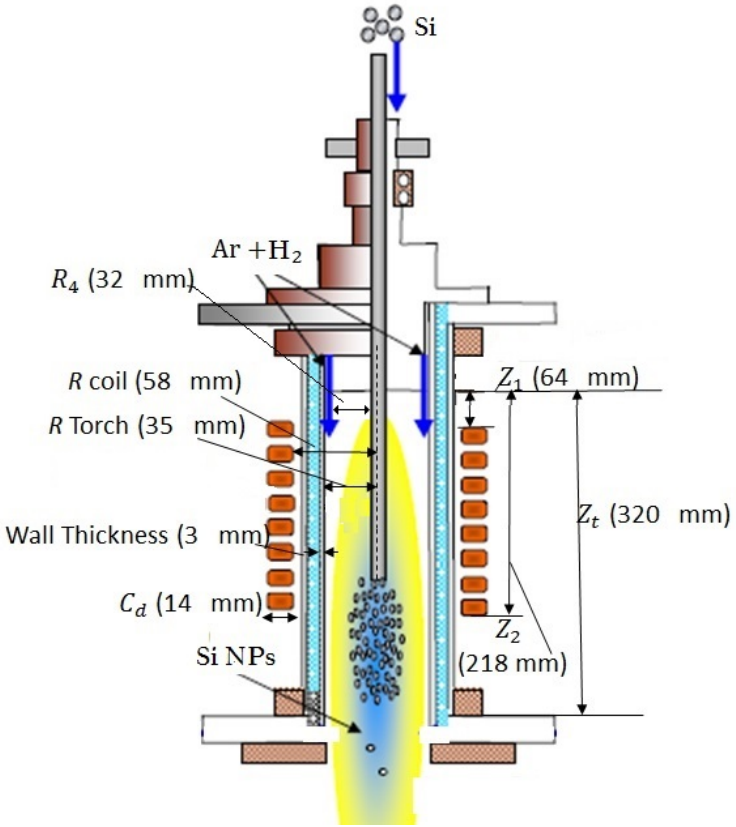

Fig. 2.1: Configuration of ICTP torch.

interactions between 99% Ar+1%H_2 ICTP and silicon (Si) feedstock powder injection using our previously developed numerical simulation model [13]– [16]. Results indicated that influence of input power can increase the thermal plasma temperature in the plasma torch but can just slightly enhance evaporation of feedstock powder at the center axis of the plasma torch.

2.2 Configuration of Inductively Coupled Thermal Plasma torch

Figure 4.1 shows the configuration of the inductively thermal plasma torch used in this numerical simulation. The plasma torch contains two coaxial quartz tubes with 320 mm in length. The inner quartz tube has an internal radius of 35 mm with 3 mm in thickness. An 8 turn-coil is located around the quartz tube to generate the electromagnetic field. The

radius of this coil is 58 mm. The generated electromagnetic field forms a thermal plasma inside the torch by inductively coupling. The torch wall of the plasma torch is cooled at room temperature with cooling water. Silicon powder is injected through a water cooled pipe into the ICTP as indicated in Figure 4.1. The carrier gas is also injected together with the silicon powder through this pipe. For numerical simulation of the ICTP with silicon powder injections, a two-dimensional cylindrical r-z cross section of this plasma torch was set as the calculation space.

2.3 Modeling of the Inductively Coupled Thermal Plasma with Powder Injection

2.3.1 Modelling Assumptions

We have assumed the following conditions for modeling thermal plasma [10]– [14]; (i) Local thermodynamic equilibrium (LTE) is established in the inductively coupled thermal plasma. Thus, all the temperatures such as the heavy particle temperature, excitation temperature, and electron temperature are identical. In addition, we have equilibrium conditions for all reactions. (ii) The optically thin condition is assumed in the plasma at wavelengths above 200 nm. Whereas at wavelengths below 200 nm, 20% of the total emission coefficient is accounted for as radiation loss to take into consideration the effective light absorption. (iii) Steady, laminar, and axis-symmetric flow is assumed without viscous dissipation. (iv) The particle-particle interactions are neglected for injected particles. (v) The mean free path of plasma components is assumed to be much smaller than the particle radius. (vi) Particle always has spherical shape even at evaporation. (vii) The particles are uniformly heated from the surrounding plasmas. Therefore, evaporation uniformly occurs around the particle surface. (viii) Effects of electronic charging on the particle are not considered. (ix) The rocket effect from ejected evaporation vapor is not taken into account. (x) Silicon feedstock powder particle is evaporated only by heat from the plasma.

2.3.2 Governing equation

For an individual feedstock particles supplied through the water-cooled tube, we solve the equation of motion were solved with Lagrangian form considering drag force from the plasma fluid and gravity. In addition, we solve the energy conservation equation of the individual particle taking into account heat conduction inside the particle, the heat flux from the plasma and radiation loss from the particle surface. In addition, we considered melting and evaporation process at the surface of the particles. The detail of the calculation can be obtained in reference [12]. Based of the assumptions described above, the thermal plasma is governed by the following equation.

Mass conservation.

$$\frac{\partial(\rho u)}{\partial z} + \frac{1}{r}\frac{\partial(r\rho v)}{\partial r} = S_{\mathrm{p}}^{C} \tag{2.1}$$

Momentum conservation.

Axial:

$$\begin{aligned} &\rho u\frac{\partial u}{\partial z} + \rho v\frac{\partial u}{\partial r} \\ &= -\frac{\partial p}{\partial z} + 2\frac{\partial}{\partial z}(\eta\frac{\partial u}{\partial z}) \\ &+ \frac{1}{r}\frac{\partial}{\partial r}[\eta r(\frac{\partial u}{\partial r} + \frac{\partial v}{\partial z})] + \mu_0\sigma\Re[\dot{E}_\theta\dot{H}_r^*] + S_{\mathrm{p}}^{M_z} \end{aligned} \tag{2.2}$$

Radial:

$$\begin{aligned} &\rho u\frac{\partial v}{\partial z} + \rho v\frac{\partial v}{\partial r} \\ &= -\frac{\partial p}{\partial r} + \frac{\partial}{\partial z}[\eta(\frac{\partial v}{\partial z} + \frac{\partial u}{\partial r})] \\ &+ \frac{2}{r}\frac{\partial}{\partial r}(\eta r\frac{\partial v}{\partial r}) - 2\eta\frac{v}{r^2} + \mu_0\sigma\Re[\dot{E}_\theta\dot{H}_z^*] + S_{\mathrm{p}}^{M_r} \end{aligned} \tag{2.3}$$

Swirl:

$$\begin{aligned} &\rho u\frac{\partial w}{\partial z} + \rho v\frac{\partial w}{\partial r} \\ &= \frac{\partial}{\partial z}\left(\eta\frac{\partial w}{\partial z}\right) + \frac{1}{r}\frac{\partial}{\partial r}\left(r\eta\frac{\partial w}{\partial r}\right) \\ &- \frac{\rho v w}{r} - \frac{w}{r}\frac{\partial r\eta}{\partial r} \end{aligned} \tag{2.4}$$

Energy conservation.

$$\begin{aligned}\rho u\frac{\partial h}{\partial z}+\rho v\frac{\partial h}{\partial r}&\\ =\ &\frac{\partial}{\partial z}(\frac{\lambda}{C_{\rm p}}\frac{\partial h}{\partial z})+\frac{1}{r}\frac{\partial}{\partial r}(r\frac{\lambda}{C_{\rm p}}\frac{\partial h}{\partial r})\\ +\ &\sigma|\dot{E}_\theta|^2-P_{\rm rad}-S_{\rm p}^E\end{aligned}\tag{2.5}$$

Mass conservation equation for Si vapor.

$$\begin{aligned}\rho u\frac{\partial Y_{\rm Si}}{\partial z}+\rho v\frac{\partial Y_{\rm Si}}{\partial r}&\\ =\ &\frac{\partial}{\partial z}(\rho D_{\rm Si}\frac{\partial Y_{\rm Si}}{\partial z})+\frac{1}{r}\frac{\partial}{\partial r}(r\rho D_{\rm Si}\frac{\partial Y_{\rm Si}}{\partial r})+S_{\rm p}^C\end{aligned}\tag{2.6}$$

Maxwell equation for vector potential.

$$\frac{\partial^2\dot{A}_\theta}{\partial z^2}+\frac{1}{r}\frac{\partial}{\partial r}(r\frac{\partial\dot{A}_\theta}{\partial r})-\frac{\dot{A}_\theta}{r^2}=j\mu_0\sigma\omega\dot{A}_\theta\tag{2.7}$$

$$\dot{H}_z=\frac{1}{\mu_0}\frac{1}{r}\frac{\partial}{\partial r}(r\dot{A}_\theta),\quad \dot{H}_r=-\frac{1}{\mu_0}\frac{\partial\dot{A}_\theta}{\partial z}\tag{2.8}$$

$$\dot{E}_\theta=-j\omega\dot{A}_\theta\tag{2.9}$$

In these equations, $C_{\rm p}$: specific heat at constant pressure, ρ: mass density, h: enthalpy, σ: electrical conductivity, p: pressure, η: viscosity v: radial flow velocity, u: axial flow velocity, r: radial position, z: axial position, λ: thermal conductivity, $P_{\rm rad}$: radiative loss, $Y_{\rm Ti}$: mass fraction of Ti vapor, $D_{\rm Si}$: effective diffusion coefficient of Si vapor in Ar, μ_0: permeability of vacuum, $\dot{A}_\theta$: phasor of vector potential, ω: frequency of the coil current, $\dot{E}_\theta$: electric field strength, $\dot{H}_z$, $\dot{H}_r$: axial and radial components, of the magnetic field strength, respectively, j: complex factor (j^2=-1).

The magnitudes of the phasor including $\dot{A}_\theta$, $\dot{E}_\theta$, $\dot{H}_z$ and $\dot{H}_r$ are defined as the root mean square values. The asterisks * in Eqns. (4.11) and (4.12) indicate the conjugate, and a symbol $\Re$ is the real part of the phasor. The quantities $S_{\rm p}^C$, $S_{\rm p}^{M_z}$, $S_{\rm p}^{M_r}$, and $S_{\rm p}^E$ indicate source terms by the translation quantities from ablated vapor. These quantities are described later. These terms were computed by PSI cell method developed by P.Proux et al [17]– [19].

The calculation execution method is the same to our previous work [10]– [13]. The above governing equations were solved by SIMPLE method after Patankar to obtain gas flow field, and temperature field. Under this calculated field, particle trajectories were calculated by

solving motion equation for each individual particles, solving particle temperature and size histories along the trajectories. At the same time, the mass, momentum and energy source terms for each control volume from particles were determined. The plasma flow and temperature fields were solved again incorporating these source terms. The new plasma flow field was used to establish new particle trajectories, particle temperature and size history. Iterations are repeated for as many times as needed convergence of the plasma and the solution that accounts for the mutual interaction of the particle and plasma is finally obtained.

2.3.3 Calculation condition

In this calculation, the frequency of the coil current for the ICTP was fixed at 450 kHz. The input power was set to three values of 20 kW, 30 kW, and 40 kW. The pressure was set at 300 Torr (=40 kPa) inside the torch. Total flow rate of Ar and H_2 gas mixture as sheath gas was set to 100 L/min. The fraction of Ar/H_2 was set to 99% Ar-1% H_2. To this ICTP, silicon feedstock powder was assumed to be injected through a water-cooled pipe inserted on the torch axis from the plasma torch head. The injected silicon feedstock powder has a mean diameter of 2 μmm and a deviation of 1 μm. The silicon feedstock feed rate was set to 0.5 g/min. The thermodynamic properties of Silicon used in the numerical calculation is summarized in Table 1. In addition, thermodynamic and transport properties of Ar-H_2 mixture and Si vapor were in advance calculated as a function of temperature [20]. Transport properties for the numerical calculation can was adopted by Chapman-Enskog method [21]– [22].

Table 2.1: Thermodynamic Properties of Silicon Powder

Parameter	Unit	Value
Injection load	[g/min]	0.1
Mass density	[kg/m^3]	4506
Melting temperature	[K]	1953
Boiling temperature	[K]	3535
Latent heat for melting	[kJ/kg]	391
Latent heat for evaporation	[kJ/kg]	8294
Specific heat of solid	[J/(kg·K)]	528
Specific heat of liquid	[J/(kg K)]	700
Thermal conductivity	[W/(m·K)]	14
Emissivity of particle source	(-)	0.4

2.4 Calculation results

2.4.1 The Temperature Distribution of Thermal Plasma

2.4.1.1 Temperature distribution and gas flow pattern

The calculation from governing equation in (2.1) to (2.9) was made for Si powder injection to 90% Ar-1%H_2 ICTP at input powers of 20 kW, 30 kW, and 40 kW to obtain temperature distributions and gas flow pattern of ICTPs, and evaporated mass fraction and also particle size history in Figure 3.3 to 3.2. Figure 3.3(a) shows the temperature distribution of the ICTP with an input power 40 kW, while Figure 3.3(b) shows the temperature distribution with an input power 30 kW, and Figure 3.3(c) presents the result at an input power 20 kW. In case of Figure 3.3(a) with an input power 40 kW, the ICTP has high temperature area about 13000 K in wide region around radial positions of 10 mm $< r <$ 26 mm and axial positions 150 mm $< z <$ 250 mm. At this high temperature area, the current flows inside the thermal plasma to be heated. On the other hand, as indicated in Figure 3.3(b), with an input power 30 kW, the high temperature area at temperatures above 13000 K becomes smaller around radial positions of 12 mm $< r <$ 24 mm and axial positions of 170 mm $< z <$ 240 mm. Furthermore, lower input power 20 kW case as shown in Figure 3.3(c) presents a further smaller high temperature area at temperatures above 13000 K around radial positions of 16 mm $< r <$ 23 mm and axial positions of 205 mm $< z <$ 230 mm. This means that increasing input power makes increased temperature in the ICTP. However, as seen along the center axis, the similar temperature around 6000-6500 K can be obtained for 20 kW, 30 kW, and 40 kW. This implies that increasing power just slightly increases the temperature at the center axis of the plasma torch.

To compare the temperature distribution clearly with input powers of 20 kW, 30 kW, and 40 kW in 99% Ar-1%H_2 ICTPs, the radial temperature distributions at axial positions of z= 250 mm are plotted in Figure 3.4. As seen, an increase in input power hardly improves the axial temperature of the ICTP, although the temperatures outside from a radial position of 10 mm rises by increased input power. This implies that evaporation of Si feedstock is hardly improved just by increasing input power. On the other hand, Figure 3.5 shows the axial temperature distribution at radial position of 5 mm, that is at off-axis region, at different three input powers of 20 kW, 30 kW, and 40 kW. At the off-axis region, the

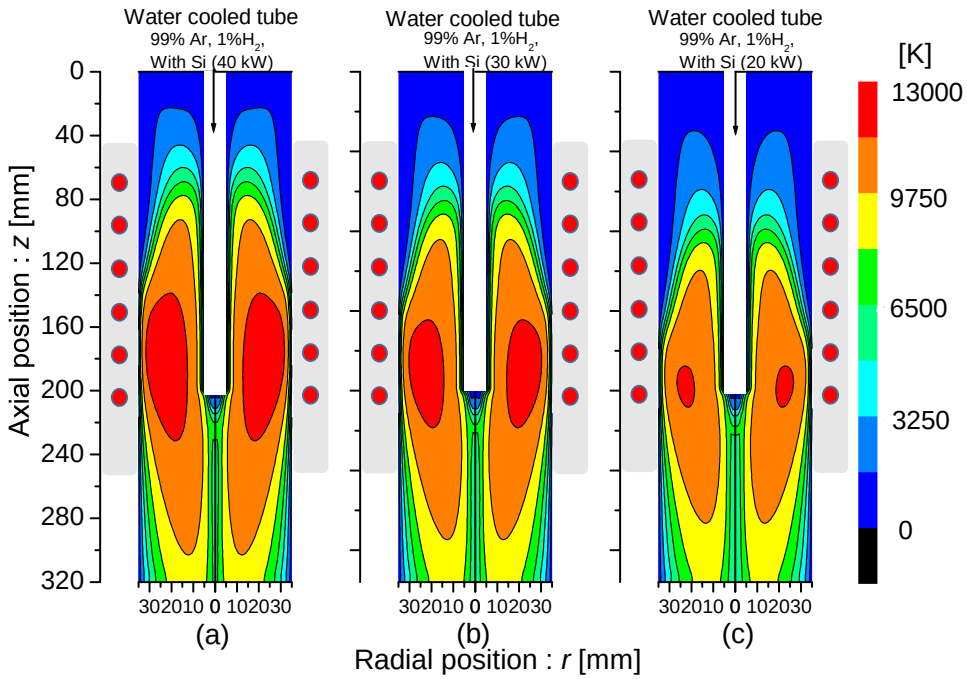

Fig. 2.2: The temperature distribution of 99% Ar-1%H_2 ICTPs with Si powder injection at input powers of 20 kW, 30 kW, and 40 kW.

temperature recovers faster at higher input power.

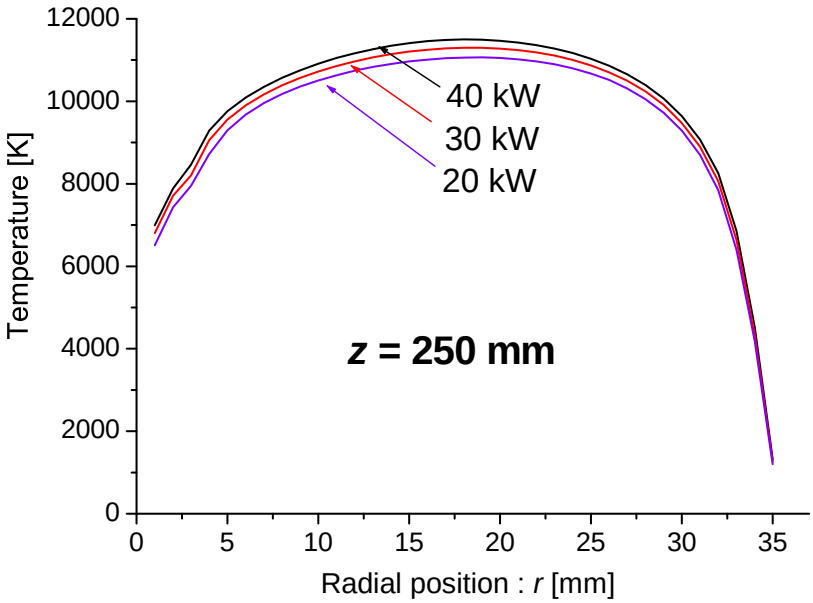

Fig. 2.3: Radial temperature distribution of 99% Ar-1%H_2 ICTP at an axial position of 250 mm with Si powder injection.

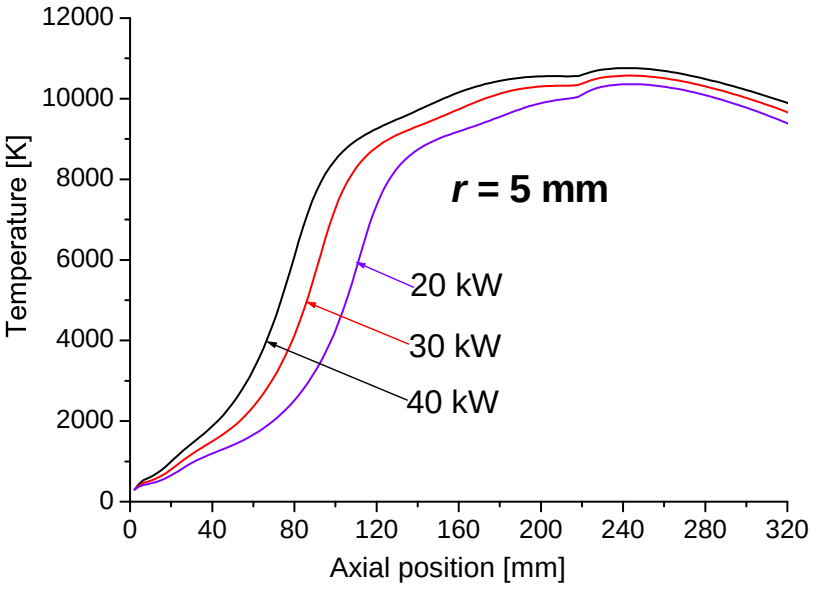

Fig. 2.4: Axial temperature distribution of 99% Ar-1%H_2 ICTP at an radial position of 5 mm with Si powder.

2.4.1.2 Mass fraction distribution of Silicon vapor

We also consider Si evaporation occurrence in the plasma torch. Figure 3.6 shows variation in diameters of the 35 particles with 7 different initial diameters injected from 5 different initial positions [23] into the 40 kW-ICTP as a function of axial position. From axial position from 0 to 200 nm, the diameters do not change because all the particles are present inside the water-cooled pipe. From axial position of 200 mm, the particles start flying into the ICTP, and then they are heated. After some fly to be heated, the Si particles have the diameter decreased. This is because of evaporation of the Si particles from the ICTP. In this case, the particles are strongly heated from the ICTP, and then the particle diameter decreases to. This evaporation generates Si vapor to the ICTP.

Influence of input power on silicon vapor creation in the ICTP can be seen in Figure 3.7. As shown in this figure, the mass fraction of Si vapor is distributed far from the tip of the water-cooled pipe where Si feedstock powder is supplied in 99% Ar+1%H_2 ICTPs with 20 kW, 30 kW, and 40 kW. At just below the tip of the pipe, the temperature of the ICTP becomes low because of heat transfer to Si feedstock particle as indicated in Figure 3.3, and thus the Si feedstock is hardly evaporated. On the other hand, around axial position from 220 mm, Si vapor are generated by evaporation as shown in Figure 3.6.

The evaporation of Si feedstock power causes the contamination of Si vapor inside the ICTP. The contaminated Si vapor is transported by gas flow convection of Ar carrier gas and by diffusion [24, 25]. Thus, silicon vapor is present downstream of the feeding pipe. However, as seen in Figure 3.7, Si vapor concentration just slightly increase with increasing input power. This implies that just increase in the input power just slightly enhances evaporation rate of Si feedstock powder as long as the feedstock is supplied along the center axis of the torch. This slight increase in evaporation is because the input power density is essentially low at the center axis in the ICTP.

The injected particle are transported by drag force from the plasma flow and then the plasma flow also transfers evaporated Si material in the torch. Figure 3.2 presents the streamline inside the ICTP at different input powers of 20 kW,30 kW, and 40 kW. The gas flow field is almost independent of the input power. Therefore, the injected particle supplied along the plasma torch move around the center axis at which input power density is essentially low.

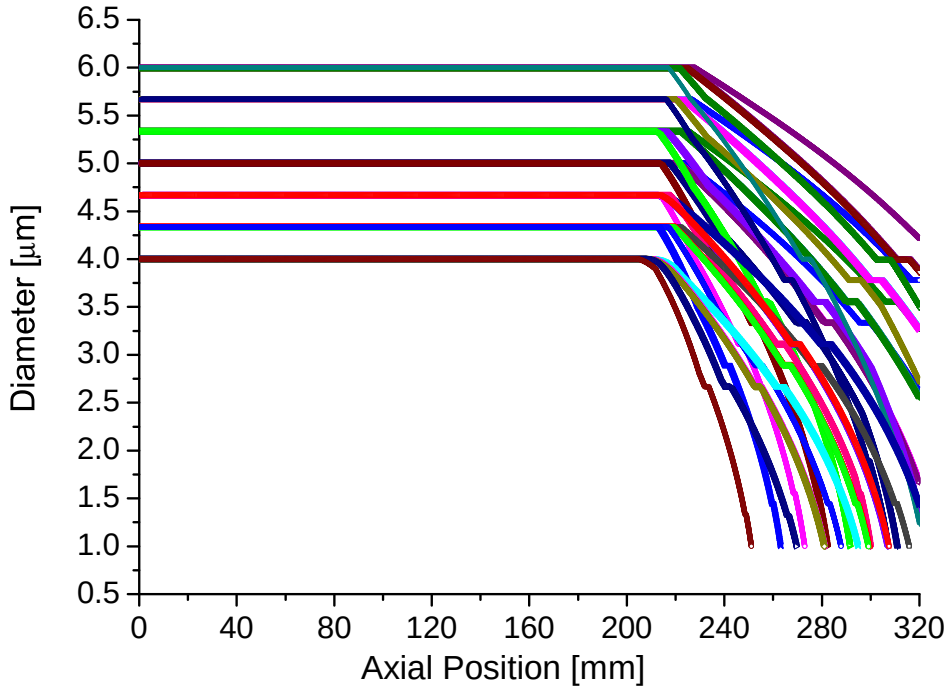

Fig. 2.5: Diameter variation for 35 kinds of Si particles injected with different 7 initial diameters and 5 different initial positions as a function of axial position in 99% Ar-1%H_2 ICTPs.

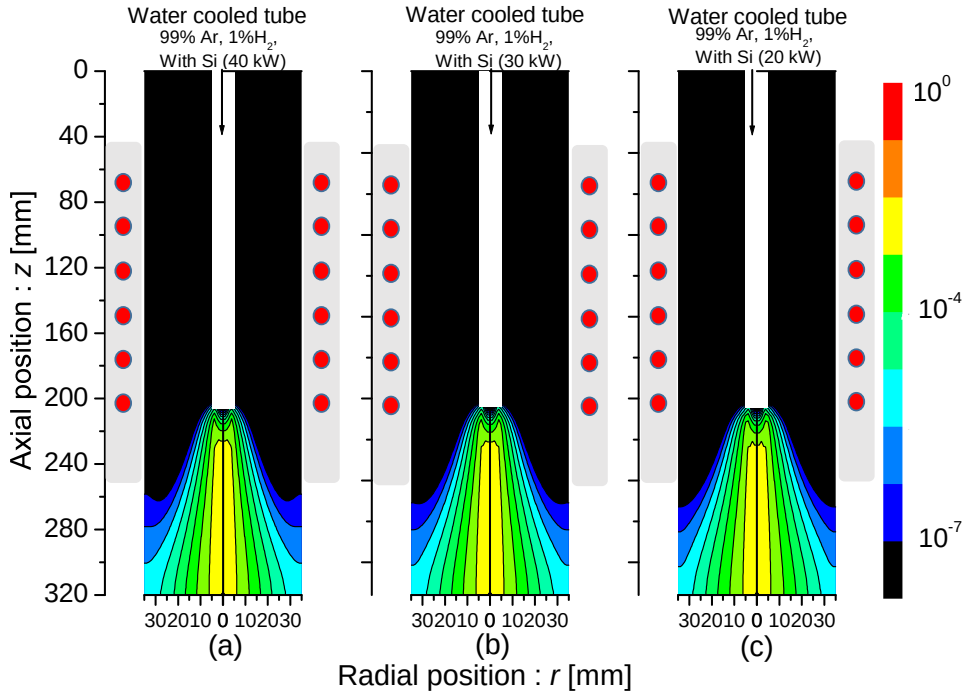

Fig. 2.6: Mass fraction distribution of 99% Ar-1%H_2 ICTPs with Si powder injection at input powers of 20 kW, 30 kW and 40 kW.

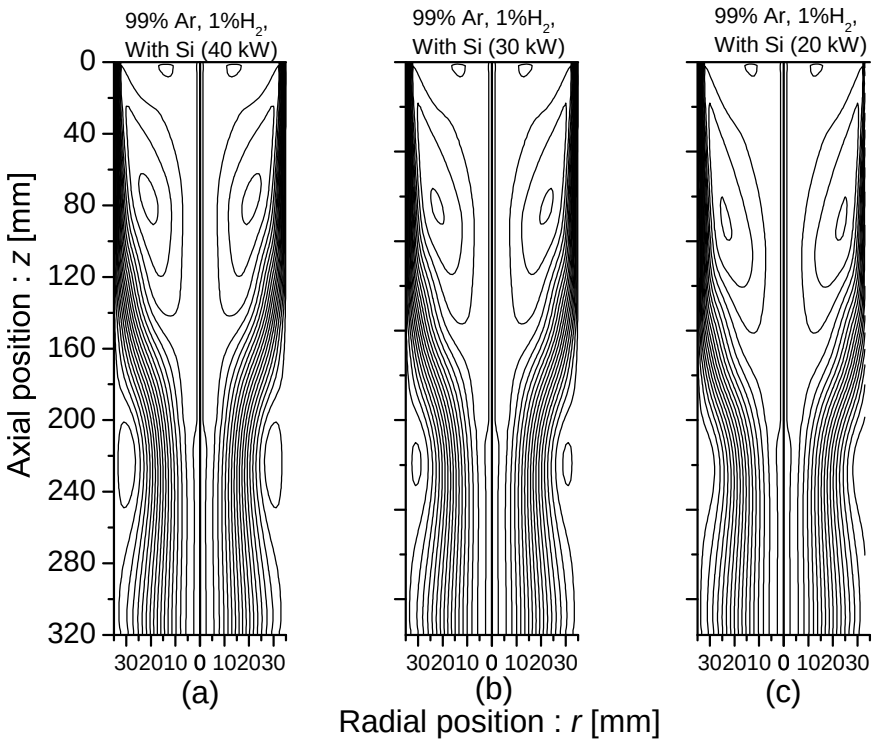

Fig. 2.7: Streamlines in 99% Ar-1%H_2 ICTPs with Si powder injection at input powers of 20 kW, 30 kW, and 40 kW.

2.5 Summary of chapter 2

This research investigated the influence of input power on the temperature distribution in argon (Ar) and hydrogen (H_2) induction thermal plasma with silicon (Si) powder injection. The calculated temperature distributions of 99%Ar-1%H_2 thermal plasma and Si powder injection were compared with different input powers of 20 kW, 30 kW, and 40 kW. Results indicated that higher input power increases the temperature of the thermal plasma but it slightly enhances evaporation of the powder at the center axis of the plasma torch. This numerical calculation research was made to obtain temperature field and gas flow field and evaporated mass fraction from very complicated interactions between thermal plasma and particle injection, which cannot be understood only by experiments. The calculated temperature distributions of 99% Ar-1%H_2 thermal plasma and Si powder injection were compared with different input powers of 20 kW, 30 kW, and 40 kW. Results indicated that higher input power increases the temperature of the thermal plasma with doughnut shape but it slightly enhances evaporation of the powder at the center axis of the plasma torch.

References

[1] S. Gottlieb, N. Wohrl, S. Schulz, V. Buck : "Simultaneous synthesis of nanodiamonds and graphene via plasma enhanced chemical vapor deposition (MW PE-CVD) on copper" *SpringerPlus* **5:568** pp.1-16 (2016)

[2] K.S. Kim, A. Moradian, J. Mostaghimi, G. Soucy : " Modeling of induction plasma process for fullerene synthesis: Effect of plasma gas composition and operating pressure" *Plasma Chemistry and Plasma Processing* **30** pp. 91-110 (2010)

[3] P.-J. Chu, S.-Y. Wu, K.-C. Chen, J.-L. He, A. Yerokhin, A. Matthews : "Nanostructured TiO_2 films by plasma electrolytic oxidation combined with chemical and thermal post-treatments of titanium, for dye-sensitized solar cell applications" *Thin Solid Films* **519** pp. 1723-1728 (2010)

[4] Shigeta : "Numerical investigation of nano-material processing by thermal plasma flows" *Proceedings of the Joint Workshop on High Performance Computing on Vector Systems, and Workshop on Sustained Simulation Performance, Sendai* pp. 169-182 (2013)

[5] T. Shigaki and J. G. Li : "Synthesis of functional nanocrystallites through reactive thermal plasma processing" *Sci. Technol. Adv. Mater* **8** pp. 617623 (2007)

[6] L. Tong and R. G. Reddy : "Thermal plasma synthesis of SiC nano-powders/nanofibers" *Mater. Res. Bull* **41** pp. 2303-2310 (2006)

[7] M. Shigeta, T. Watanabe and H. Nishiyama : "Numerical investigation for nanoparticle synthesis in an RFinductively coupled plasma." *Thin Solid Films* **457** pp. 192200 (2004)

[8] J. Mao, M. Liu, C.G. Deng, C.M. Deng, K.S. Zhou, Z.Q. Deng : "Preparation and distribution analysis of thermal barrier coatings deposited on multiple vanes by plasma

spray-physical vapor deposition technology" *Journal of Engineering Materials and Technology, Transactions of the ASME* **139** (2017)

[9] W. G. Mao, Y. Y. Chen, Y. J. Wang, M. Zhou, H. Y. Yang, Z. Wang, C. Y. Dai, X. Chen, D. N. Fang : "A multilayer structure shear lag model applied in the tensile fracture characteristics of supersonic plasma sprayed thermal barrier coating systems based on digital image correlation" *Elsivier, Surface and Technology* **350** pp. 211226 (2018)

[10] C. Wang, Y. Tanaka and T. Sakuta : "Modeling of Ar Induction Thermal Plasma with an Injection of PTFE Powder" *Trans. IEEJ* **124-PE** pp. 440-46 (2004)

[11] Y. Takeuchi, Y. Tanaka, Y. Uesugi, S. Kaneko and S. Okabe : "Numerical simulation of thermal interaction between polymer and Ar induction thermal plasma" *Trans. IEEJ* **127-PE** pp. 739-46 (2007)

[12] Y Tanaka, Y Takeuchi, Y Uesugi, S. Kaneko, S. Okabe : "Numerical and experimental investigations on thermal interaction between thermal plasma and solid polymer poeders using induction thermal plasma technique" *J. Phys. D: Appl. Physr* **41** pp. 025203 (2008)

[13] Y. Tanaka and T. Sakuta : "Investigation of plasma-quenching efficiency of various gases using induction thermal plasma technique: effect of various gas injection on Ar thermal ICP" *Journal of Physics D: Applied Physics* **35** pp. 2149-58 (2002)

[14] Y. Siregar, N. Kodama, Y. Tanaka, T. Ishijima, Y. Uesugi : "Numerical simulation on thermal plasma temperature field in torch for different conditions" *IOP Conf. Series: Materials Science and Engineering* **309** pp. 012090 (2018)

[15] Q.J. Guo, G.H. Ni, Li.Li, Q.FLin, Y.J. Zhao, S.Y. Sui, H.B. Xie, W.X. Duan, Y.D, Meng : "Effects of input power, gas flow rate and hydrogen concentration on Cu film deposition by a radio frequency driven non-thermal atmospheric pressure plasma jet" *Elsevier, Thin Solid Films* **660** pp. 493498 (2018)

[16] V. Colombo, E. Ghedini, M. Gherardi and P. Sanibondi : "Evaluation of precursor evaporation in Si nanoparticle synthesis by inductively coupled thermal plasmas" *IOP*

Publishing **22** pp. 035010 (2013)

[17] P. Proulx, J. Mostaghimi and M.I. Boulos : "Plasma particle interaction effects in induction plasma modeling under dense loading conditions" *Int. J. Heat Mass Transfer* **28** pp. 1327-1336 (1985)

[18] P. Proulx, J. Mostaghimi and M.I. Boulos : "Heating of powder in an r.f. inductively coupled plasma under dense loading conditions" *Plasma Chem. Plasma Process.* **7** pp. 29-52 (1987)

[19] J. Mostaghimi, P. Proulx, M.I. Boulos : "An analysis of the computer modeling of the flow and temperature fields in an inductively coupled plasma" *Numerical Heat Transfer* **8** pp. 187-201 (1985)

[20] J.M. Yos : "Transport properties of nitrogen, hydrogen, oxygen and air to 30 000 K", *AVCO Technical Memorandum RAD-TM* **196401** pp.73 (1963)

[21] S. Chapman and T.G. Cowling : "The Mathematical Theory of Non-Uniform Gases Third Edition" *Cambridge University Press* (1970)

[22] R.S. Devoto : "Transport coefficients of partially ionized argon" *Phys. Fluid* **10** pp. 354-64 (1967)

[23] J. G. Li, M. Ikeda, R. Ye, Y. Moriyoshi and T. Ishigaki : "Control of particle size and phase formation of TiO2 nanoparticles synthesized in RF induction plasma" *J. Phys. D: Appl. Phys* **40** pp. 23482353 (2007)

[24] R.S. Devoto : "Transport coefficients of partially ionized argon" *Phys. Fluid* **10** pp. 354-64 (1967)

[25] M. Wei, B. He, Q. Liang, S. Somasundaram, C. Seng Than, E. N. Wang : "Optimization and thermal characterization of uniform silicon micropillar based evaporators" *Elsevier, International Journal of Heat and Mass Transfer.* **127** pp. 5160 (2018)

—

Chapter 3

Numerical Parametric Investigation on Temperature Distribution in Ar/O_2 Induction Thermal Plasmas with Ti Powder Injection -Inclusion of Particle Evaporation-

3.1 Introduction

The high-pressure and high-power inductively coupled thermal plasma (ICTP) is widely used as a chemical reaction source and an effective heat source for various materials processing. One benefit of the ICTP is to have higher radical density and higher enthalpy without any impurity contamination because the high power ICTP is sustained by electromagnetic coupling without any electrodes. Another benefit of the ICTP in materials processing is that such an ICTP can provide a one-step direct processing including rapid evaporation of injected raw materials and then rapid cooling of evaporated materials. From the above benefits, the ICTP has been well adopted for synthesis of fullerene, fabrication of diamond films [1], materials surface modifications [2], and thermal barrier coatings [3], etc. Recently in addition, the ICTP is widely used for synthesis of nanometer's. For example, synthesis of TiO_2 nanoparticles [4] are continually receiving attention for use as phonic crystals, photocatalysts [5], gas sensors [6] and photovoltaic cells [7].

To consider the process of nanoparticle synthesis, it is very important to understand

thermal interaction between feedstock powder injected and high-temperature field in the ICTP. In the high-temperature field, the injected feedstock powder is heated to elevate its temperature, which results in its melting and then evaporation. The evaporation of feedstock material can change the temperature field because of powder consumption, and also the gas flow field due to mass source from the evaporation. In addition, the evaporated material can contaminates the ICTP, which can greatly change the thermodynamic and transport properties of the ICTP. Further, the above change in the properties can affect the temperature distribution and gas flow field in the ICTP. These sequential change from feedstock powder injection to evaporation in steady state is extremely complex. To elucidate these complex phenomena, numerical simulation is one strong tool nowadays. The interaction between thermal plasma and solid particles were studied by many researchers, and several numerical models including the above interactions have been developed over 30 years [8]$^-$ [28]. Actually, we have developed a numerical simulation model of the Ar ICTP with Si powder or C powder feedstock previously [15].

Thermal interaction with high-temperature field and feedstock powder in the ICTP is important to understand nanoparticle synthesis processes. Contamination of their vapor and evaporation of the feedstock to the ICTP can change transport and thermodynamic properties of the ICTP markedly. This change in the transport and thermodynamic properties can also vary temperature fields and gas flow in the ICTP. Such the vapor contamination, a sequence of evaporation of the feedstock and transport is extremely complex in the ICTP. We have investigated this complex phenomena numerically in Ar ICTP [15]. However, there are a lot of operation parameters in this process such as feedstock feeding rate, sheath gas rate, and input power of the Ar ICTP. In addition, in actual nanoparticle synthesis, molecular gas injection is injected to the ICTP. The above operation parameters all affects the whole process in the ICTP. Especially, for nanoparticle synthesis, feedstock vapor with high mass fraction should be created by controlling operating parameters. Thus, it is necessary to study the influence of operation parameter on the thermal plasma fields.

This paper describes numerical investigation results on thermal interaction in Ar-O_2 ICTP with titanium (Ti) feedstock powder injection for TiO_2 nanoparticle synthesis. Especially, evaporation of Ti feedstock was treated in Ar-O_2 ICTP. For this purpose, first the equilibrium composition of Ar-O-Ti system was calculated to find dominant species and

by products in temperature range of 300-3000 K. The calculated composition was utilized to compute the thermodynamic and transport properties of Ar-Ti-O vapor. After that, the temperature distribution was calculated by numerical thermo-fluid simulation for the ICTP with considering evaporation of the many injected Ti feedstock particles. Influences of feedstock feeding rate, sheath gas flow rate and input power were investigated for evaporation process of the Ti feedstock as well as the temperature field and the mass fraction of Ti vapor in the ICTP torch. Results provide fundamental operation parameter dependences which is useful to consider the parametric design of the ICTP with powder. The contribution of this paper is to provide the equilibrium composition of Ar-Ti-O system, thermodynamic and transport properties of Ar-Ti-O system, and also parametric investigation data on the temperature distribution of Ar-O_2 ICTP. In particular, inclusion of O_2 in Ar ICTP increases the enthalpy of thermal plasmas due to dissociation and association reactions, which makes the thermal plasma properties complex. Although the calculation methods are based on the ones developed by many researchers, the obtained data will be helpful to design the plasma torch with powder injection because it contains comprehensive characteristic features such as gas flow pattern, plasma temperature distribution, evaporation position and then mass fraction of Ti vapor for various operation parameters in one paper.

3.2 Configuration of inductively coupled thermal plasmatorch

Figure 4.1 depicts the configuration of the inductively coupled thermal plasma torch used in this research. The plasma torch comprises two coaxial quartz tubes with 320 mm in length. The inner quartz tube has a thickness of 3 mm with 35 mm in internal radius. Between the inner quartz tube and the outer quartz tube, cooling water flows to keep the wall temperature around 300 K. Around the outer quartz tube, an eight-turn induction coil is installed. The radius of the coil is 58 mm. To this coil, the radio-frequency (rf) coil current is supplied to generate electromagnetic field inside the plasma torch from an rf power source. The coil current frequency is 450 kHz. On the other hand, from the head of the plasma torch, argon (Ar) and oxygen (O_2) gas mixture is supplied as a sheath gas.

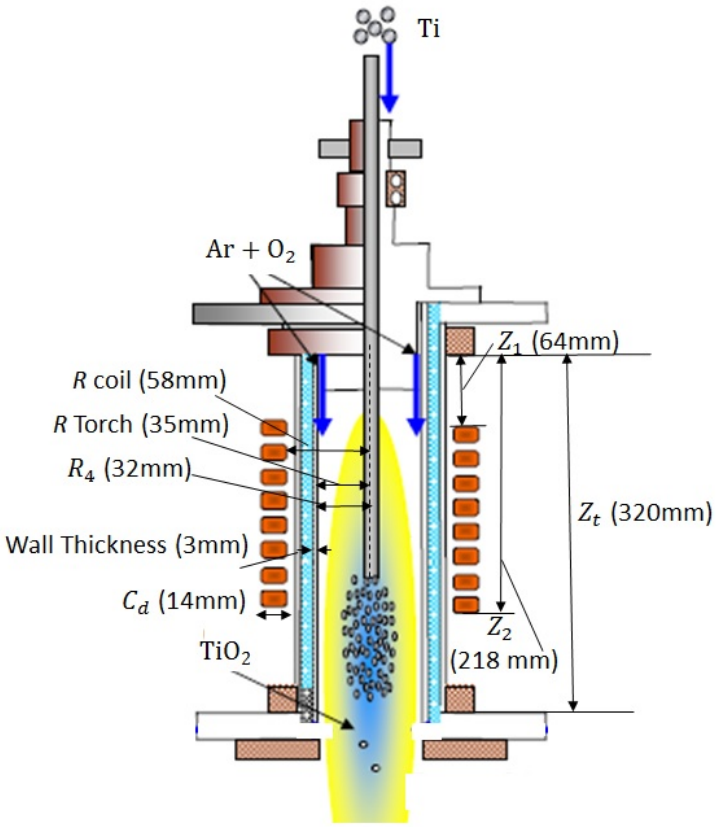

Fig. 3.1: Configuration of inductively coupled thermal plasma torch used in the calculation.

This sheath gas is supplied along the inner quartz tube wall with a swirl to prevent the plasma from contacting the inner quartz tube. The electromagnetic field generated by the coil current can accelerate an electron inside the torch, and a plasma can be formed there if the electron impact ionization occurs. At high pressure near atmospheric pressure, the thermal plasma with high gas temperature is generated without any electrode. This is called inductively coupled thermal plasma (ICTP). One feature of the ICTP is the high gas temperature, high enthalpy without any contamination from the electrodes. As for feedstock, titanium (Ti) feedstock powder was injected to the high temperature region of the ICTP directly through the water-cooled tube with Ar carrier gas flow. This water-cooled tube installed from the top of the plasma torch head deeply into the torch. This condition is similar to the one for TiO_2 nanoparticle synthesis.

For numerical calculation of ICTP with titanium powder injections, the calculation space was set to the two-dimensional cylindrical $r - z$ cross section of this plasma torch.

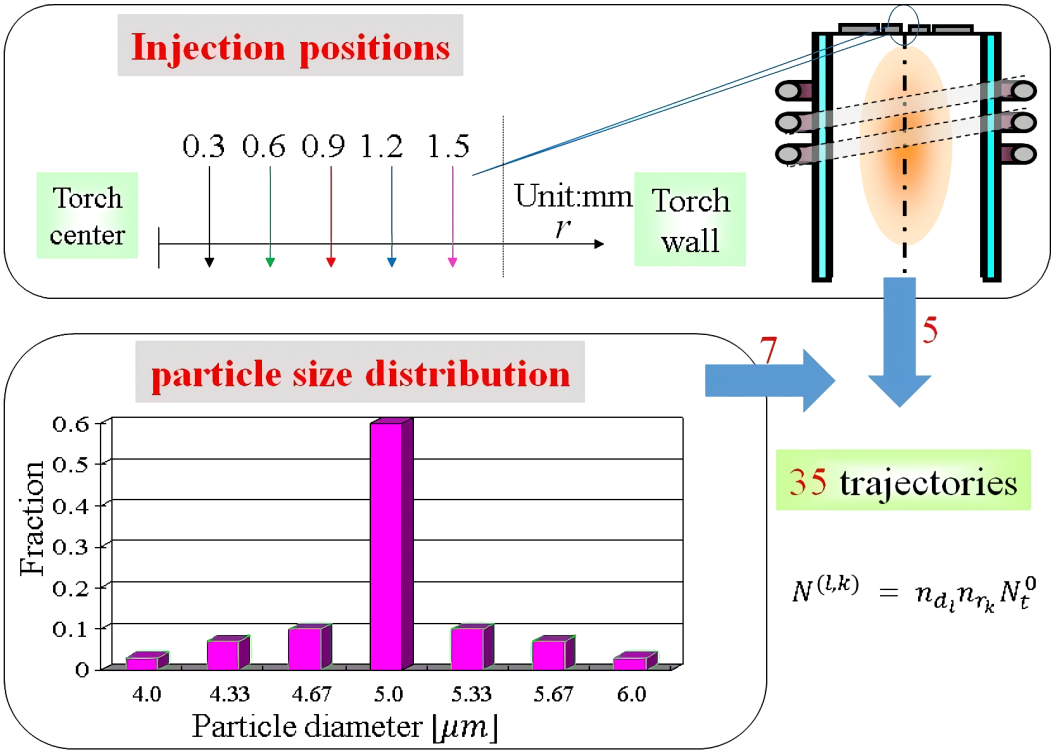

Fig. 3.2: Initial positions of particle injections and particle size distribution.

3.3 Modeling

3.3.1 Assumptions

The developed model is based on the PSI-Cell concept developed by Crowe *et al* [26]; it is an extension of the work by Proulx and co-workers [27,28]. In modeling, the following assumptions were made: (i) The plasma is in local thermodynamic equilibrium; consequently, all the temperatures such as the electron temperature, heavy particle temperature, and excitation temperatures are identical. In addition, the model assumes chemical equilibrium conditions for all reactions. (ii) The plasma is optically thin for wavelengths greater than 200 nm. For wavelengths of less than 200 nm, 20% of the total emission coefficient is accounted for radiation loss to consider the effective light absorption [4, 29]. (iii) The flow is steady, laminar, and axis-symmetric, with negligible viscous dissipation. (iv) For injected particles, the particle-particle interactions are neglected. (v) The particle radius is much smaller than the mean free path of plasma components. (vi) The particle is always spherical even during and after melting and evaporation. (vii) Particle surface is uniformly heated

from thermal plasmas. Thus, evaporation also uniformly occurs around the particle surface. (viii) Effects of electric charging on the particle are neglected. (ix) The rocket effect from ejected ablation vapor is neglected. (x) Titanium feedstock particles are evaporated by the heat from the thermal plasma.

3.3.2 Governing equation for Ti particle

Assuming that only forces affecting an individual feedstock particle are drag and gravity, the momentum equation for a Ti single particle into the plasma can be written by

$$\frac{du_{\mathrm{p}}}{dt} = -\frac{3}{4}C_{\mathrm{D}}(u_{\mathrm{p}} - u)U_{\mathrm{R}}(\frac{\rho}{\rho_{\mathrm{p}}d_{\mathrm{p}}}) + g \tag{3.1}$$

$$\frac{dv_{\mathrm{p}}}{dt} = -\frac{3}{4}C_{\mathrm{D}}(v_{\mathrm{p}} - v)U_{\mathrm{R}}(\frac{\rho}{\rho_{\mathrm{p}}d_{\mathrm{p}}}) + \frac{w_{\mathrm{p}}^2}{r} \tag{3.2}$$

$$\frac{dw_{\mathrm{p}}}{dt} = -\frac{3}{4}C_{\mathrm{D}}(w_{\mathrm{p}} - w)U_{\mathrm{R}}(\frac{\rho}{\rho_{\mathrm{p}}d_{\mathrm{p}}}) \tag{3.3}$$

$$U_{\mathrm{R}} = \sqrt{(u_{\mathrm{p}} - u)^2 + (v_{\mathrm{p}} - v)^2 + (w_{\mathrm{p}} - w)^2}, \tag{3.4}$$

where C_{D} is the drag coefficient, u_{p} is the axial velocity of the Ti particle, v_{p} is the radial velocity of the particle, w_{p} is the swirl velocity of the particle, U_{R} is the relative velocity between the plasma and Ti particle, ρ_{p} is the mass density of the Ti particle in solid and liquid phases, d_{p} is the Ti particle diameter, and g is the gravitational acceleration. In addition, the directions of particles at the outlet of the injection powder feeding tube were set randomly to three angle directions to simulate reflections of particles with the tube inner wall [24].

The energy conservation equation for particles is expressed with consideration of the thermal conduction inside the particle. In this model, the particle was divided into several shells to treat the temperature gradient inside the particle. In addition, we defined the temperature $T_{\mathrm{p}}(r,t)$ and the liquid fraction $\chi(r,t)$ of each shell which depends on the radial position r and the time t. In this case, the energy conservation equation of the particle is expressed as follows:

-Inner shells ($0 < r \leq d_{\mathrm{p}-1}/2$):

$$\rho_{\mathrm{p}}C_{\mathrm{pp}}\frac{\partial T_{\mathrm{p}}(r,t)}{\partial t} = \frac{1}{r^2}\frac{\partial}{\partial r}(r^2\lambda_{\mathrm{p}}\frac{\partial T_{\mathrm{p}}(r,t)}{\partial r})$$
$$(T_{\mathrm{p}}(r,t) < T_{\mathrm{m}},\, T_{\mathrm{m}} < T_{\mathrm{p}}(r,t) < T_{\mathrm{b}}) \tag{3.5}$$

$$\rho_{\mathrm{p}} H_{\mathrm{m}} \frac{\partial \chi(r,t)}{\partial t} = \frac{1}{r^2}\frac{\partial}{\partial r}(r^2 \lambda_{\mathrm{p}} \frac{\partial T_{\mathrm{p}}(r,t)}{\partial r}) \quad (T_{\mathrm{p}}(r,t) = T_{\mathrm{m}}) \tag{3.6}$$

where C_{pp}: the specific heat of the Ti particle in solid or liquid phases, $T_{\mathrm{p}}(r,t)$: the shell temperature inside the particle, T_{m}: the melting temperature of Ti, T_{b}: the boiling temperature of Ti, λ_{p}: the thermal conductivity of Ti bulk, H_{m}: the latent heat for melting, $\chi(r,t)$: liquid fraction of the shell.

At the outer shell, we considered not only thermal conduction to the inside of the particle but also heat transfer from the plasma and radiation transfer:

-Outer shell ($r > d_{\mathrm{p-1}}/2$):

$$\frac{1}{6}\pi(d_{\mathrm{p}}^3 - d_{\mathrm{p-1}}^3) \cdot \rho_{\mathrm{p}} C_{\mathrm{pp}} \frac{\partial T_{\mathrm{p}}(r_{\mathrm{out}},t)}{\partial t} = Q \quad (T_{\mathrm{p}}(r_{\mathrm{out}},t) < T_{\mathrm{m}},\ T_{\mathrm{m}} < T_{\mathrm{p}}(r_{\mathrm{out}},t) < T_{\mathrm{b}}) \tag{3.7}$$

$$\frac{1}{6}\pi(d_{\mathrm{p}}^3 - d_{\mathrm{p-1}}^3) \cdot \rho_{\mathrm{p}} H_{\mathrm{m}} \frac{\partial \chi(r_{\mathrm{out}},t)}{\partial t} = Q \quad (T_{\mathrm{p}}(r_{\mathrm{out}},t) = T_{\mathrm{m}}) \tag{3.8}$$

$$\frac{\pi d_{\mathrm{p-1}}^2}{2} \cdot \rho_{\mathrm{p}} H_{\mathrm{v}} \frac{\partial (d_{\mathrm{p}})}{\partial t} = Q \quad (T_{\mathrm{p}}(r_{\mathrm{out}},t) = T_{\mathrm{b}}) \tag{3.9}$$

$$\begin{aligned} Q &= -\pi d_{\mathrm{p-1}}^2 \lambda_{\mathrm{p}} \left.\frac{\partial T_{\mathrm{p}}}{\partial r}\right|_{r=d_{\mathrm{p-1}}/2} \\ &+ \pi d_{\mathrm{p}}^2 h_c (T - T_{\mathrm{p}}(r_{\mathrm{out}},t)) \\ &- \pi d_{\mathrm{p}}^2 \sigma_{\mathrm{s}} \epsilon (T_{\mathrm{p}}(r_{\mathrm{out}},t)^4 - T_{\mathrm{a}}^4) \end{aligned} \tag{3.10}$$

In those equations, we used the following variables: $d_{\mathrm{p-1}}$: the outer shell's inner diameter, r_{out}: the radial position of the control volume of the outer shell, H_{v}: the latent heat for evaporation, Q: the heat at the outer shell from the thermal plasma, T: the thermal plasma temperature, ϵ: the particle surface emissivity, T_{a}: the ambient temperature, σ_{s}: the Stefan-Boltzmann coefficient, h_{c}: the heat transfer coefficient between thermal plasma and titanium. The quantities C_{D} and h_{c} were given as a function of particle Reynolds number [27].

3.3.3 The drag force coefficient and heat transfer coefficient

3.3.4 The drag force coefficient and heat transfer coefficient

The drag force used in this calculation is the drag force coefficient with correction factors due to the small size and the steep temperature gradient by following equation [8]$^-$ [10]:

$$C_{\mathrm{D}} = C_{\mathrm{Df}} \cdot f_1 \cdot f_2 \tag{3.11}$$

where C_{Df} is the ordinary drag force coefficient, f_1 is the correction factor from steep temperature gradient, f_2 is the correction factor from the small size. The ordinary drag force coefficient C_{Df} was used dependent on particle Reynolds number [28]:

$$C_{\mathrm{Df}} = \begin{cases} 24/Re & (Re \leqslant 0.2) \\ 24(1+0.1875Re)/Re & (0.2 < Re \leqslant 2) \\ 24(1+0.11Re^{0.81})/Re & (2 < Re \leqslant 21) \\ 24(1+0.189Re^{0.62})/Re & (21 < Re \leqslant 200) \\ 24(1+0.15Re^{0.687})/Re & (Re \geqslant 200) \end{cases}$$

where Re is the particle Reynolds number and the relative velocity between the gas and the particle. The correction factors are needed for the drag coefficients because the temperature drops drastically in the boundary area and, accordingly, there are property variations across the boundary area. Furthermore, the steep temperature gradients between the particles and their surroundings as well as the highly nonlinear plasma properties. The correction factors adopted here are [8]$^-$ [10]

$$f_1 = \left(\frac{\rho_\infty \mu_\infty}{\rho_{\mathrm{w}} \mu_{\mathrm{w}}} \right)^{-0.45} \tag{3.12}$$

where the subscripts ∞ represents surrounding plasma properties, subscripts w is the properties at particle surface temperature. Another important for correction factor due to the small size particles [10]. The following correction factor is used in this calculation:

$$f_2 = \left[1 + \left(\frac{2-a}{a} \right) \left(\frac{\gamma}{1+\gamma} \right) \frac{4}{Pr_{\mathrm{w}}} Kn^* \right]^{-0.45} \tag{3.13}$$

where γ is the specific heat ratio, a is the thermal accommodation coefficient, Kn^* is the Knudsen number based on an effective mean free path length, Pr_{w} is the Prandtl number of the gas at the surface temperature of the particle.

The heat transfer coefficient h_{c} was estimated by [8, 10, 27, 28]:

$$h_{\mathrm{c}} = \frac{Nu_{\mathrm{f}}}{d_{\mathrm{p}}}\lambda_{\mathrm{p}} \tag{3.14}$$

$$Nu_{\mathrm{f}} = (2 + 0.515Re^{1/2}{Pr_{\mathrm{f}}}^{1/3})\left(\frac{\rho_\infty \mu_\infty}{\rho_{\mathrm{w}}\mu_{\mathrm{w}}}\right)^{0.6}\left(\frac{C_{\mathrm{p}\infty}}{C_{\mathrm{pw}}}\right)^{0.38} \tag{3.15}$$

where Nu_{f} is Nusselt number, C_{pw} is specific heat at the particle surface, $C_{\mathrm{p}\infty}$ is specific heat at the surrounding plasma.

3.3.5 Governing equation for thermal plasma region

On the basis of the assumptions described above, the thermal plasma is governed by the following equations [15] [23] [18]:

Mass conservation.

$$\frac{\partial(\rho u)}{\partial z} + \frac{1}{r}\frac{\partial(r\rho v)}{\partial r} = S_{\mathrm{p}}^{C} \tag{3.16}$$

Momentum conservation.

Axial:

$$\begin{aligned} &\rho u\frac{\partial u}{\partial z} + \rho v\frac{\partial u}{\partial r} \\ &= -\frac{\partial p}{\partial z} + 2\frac{\partial}{\partial z}(\eta\frac{\partial u}{\partial z}) \\ &+ \frac{1}{r}\frac{\partial}{\partial r}[\eta r(\frac{\partial u}{\partial r} + \frac{\partial v}{\partial z})] + \mu_0\sigma\Re[\dot{E}_\theta \dot{H}_r^*] + S_{\mathrm{p}}^{M_z} \end{aligned} \tag{3.17}$$

Radial:

$$\begin{aligned} &\rho u\frac{\partial v}{\partial z} + \rho v\frac{\partial v}{\partial r} \\ &= -\frac{\partial p}{\partial r} + \frac{\partial}{\partial z}[\eta(\frac{\partial v}{\partial z} + \frac{\partial u}{\partial r})] \\ &+ \frac{2}{r}\frac{\partial}{\partial r}(\eta r\frac{\partial v}{\partial r}) - 2\eta\frac{v}{r^2} + \frac{\rho w^2}{r^2} \\ &+ \mu_0\sigma\Re[\dot{E}_\theta \dot{H}_z^*] + S_{\mathrm{p}}^{M_z} \end{aligned} \tag{3.18}$$

Swirl:

$$\begin{aligned}\rho u\frac{\partial w}{\partial z}+\rho v\frac{\partial w}{\partial r}&\\ =\ \frac{\partial}{\partial z}\left(\eta\frac{\partial w}{\partial z}\right)+\frac{1}{r}\frac{\partial}{\partial r}\left(r\eta\frac{\partial w}{\partial r}\right)&\\ -\ \frac{\rho vw}{r}-\frac{w}{r}\frac{\partial r\eta}{\partial r}&\end{aligned} \tag{3.19}$$

Energy conservation.

$$\begin{aligned}\rho u\frac{\partial h}{\partial z}+\rho v\frac{\partial h}{\partial r}&\\ =\ \frac{\partial}{\partial z}(\frac{\lambda}{C_{\rm p}}\frac{\partial h}{\partial z})+\frac{1}{r}\frac{\partial}{\partial r}(r\frac{\lambda}{C_{\rm p}}\frac{\partial h}{\partial r})&\\ +\ \sigma|\dot{E}_\theta|^2-P_{\rm rad}-S_{\rm p}^E&\end{aligned} \tag{3.20}$$

Mass transport equation for Ti vapor.

$$\begin{aligned}\rho u\frac{\partial Y_{\rm Ti}}{\partial z}+\rho v\frac{\partial Y_{\rm Ti}}{\partial r}&\\ =\ \frac{\partial}{\partial z}(\rho D_{\rm Ar/O_2-Ti}\frac{\partial Y_{\rm Ti}}{\partial z})+\frac{1}{r}\frac{\partial}{\partial r}(r\rho D_{\rm Ar/O_2-Ti}\frac{\partial Y_{\rm Ti}}{\partial r})+S_{\rm p}^C&\end{aligned} \tag{3.21}$$

Maxwell equation.

$$\frac{\partial^2\dot{A}_\theta}{\partial z^2}+\frac{1}{r}\frac{\partial}{\partial r}(r\frac{\partial\dot{A}_\theta}{\partial r})-\frac{\dot{A}_\theta}{r^2}=j\mu_0\sigma\omega\dot{A}_\theta \tag{3.22}$$

$$\dot{H}_z=\frac{1}{\mu_0}\frac{1}{r}\frac{\partial}{\partial r}(r\dot{A}_\theta),\quad \dot{H}_r=-\frac{1}{\mu_0}\frac{\partial\dot{A}_\theta}{\partial z} \tag{3.23}$$

$$\dot{E}_\theta=-j\omega\dot{A}_\theta \tag{3.24}$$

In those equations, the followings pertain: r: radial position, z: axial position, u: axial flow velocity, v: radial flow velocity, ρ: mass density, p: pressure, η: viscosity, h: enthalpy, λ: thermal conductivity, $C_{\rm p}$: specific heat at constant pressure, σ: electrical conductivity, $P_{\rm rad}$: radiative loss, $Y_{\rm Ti}$: mass fraction of Ti vapor, $D_{\rm Ar/O_2-Ti}$: effective diffusion coefficient of Ti vapor in Ar/O_2 gas, μ_0: permeability of vacuum, $\dot{A}_\theta$: vector potential, ω: angular frequency of the coil current, $\dot{E}_\theta$: electric field strength, $\dot{H}_z$, $\dot{H}_r$: axial and radial components, of the magnetic field strength, respectively, j: complex factor (j^2=−1). The vector potential $\vec{A}(r,z,t)$ has only an azimuthal component $\vec{A}(r,z,t)=(0,\sqrt{2}\dot{A}_\theta e^{j\omega t},0)$, where the phasor $\dot{A}_\theta$ has a real and an imaginary part like $\dot{A}_\theta=A_{\theta R}+jA_{\theta I}$. The magnitudes of the phasor

including $\dot{A}_\theta$, $\dot{E}_\theta$, $\dot{H}_z$ and $\dot{H}_r$ are defined as the root mean square values. The asterisks * in Eqns. (4.11) and (4.12) indicate the conjugate, and a symbol $\Re$ is the real part of the phasor. The above momentum equation omitted a term $-\nabla \cdot \frac{1}{3}\eta(\nabla \cdot \vec{u})[I]$ for simplicity where $[I]$ is the unit tensor. The quantities S_{p}^{C}, $S_{\mathrm{p}}^{M_z}$, $S_{\mathrm{p}}^{M_r}$, and S_{p}^{E} indicate source terms by the translation quantities from evaporated material. These quantities are described in the next section. The calculation was made by SIMPLER algorithm after Patankar.

3.3.6 Interaction between Ti particle and thermal plasma

The titanium particles are regarded as sources of mass, momentum, and energy of plasma equations. Here we take N_t^0 as the number of particles injected per unit time, while n_d corresponds to the particle size distribution, and n_r represents the fraction of N_t^0 injected at each point in the water-cooled tube. The number of particles per time traveling along the trajectory (l, k) with a particle diameter d_l injected at point r_k can be written by the following:

$$N^{l,k} = n_{d_l} n_{r_k} N_{\mathrm{t}}^0 \tag{3.25}$$

In this calculation, the particle concentration n_r at the inlet was assumed to be uniform for five positions of particle starting. Figure 3.2 shows the initial positions of particle injection and the initial particle size distribution. Particles are assumed to be injected at five radial positions of r =0.3 mm, 0.6 mm, 0.9 mm, 1.2 mm and 1.5 mm. On the other hand, the powder was assumed to consist of particles with seven discrete diameters, as shown in lower panel in Fig. 3.2. Furthermore, these seven discrete diameter particles were assumed to have a Gaussian distribution fraction. In this case, 60% of the whole particles has mean diameter of 5.0 μm, 10% of those have diameters of 4.67 μm, and 5.33 μm, 7% of the particles have diameter of 4.33 μm and 5.67 μm, and remaining 3% of the particles have diameters of 4.0 μm and 6.0 μm. Those conditions offer 7×5=35 possible particle trajectories. Thus, there are 35 trajectories for particles with 7 different diameters and 5 different initial positions. This calculation of 35 trajectories was done for statistical calculation on the particle size change and its influence on the thermal plasma temperature. The initial particle injection velocity was set equal to the carrier gas velocity. The source term in the mass conservation equation S_{p}^{C} is the net mass efflux rate from the particle in

a computational cell (control volume). On the assumption of the spherical particles, the mass efflux rate from the particles during the particle trajectory (l,k) traversing a given cell (i,j) is as follows:

$$S_{\mathrm{p},ij}^{C(l,k)} = \frac{1}{6}\pi\rho_{\mathrm{p}}N_{ij}^{(l,k)}(d_{ij,\mathrm{in}}^3 - d_{ij,\mathrm{out}}^3). \tag{3.26}$$

The net mass efflux rate from the particle can be derived by summing over all particle trajectories traversing a given cell:

$$S_{\mathrm{p},ij}^{C} = \sum_l \sum_k S_{\mathrm{p},ij}^{C(l,k)}. \tag{3.27}$$

The momentum source terms were calculated in the similar way as the particle mass source terms. In this case, the efflux rate of particle momentum attributable to the particle trajectory (l,k) traversing a given cell (i,j), which are describe as the quantities $S_{\mathrm{p}}^{M_z}$ and $S_{\mathrm{p}}^{M_z}$, is given by

$$S_{\mathrm{p},ij}^{M_z(l,k)} = \frac{1}{6}\pi\rho_{\mathrm{p}}N_{ij}^{(l,k)}(u_{ij,\mathrm{in}}d_{ij,\mathrm{in}}^3 - u_{ij,\mathrm{out}}d_{ij,\mathrm{out}}^3) \tag{3.28}$$

$$S_{\mathrm{p},ij}^{M_r(l,k)} = \frac{1}{6}\pi\rho_{\mathrm{p}}N_{ij}^{(l,k)}(v_{ij,\mathrm{in}}d_{ij,\mathrm{in}}^3 - v_{ij,\mathrm{out}}d_{ij,\mathrm{out}}^3), \tag{3.29}$$

and the corresponding momentum source terms are

$$S_{\mathrm{p},ij}^{M_z} = \sum_l \sum_k S_{\mathrm{p},ij}^{M_z(l,k)} \tag{3.30}$$

$$S_{\mathrm{p},ij}^{M_r} = \sum_l \sum_k S_{\mathrm{p},ij}^{M_r(l,k)}. \tag{3.31}$$

The energy source term contains the heat given to the particles $Q_{\mathrm{p},ij}^{(l,k)}$, and the superheat to bring the particle vapor into thermal plasma $Q_{\mathrm{v},ij}^{(l,k)}$. The quantity S_{p}^{E} is written by $Q_{\mathrm{p},ij}^{(l,k)}$ and $Q_{\mathrm{v},ij}^{(l,k)}$ as follows:

$$Q_{\mathrm{p},ij}^{(l,k)} = \int_{\tau_{\mathrm{in}}}^{\tau_{\mathrm{out}}} \pi d_{\mathrm{p}}^2 h_c[T_{ij} - T_{\mathrm{p},ij}^{(l,k)}]dt \tag{3.32}$$

$$Q_{\mathrm{v},ij}^{(l,k)} = \int_{\tau_{\mathrm{in}}}^{\tau_{\mathrm{out}}} \frac{\pi}{2} d_{\mathrm{p}}^2 \rho_{\mathrm{p}} \left(\frac{dd_{\mathrm{p}}}{dt}\right) C_{\mathrm{pp}}[T_{ij} - T_{\mathrm{p},ij}^{(l,k)}]dt \tag{3.33}$$

$$S_{\mathrm{p},ij}^{E} = \sum_l \sum_k N_{ij}^{(l,k)}[Q_{\mathrm{p},ij}^{(l,k)} + Q_{\mathrm{v},ij}^{(l,k)}] \tag{3.34}$$

3.3.7 Thermodynamic properties of Ar/O_2 mixture and Ti vapor

The calculation needs thermodynamic properties of Ti solid feedstock, Ar/O_2 mixture and Ti vapor in gas phase. The thermodynamic properties of Ti solid feedstock used in the calculation is summarized in Table 3.1. For this purpose, the equilibrium composition of Ar-O_2 mixture was first calculated by minimization of Gibbs' free energy of a system of A-O-Ti. Figure 3.3 presents the molar fraction of Ar-O_2 thermal plasma without Ti vapor at a pressure of 300 torr as a function of temperature. As seen, oxygen molecule O_2 is dissociated at temperatures around 3000 K to produce O atoms. A further increase in the temperature from 8000 K involves the ionization of Ar and O atoms, resulting in increased mole fraction of electrons and ions. Electrons are almost supplied from ionization of Ar atoms. On the other hand, Fig. 3.4 depicts the equilibrium composition of 89%Ar+9%O_2+9%Ti thermal plasma at the same pressure. At temperatures from 3000 K the electrons are supplied from ionization of Ti atom because metal vapor of Ti (6.82 eV) has lower ionization potential than Ar (15.76 eV) and O (13.61 eV). Another noticeable point is that the equilibrium composition has high mole fractions of TiO_2 and TiO in gas phase at temperatures below 4000 K. Especially, TiO is second dominant species at temperatures below 3000 K in this condition. It should be noted that TiO is one of precursors for nucleation of TiO_2 nanoparticles.

Using the calculated equilibrium composition, we computed the thermodynamic and transport properties such as the mass density, the enthalpy, the specific heat, the electrical conductivity, thermal conductivity and viscosity. In calculation of the transport properties, the first order approximation of Chapman-Enskog method was adopted [19] [20] [30] [31].

Figure 3.5 indicates specific heat at constant pressure of Ar-O_2 and Ti vapor at 300 torr. The Ti admixture ratio to 90%Ar/10%O_2 is taken as a parameter. Specific heat has peculiar peak at specified temperatures. The peak in specific heat at 25000 K corresponds to the power consumption for ionization of Ar^+ and O^+, and the peak at 14000 K is due to ionization of Ar and O atoms. Specific heat at higher admixture ratio of Ti vapor has a peak 6000 K. This arises from Ti ionization. On the other hand, the peak at 4000 K is attributed to the dissociation of TiO. The calculated electrical conductivity of Ar-O-Ti mixtures is plotted in Fig. 3.6. As seen in this figure, the electrical conductivity rises up rapidly at temperatures around 5000 K for 90%Ar/10%O_2 mixture. Addition of Ti

remarkably elevates the electrical conductivity in low temperature region below 5000 K. For example, only 1%Ti inclusion increase the electrical conductivity from 10 S/m to 1000 S/m at 6000 K. This is due to the ionization of metal vapor of Ti. Viscosity of Ar-O-Ti vapor can be seen in Fig. 3.7. The viscosity increases with temperature from 300 K to 10000 K, and then it decreases with temperature from 10000 K to 15000 K. This decrease in viscosity is due to large collision integrals between ion and electrons by Coulomb collision. An increase in Ti admixture ratio decreases the viscosity around 8000 K to 12000 K, which also results from Ti ionization at lower temperature.

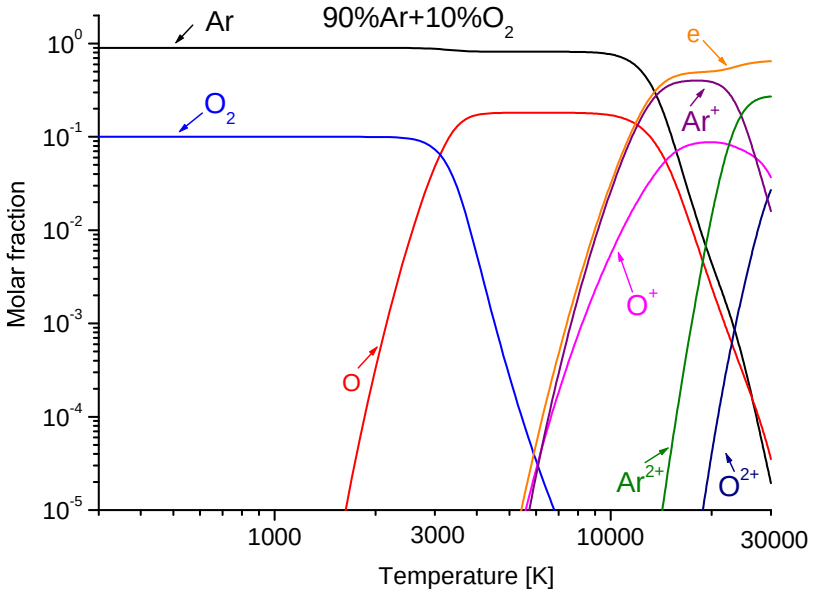

Fig. 3.3: Molar fraction of thermal plasma in 90%Ar+10%O_2 at a pressure of 300 Torr.

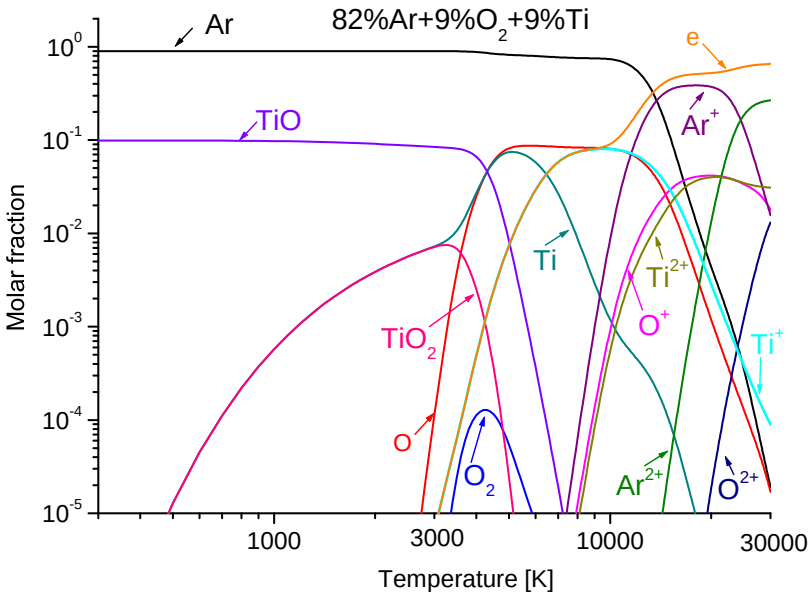

Fig. 3.4: Molar fraction of thermal plasma in 89%Ar+9%O_2 +9%Ti at a pressure of 300 Torr.

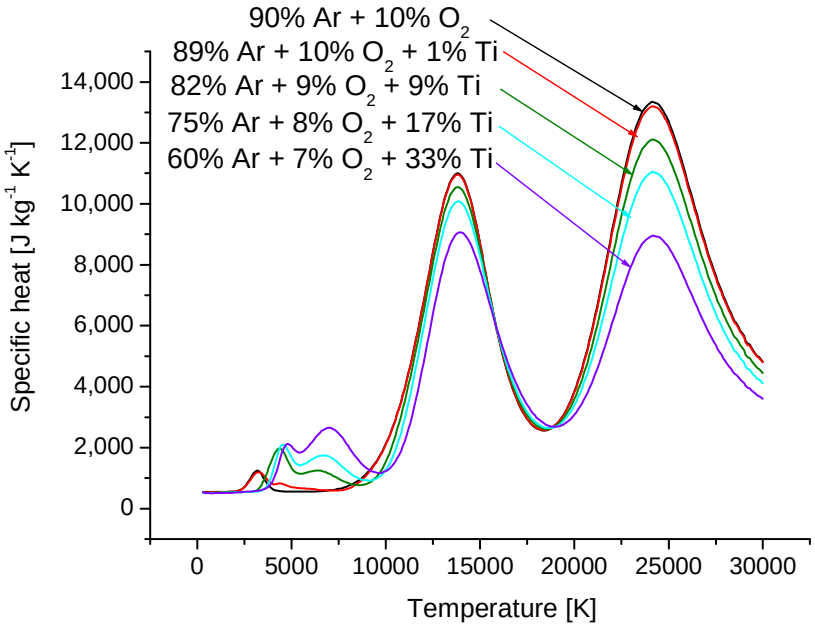

Fig. 3.5: Specific heat at constant pressure for Ar-O_2 thermal plasma with Ti vapor at a pressure of 300 Torr.

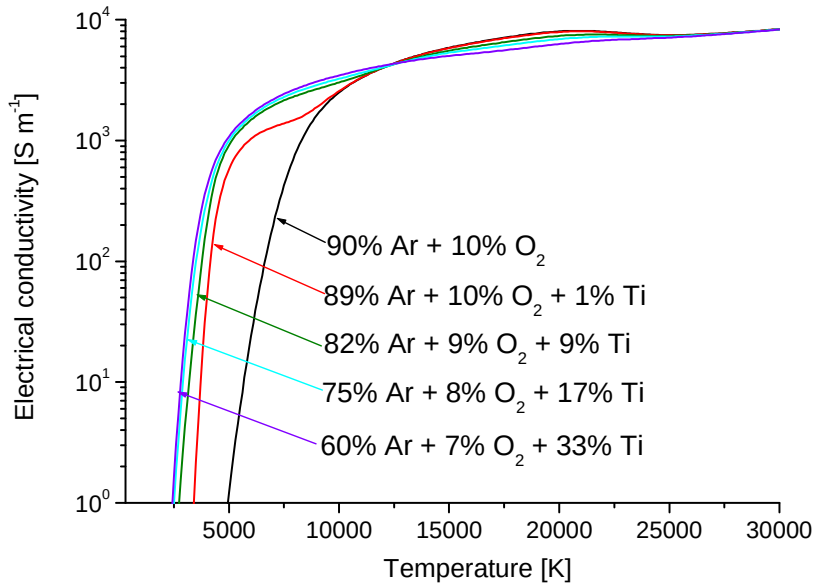

Fig. 3.6: Electrical conductivity for Ar-O_2 thermal plasma with Ti vapor at a pressure of 300 Torr.

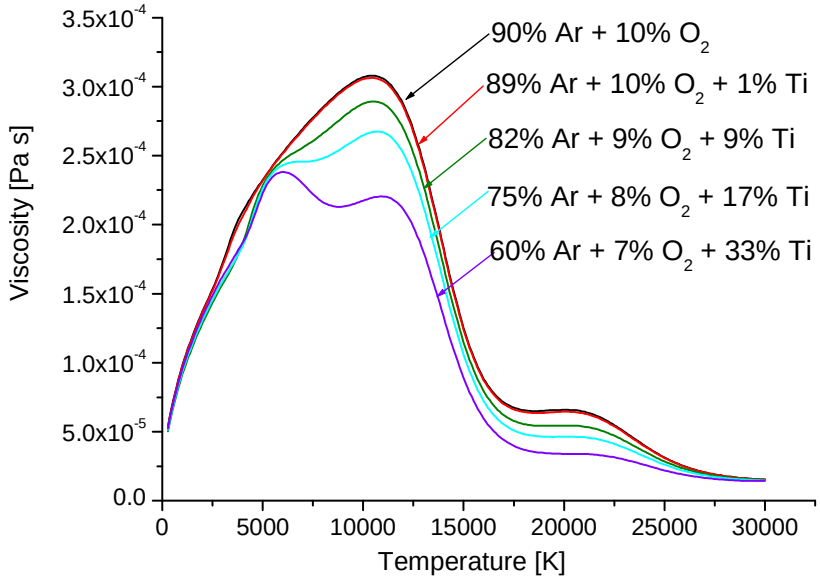

Fig. 3.7: Viscosity for Ar-O_2 thermal plasma with Ti vapor at a pressure of 300 Torr.

3.3.8 Calculation condition

The thermal plasma temperature field is much influenced by many physical parameters such as input power, sheath gas flow rate and also Ti powder feeding rate. Here, we researched influences of these physical parameters on the thermal plasma temperature field and gas flow field. Furthermore, influence of these parameters on the particle evaporation were also studied.

Table 3.2 summarizes the numerical calculation conditions in the present work. Four conditions were treated. As a standard reference condition, we set the input power of 20 kW, the frequency of the coil current of 450 kHz, the pressure of 300 torr, the sheath gas flow rate of 90 L/min, the Ar carrier gas flow rate of 4 L/min, and Ti powder feeding rate of 0.1 g/min. From the reference condition, only one condition was changed to study the influence of specified parameter on the thermal plasma temperature field. Condition (a) has a lower Ar-O_2 sheath gas flow rate of 70 L/min compared to the reference condition of 90 L/min. Condition (b) has a lower Ti feeding rate of 0.05 g/min compared to 0.1 g/min in the reference condition. The input power is also one of the important physical parameters to determine the thermal plasma temperature. The input power in condition (c) is lower at 10 kW from 20 kW of the reference condition. Conditions (a), (b) and (c) are all the conditions with reduced parameters to the reference condition.

Table 3.3 shows other conditions (d), (e) and (f). In condition (d), sheath gas flow rate of Ar-O_2 mixture was set to 110 L/min higher than the reference condition with 90 L/min. Condition (e) has higher Ti feeding rate of 0.5 g/min from the reference of 0.1 g/min. Finally, condition (f) has higher input power of 30 kW than that of 20 kW in reference condition.

Table 3.1: Thermodynamic properties of titanium powder

Mass density [kg/m^3]	4506
Melting temperature [K]	1953
Boiling temperature [K]	3535
Latent heat for melting [kJ/kg]	391
Latent heat for evaporation [kJ/kg]	8294
Specific heat of solid [J/(kg·K)]	528
Specific heat of liquid [J/(kg K)]	700
Thermal conductivity [W/(m·K)]	14
Emissivity of particle source (-)	0.4

Table 3.2: Calculation condition with lower value in parameters from reference.

Condition No.	Ref.Cond.	Cond.(a)	Cond.(b)	Cond.(c)
Input power [kW]	20	-	-	10
Frequency [kHz]	450	-	-	-
Pressure [Torr]	300	-	-	-
Sheath gas flow rate [L/min]	90	70	-	-
Carrier gas flow rate [L/min]	4	-	-	-
Feeding powder rate [g/min]	0.1	-	0.05	-

Table 3.3: Calculation condition with higher value in parameters from reference.

Condition No.	Ref.Cond.	Cond.(d)	Cond.(e)	Cond.(f)
Input power [kW]	20	-	-	30
Frequency [kHz]	450	-	-	-
Pressure [Torr]	300	-	-	-
Sheath gas flow rate [L/min]	90	110	-	-
Carrier gas flow rate [L/min]	4	-	-	-
Feeding powder rate [g/min]	0.1	-	0.5	-

3.4 Calculation results

3.4.1 Influence of operation parameters reduced to lower values

3.4.1.1 Temperature distribution and gas flow pattern

First of all, we mention the temperature distribution of the ICTP under the reference condition, as shown in Fig. 3.8(a). The ICTP has the wide high temperature region in the plasma torch by inductively coupling with electromagnetic field. The maximum temperature in the torch reaches to 12000 K around axial position of z=200 mm and radial position of r=17 mm. This means that the ICTP has high temperature region floating with a donut shape because the rf frequency eddy current flows in the ICTP itself by electromagnetic coupling. High temperature area with temperatures above 10000 K exists spreadly in region of $7.5 < r < 30$ mm and $130 < z < 298$ mm.

To consider influences of operation parameters, we compare the two-dimensional temperature distribution with a reduced parameters in (a) sheath gas flow rate, (b) feedstock feeding rate, and (c) input power from the reference condition as shown in Table 3.2 and Fig. 3.8. In addition, the radial distribution at z =250 mm and the axial distribution at r=5 mm are also depicted in Fig. 3.9 and Fig. 4.15, respectively, to indicate differences in the temperature value in each condition. As indicated in panel (a) in Fig. 3.8, the reduced sheath gas flow rate from 90 L/min to 70 L/min causes the shrinkage of the high temperature area with temperatures above 10000 K. This is attributable to the lower gas flow velocity in the ICTP in condition (a), weakening the axial convection flow transporting heat flux to downstream. Thus, the ICTP is totally shifted to be sustained to the upper side than that in the reference condition. In panel (b) in Fig.3.8, almost similar temperature distribution except around the axial axis r = 0 mm can be seen for condition (b) in which feedstock feeding rate is reduced from 0.1 g/min to 0.05 g/min. The temperature at r=0 mm increases from 7700 K to 8700 K around z=250 mm from the reference condition to condition (b) as indicated in Fig. 3.9. This result suggests that the change in feed rate in this range hardly affects the temperature distribution in the main ICTP region, but only the temperature on the axis where the feedstock is molten and evaporated with power consumption. On the other hand, condition (c) clearly decreases the temperature of main ICTP region as shown in Fig. 3.8(c) by reducing input power from 20 kW to 10 kW. Fig-

ure 4.15 also shows the lower temperature at r= 5 mm compared to the other conditions. This is reasonable because joule heating power to heat up the ICTP is reduced.

The gas flow pattern at each condition can be seen in Fig. 4.16. By reducing sheath gas flow rate from 90 L/min in panel of reference to 70 L/min in panel (a), the gas flow is bent in radial direction more strongly. This is because weakened axial gas flow velocity is obtained in lower sheath gas flow, and then Lorentz force acts to pinch the ICTP more. As a result, there is a vortex near the wall around z=220 mm. On the other hand, reduced feedstock feeding rate hardly changes the gas flow pattern as depicted in panel (b). However, reduced input power from 20 kW to 10 kW changes the gas flow pattern as shown in panel (c). This is due to the reduced Lorentz force from the reduced eddy current inside the ICTP, which weakens the radial gas flow.

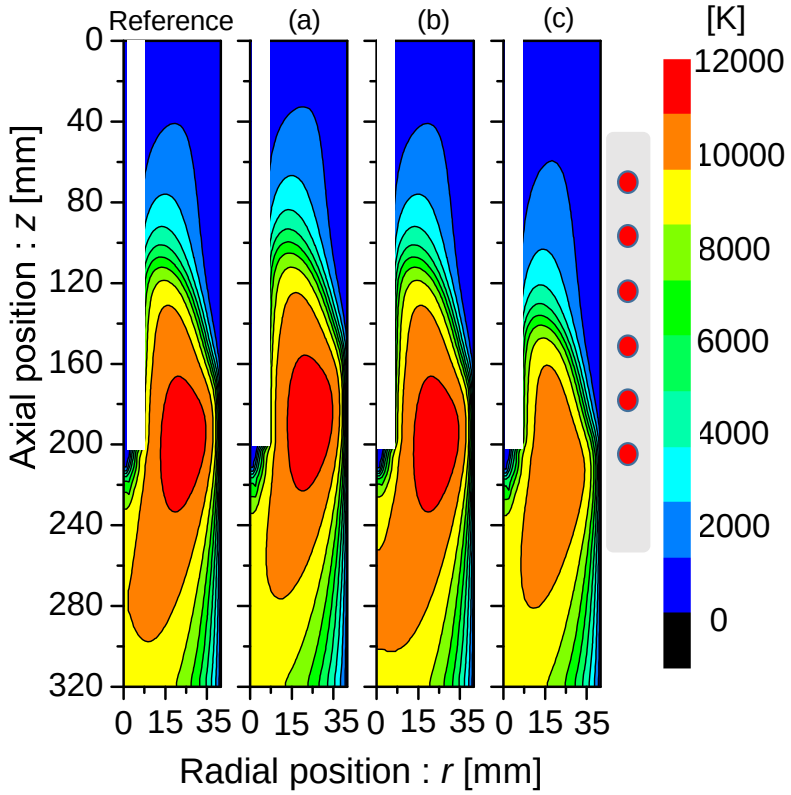

Fig. 3.8: Temperature distribution of Ar-O_2 thermal plasma with Ti powder injection for reduced sheath gas flow rate (a), feedstock feeding rate (b), input power (c) from the reference condition at a pressure of 300 Torr.

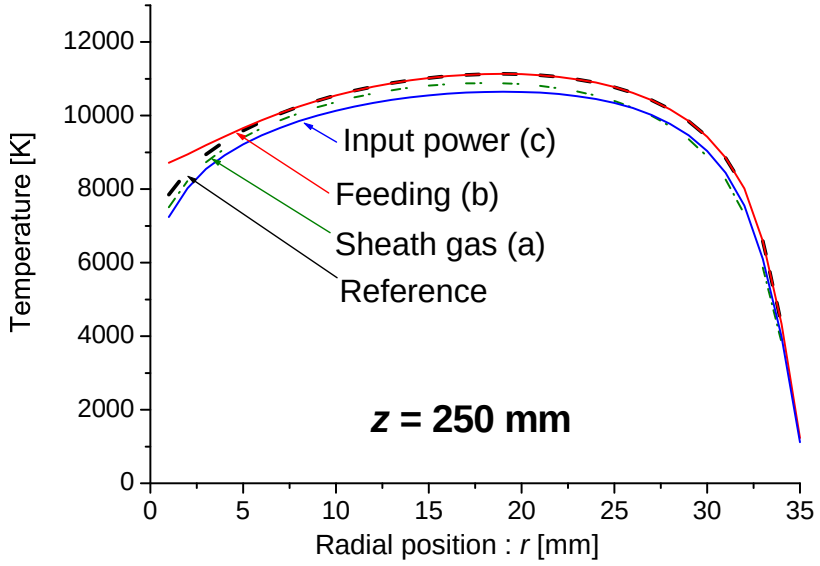

Fig. 3.9: Radial temperature distribution of Ar-O_2 thermal plasma with Ti powder injection at axial positions of 250 mm for reduced sheath gas flow rate (a), feedstock feeding rate (b), input power (c) from the reference condition.

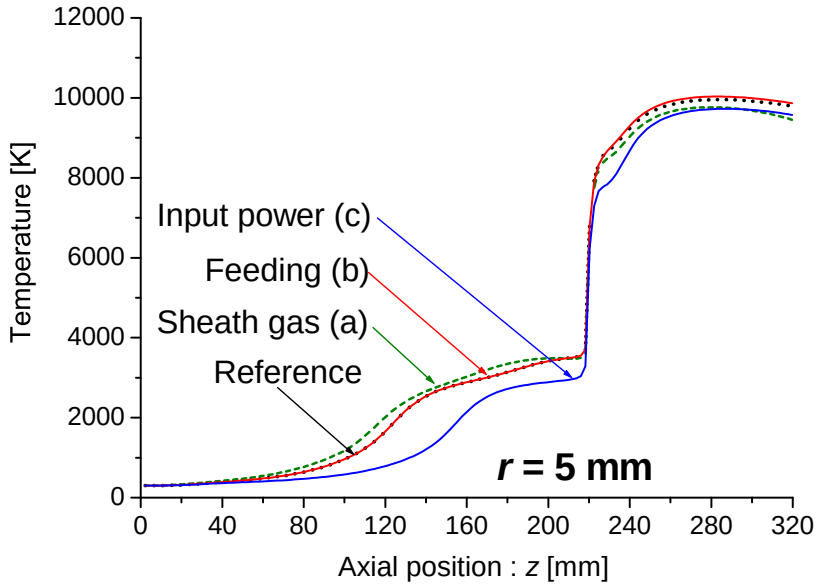

Fig. 3.10: Axial temperature distribution of Ar-O_2 thermal plasma with Ti powder injection at radial positions of 5 mm for reduced sheath gas flow rate (a), feedstock feeding rate (b), input power (c) from the reference condition.

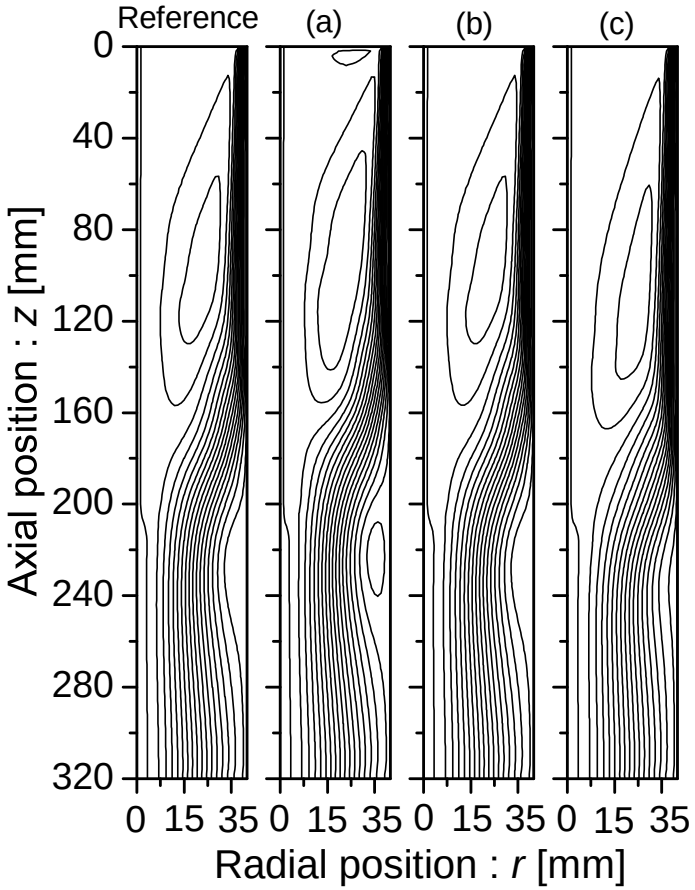

Fig. 3.11: Streamline in Ar-O_2 thermal plasma with Ti powder injection for reduced sheath gas flow rate (a), feedstock feeding rate (b), input power (c) from the reference condition at a pressure of 300 Torr.

3.4.1.2 Mass fraction distribution of Ti vapor

Operation parameters affect the temperature distribution and then the evaporation of Ti feedstock. Thus mass fraction of Ti vapor can also be influenced. Figure 4.17 shows the mass fraction of Ti vapor from evaporation of Ti feedstock powder. Titanium feedstock powder is injected from the tip of a water-cooled pipe around the axis from the top of the plasma torch. As seen in Fig.4.17, in the reference condition, the high mass fraction region of Ti vapor is distributed far from the tip of the water-cooled pipe at z=200 mm where Ti feedstock powder is supplied in Ar-O_2 ICTPs. At just below the tip of the pipe at $200 < z < 220$ mm, the temperature of the ICTP becomes low because of heat transfer to Ti feedstock particle as indicated in Fig. 3.8, and thus the Ti feedstock is hardly evaporated. At further downstream, Ti feedstock powder is evaporated to elevate the mass fraction of Ti vapor. In this way, the mass fraction of Ti vapor is present around the center axis from z >220 mm. The evaporation of Ti feedstock powder causes the contamination of Ti vapor inside the ICTP. The contaminated titanium vapor is transported by gas flow convection of Ar carrier gas and by diffusion. Thus, Ti vapor is present downstream of the feeding pipe.

Reducing sheath gas flow rate offers almost similar distribution of Ti mass fraction in Fig.4.17(a) compared to that in reference condition. Only a difference is downstream portion due to a vortex near the wall around z=220 mm as indicated in Fig. 4.16(a). Figure 4.17(b) is the result for reducing Ti feedstock powder feed rate. Actually, the mass fraction of Ti vapor is decreased because the amount of Ti feedstock is lower. In Fig.4.17(c), we have a similar mass fraction of Ti vapor distribution although the input power is clearly reduced from 20 kW to 10 kW but the mass fraction of Ti vapor is widely extended in radial direction. This arises from the fact that the temperatures just below the tip of the water-cooled pipe are around 8200 K and 7800 K at 20 kW and 10 kW, respectively, which are high enough to evaporate Ti feedstock.

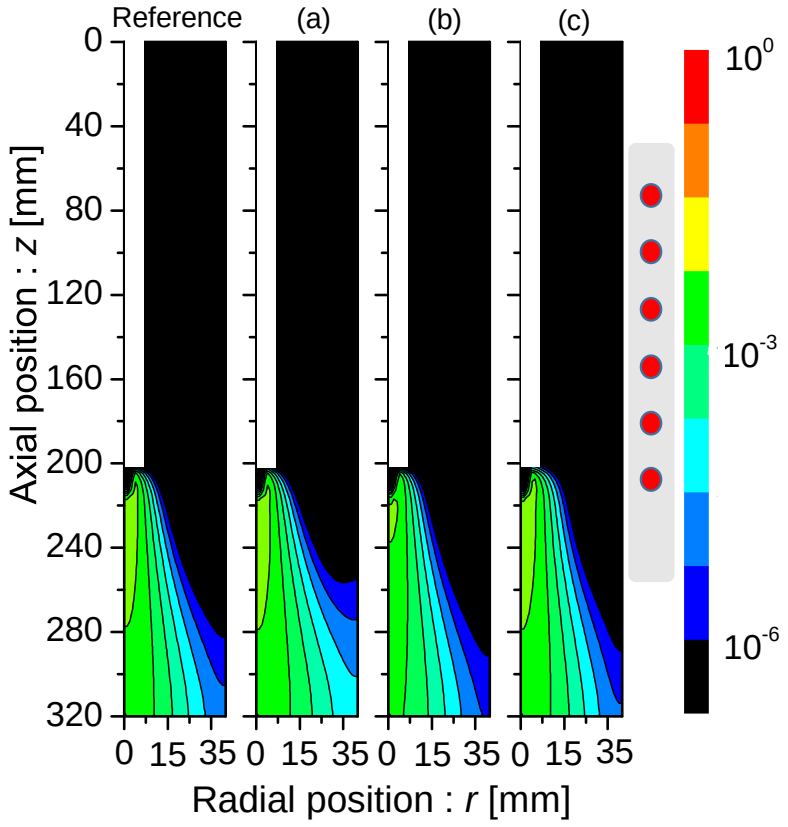

Fig. 3.12: Mass fraction distribution of Ti vapor in Ar-O_2 plasma with Ti powder injection for reduced sheath gas flow rate (a), feedstock feeding rate (b), input power (c) from the reference condition at a pressure of 300 Torr.

3.4.2 Influence of operation parameters increased to higher values

3.4.2.1 Temperature distribution and gas flow pattern

In this section, influence of operation parameters increased was studied on the temperature distribution in the ICTP torch. Figure 4.18 shows the temperature distribution of the ICTP for the reference condition and for increased sheath gas flow rate (d), Ti feedstock feeding rate (e), and input power (f), as shown in Table 3.3. In addition, the radial distribution at z =250 mm and the axial distribution at r=5 mm are also depicted in Fig. 4.19 and Fig. 4.20, respectively, to indicate differences in the temperature value in each condition.

Compared to the temperature distribution for the reference condition, increasing sheath gas flow rate provides axially longer distribution for temperature region with 10000 K. This is due to higher convective transport of high temperature region by high gas flow velocity at higher sheath gas flow rate of 110 L/min. On the other hand, large influence can be found for the temperature distribution on the axis when the Ti feedstock feed rate is increased from 0.1 g/min to 0.5 g/min. The axis temperature is effectively decreased by increasing Ti feedstock feed rate from 8000 K to 4700 K at z=250 mm, as indicated in Fig. 4.19. This originates from the power consumption for heavy load of Ti feedstock around the axis. It is noted that axis temperature from z=220 mm to z=320 mm becomes lower below 7000 K. This value is lower than those in the other condition treated here. If we increase the input power from 20 kW to 30 kW, high temperature area can be seen widely in the plasma torch as shown in Fig. 4.18. However, the temperature on the axis is hardly elevated from 8000 K. This is because the ICTP is heated by joule heating due to the eddy current on the off-axis region in the ICTP, but the ICTP on the axis is not directly heated. Therefore, the increased input power increases the temperature and high temperature region in the torch, but it hardly increases the temperature on the axis.

The gas flow pattern can be seen in Fig. 4.21 for increased operation parameters. As seen in panel (d), increasing sheath gas flow rate shrinks the vortex in the upper side of the plasma torch, resulting from the stronger axial gas flow. On the other hand, the higher feeding rate of Ti feedstock hardly affects the gas flow pattern in panel (e). Finally, higher

input power causes strong bend of the gas flow around z=160 mm due to Lorentz force, which results in the appearance of another vortex near the torch wall around z=230 mm.

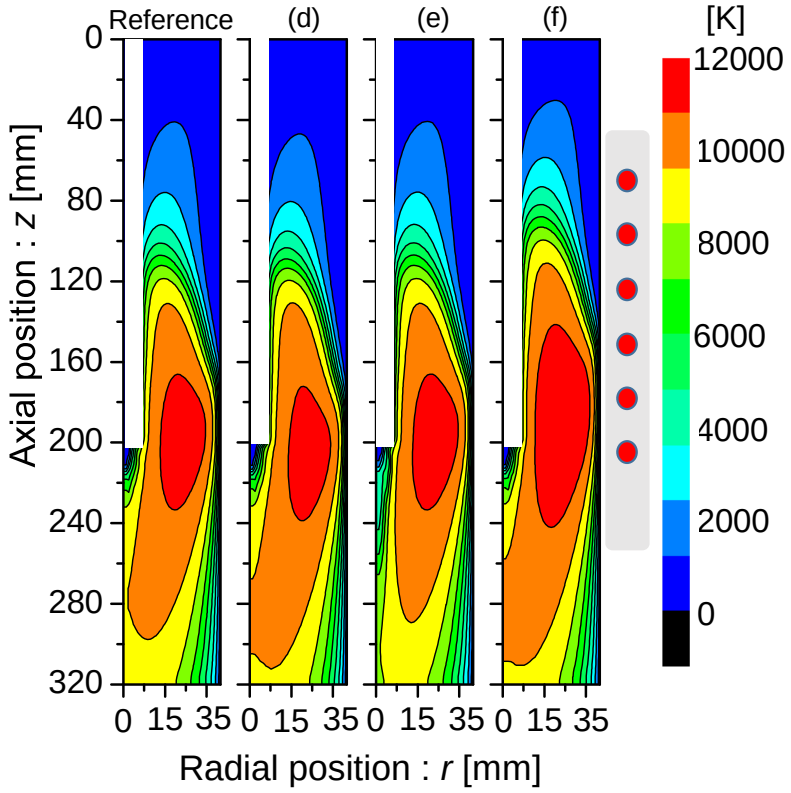

Fig. 3.13: Temperature distribution in Ar-O_2 thermal plasma with Ti powder injection for increased sheath gas flow rate (d), feedstock feeding rate (e), input power (f) from the reference condition at a pressure of 300 Torr.

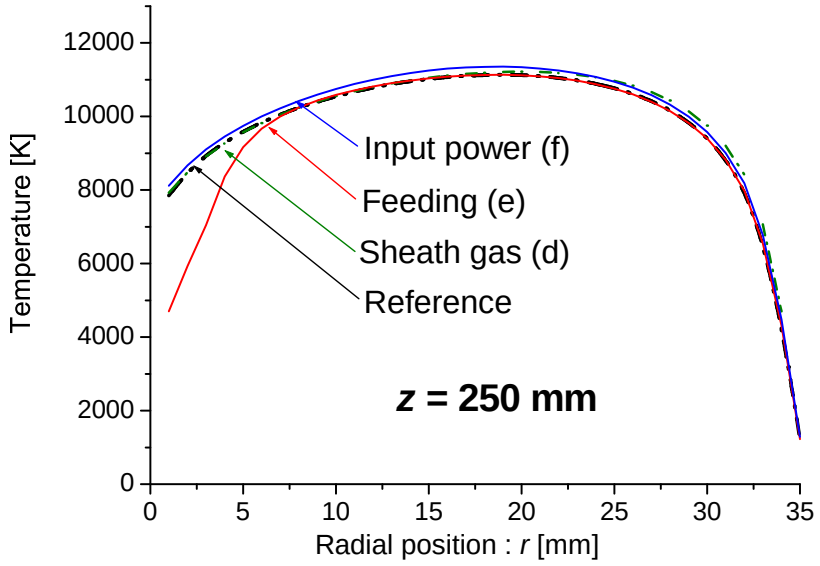

Fig. 3.14: Radial temperature distribution of Ar-O_2 thermal plasma with Ti powder injection for increased sheath gas flow rate (d), feedstock feeding rate (e), input power (f) at axial positions of 250 mm.

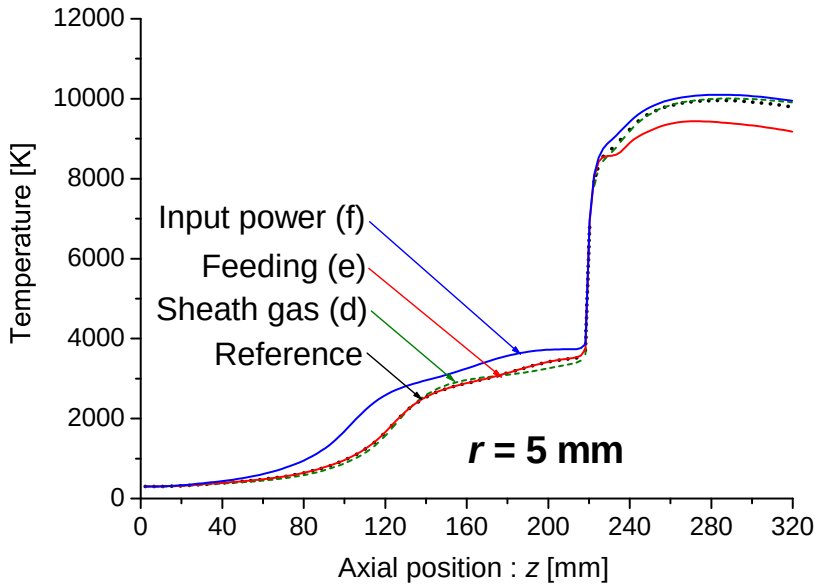

Fig. 3.15: Axial temperature distribution of Ar-O_2 thermal plasma with Ti powder injection for increased sheath gas flow rate (d), feedstock feeding rate (e), input power (f) at radial positions of 5 mm.

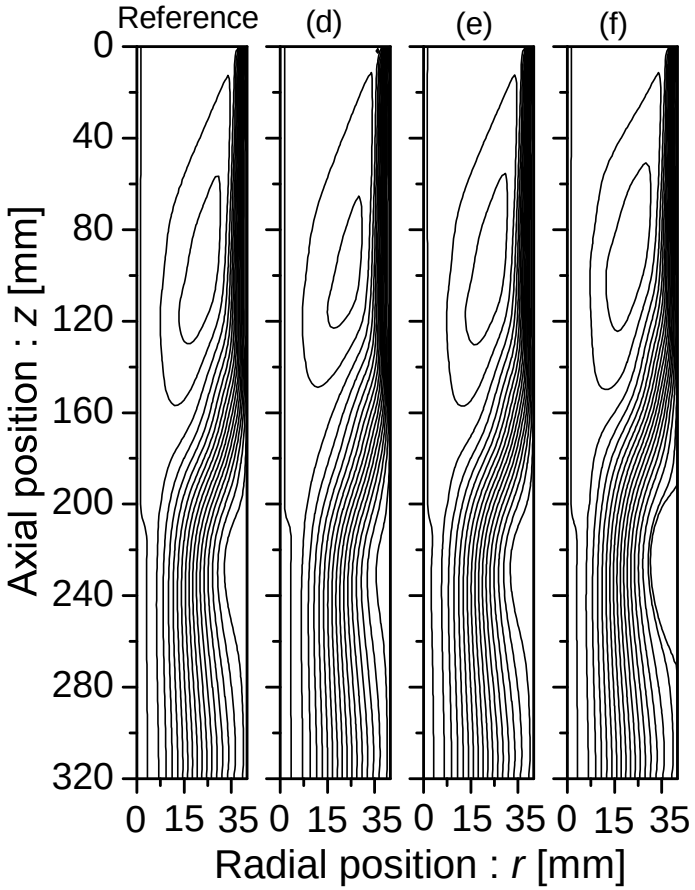

Fig. 3.16: Streamline in Ar-O_2 thermal plasma with Ti powder injection for increased sheath gas flow rate (d), feedstock feeding rate (e), input power (f) from the reference condition at a pressure of 300 Torr.

3.4.2.2 Mass fraction distribution of Ti vapor

The evaporation amount of Ti feedstock and then mass fraction of Ti vapor in gas phase are also influenced by operation parameters. Figure 4.22 presents the mass fraction distribution of Ti vapor using the reference condition and increased operating parameters. As seen in this figure, increased sheath gas flow rate gives insignificant change in the mass fraction of Ti vapor. This implies that sheath gas flow rate shows almost no influence on the evaporation of Ti feedstock. Figure 4.22(e) shows the mass fraction of Ti vapor for increased feed rate of Ti feedstock to 0.5 g/min. If the feed rate of Ti feedstock increases, the mass fraction is increased as shown. This suggests that evaporation amount of Ti feedstock can be enhanced by increasing feed rate to 0.5 g/min. On the other hand, the input power increased to 30 kW hardly affects the mass fraction of Ti vapor, implying the evaporation amount cannot be elevated significantly only by increasing input power.

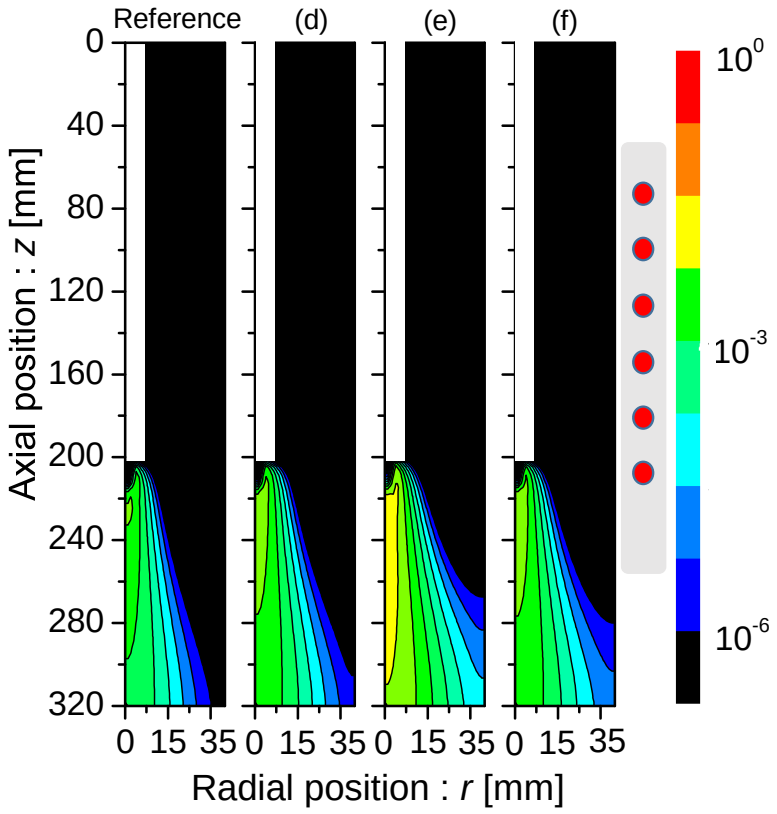

Fig. 3.17: Mass concentration distribution of Ti vapor in Ar-O_2 thermal plasma with Ti powder injection for increased sheath gas flow rate (d), feedstock feeding rate (e), input power (f) from the reference condition at a pressure of 300 Torr.

3.4.3 Particle behavior

In this calculation, Ti feedstock particles are injected into the ICTP, and they are heated, molten and evaporated through their flight. In evaporation process, the diameter of the particle decreases with time. This can be found in Fig. 4.23 under the reference condition. In this figure, behaviour of particles at different initial positions were distinguished by different colors: particle behavior at a radial initial position of r =0.3 mm is denoted by black curves, r=0.6 mm by red curves, r=0.9 mm by blue curves, r=1.2 mm by pink curves, and r=1.5 mm by green curves, respectively. Also, feedstock powder was assumed to consist of particles with seven discrete diameters, as presented in the lower panel in Fig. 2. Thus, Fig. 4.23 has variations in diameters of these 35 particles as a function of axial position. There are 35 time variations in particle size change for 7 different diameters and 5 different initial positions. This calculation of 35 trajectories was done for statistical calculation on the particle size change and its influence on the thermal plasma temperature. Therefore, we do not mention each of particle size change but general change in particle size. From axial position from 0 to 210 mm in Fig. 4.23, the diameters of particles do not change because all the particles are present inside the water-cooled pipe. From axial position of 210 mm, the particles start flying into the ICTP, and then they are heated by the ICTP. After some flight to be heated, the Ti particles have the diameter decreased. This is because of evaporation of the Ti particles from the ICTP. In this case, the particles are strongly heated from the ICTP, and then the particle diameter decreases to 0.25 μm. This evaporation generates Ti vapor to the ICTP. The important point in this figure is that all the particles have diameters decreased until z=228 mm. This implies that all the particles at 7 different initial position with 5 different initial diameter are completely evaporated.

Detailed temperature variation at each shell inside one particle are presented in Fig. 4.24. This is the temperature history for 3 shells inside one Ti particle with initial diameter of 4 . The outer shell of the Ti particle increases rapidly after particle ejection to the high-temperature plasma region from the axial position z = 200 mm. When the temperature reaches the melting temperature of the titanium materials, i.e. 1953 K, melting occurs. In this case, the particle's outer shell maintains a constant temperature of 1953 K. Simultaneously, the liquid phase fraction in the shell is increased during melting. During these processes, the heat is transported from the outer side to the inner side of the particle by

thermal conduction to increase the inside temperature of the particle. After the liquid fraction of each shell reaches to unity, the temperature of the shell is again increased. Then the temperature rapidly reaches to the evaporation/boiling temperature of 3535 K. The particle moves to position at $z = 225$ mm when this evaporation process occurs. After that, the particle continue to be evaporated during its flight. In this way, the injected particle has been heated by the ICTP rapidly, resulting in its complete evaporation. This evaporated material contaminates the ICTP to increase the mass fraction of Ti vapor as indicated in Fig.4.22.

Figure 4.25 shows the time variation in particle diameters of 35 Ti particles injected with 0.5 g/min feeding rate. The different colors in Fig.4.25 indicate different initial positions of the particles injected. As seen in this figure, the particle diameters decrease from axial position of 210-220 mm because of Ti evaporation. This evaporation provides Ti vapor in gas phase in the ICTP. However, the particle diameter decreases from the initial value more slowly than those in reference condition. This means that vapor are provided continuously from 210-255 mm from Ti evaporation. This arises from the fact that increasing feeding rate can decay the temperature on the torch axis as shown in the previous section.

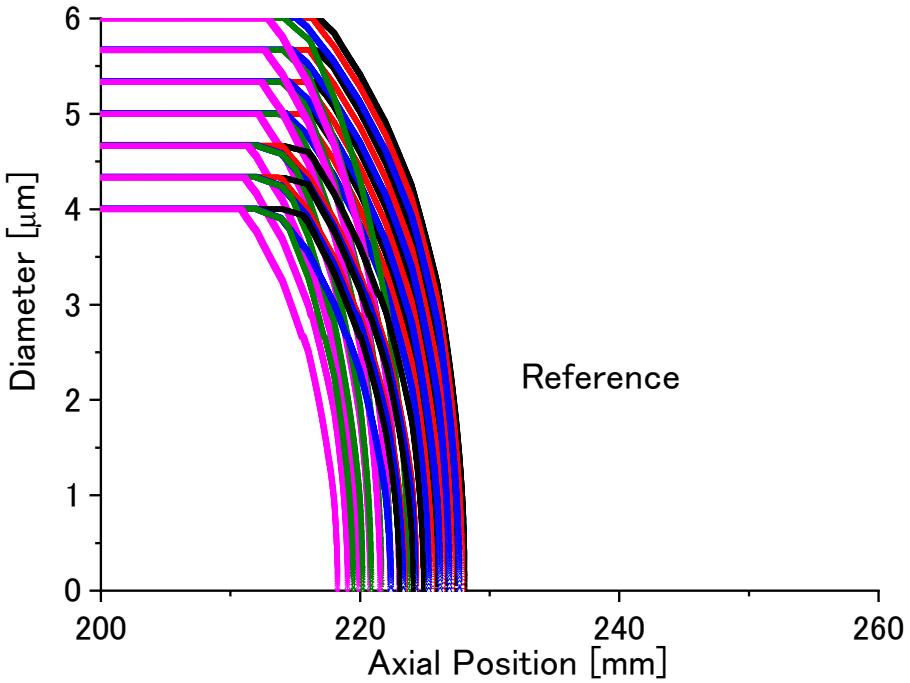

Fig. 3.18: Time variation in particle diameters of 35 Ti particles injected into Ar-O_2 ICTP for the reference condition. Particles have initial 5 different diameters. The different curves with the same initial diameter indicates the results of particle diameters injected at different initial 7 radial positions as indicated in Fig. 3.2.

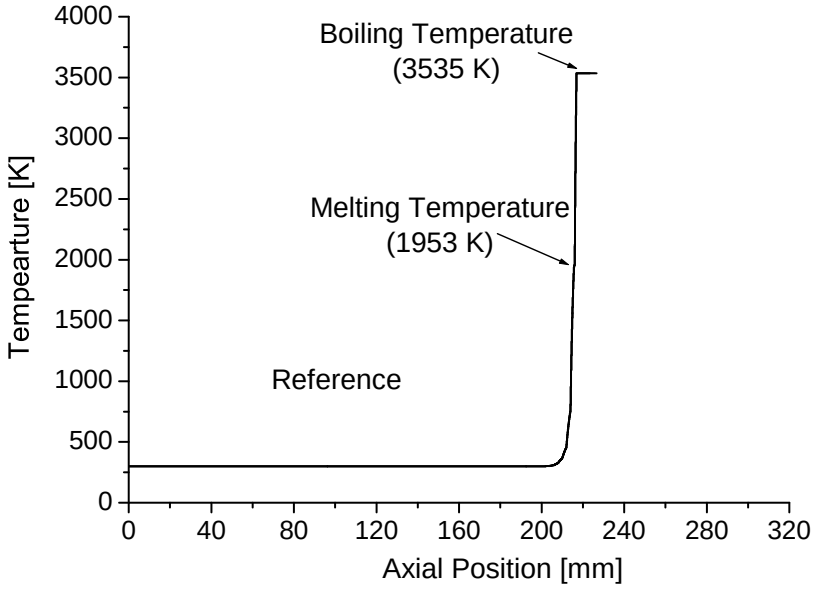

Fig. 3.19: An example of particle temperature history flying of a single Ti particle in Ar-O_2 ICTP under the reference condition. Temperatures for 3 shells in a single particle are indicated here.

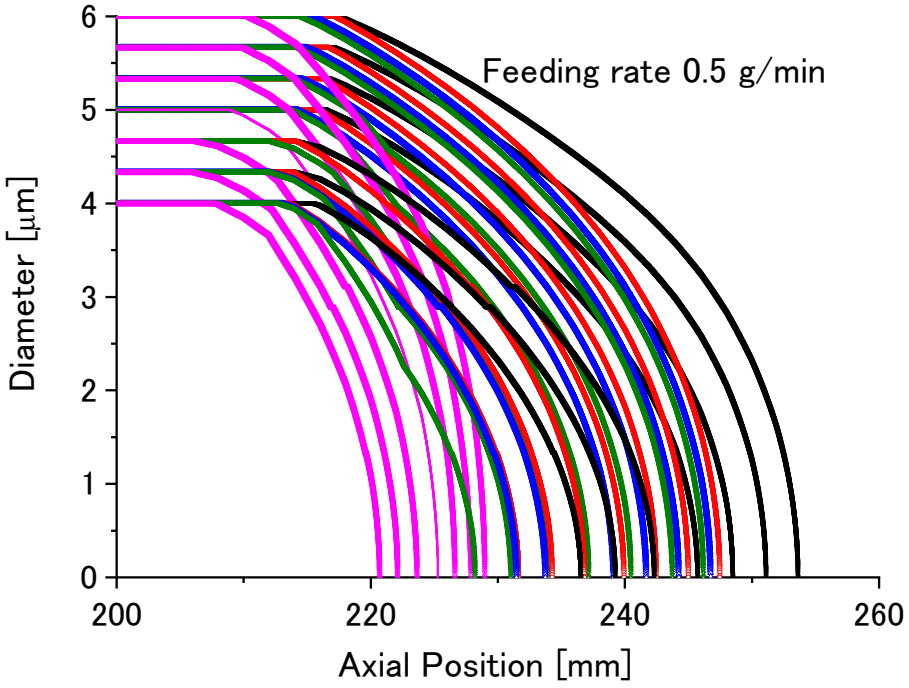

Fig. 3.20: Time variation in particle diameters of 35 Ti particles injected into Ar-O_2 ICTP with 0.5 g/min feeding rate. Particles have initial 5 different diameters. The different curves with the same initial diameter indicates the results of particle diameters injected at different initial 7 radial positions as indicated in Fig. 3.2.

3.5 Summary of chapter 3

A numerical simulation modelling was made for Ar/O_2 inductively coupled thermal plasma (ICTP) with Ti powder injection. This Ar/O_2 ICTP with Ti powder is used for TiO_2 nanoparticle synthesis. Inclusion of O_2 in Ar ICTP elevates the enthalpy, which may increase the evaporation of Ti powder. The model solves mass, momentum, and energy conservation equations with source terms from the evaporated material injected as a feedstock powder. The electromagnetic field is also obtained by solving Poisson equation for vector potential. Using this model, the influence of sheath gas flow rate, Ti powder feed rate, and input power were investigated on the temperature distribution of the ICTP and the mass fraction of Ti vapor and thus the amount of Ti feedstock evaporation. As a result, the temperature distribution can be affected by these operation parameters. Increasing sheath gas flow rate can changes the gas flow velocity and then convective transport of hot region. On the other hand, the feedstock can influence the temperature only on the axis through the evaporation of Ti feedstock and the affected temperature area is small. The input power can change the value and distribution of the temperature in the ICTP but the evaporation amount of Ti feedstock is hardly affected. This is because the ICTP is heated by eddy current on off-axis region. These calculation can provide fundamental data to understand the ICTP field with powder feeding.

References

[1] S. Gottlieb, N. Whrl, S. Schulz, V. Buck : "Simultaneous synthesis of nanodiamonds and graphene via plasma enhanced chemical vapor deposition (MW PE-CVD) on copper" *SpringerPlus* **5:568** pp.1-16 (2016)

[2] K.S. Kim, A. Moradian, J. Mostaghimi, G. Soucy : " Modeling of induction plasma process for fullerene synthesis: Effect of plasma gas composition and operating pressure" *Plasma Chemistry and Plasma Processing* **30** pp. 91-110 (2010)

[3] J. Mao, M. Liu, C.G. Deng, C.M. Deng, K.S. Zhou, Z.Q. Deng : "Preparation and distribution analysis of thermal barrier coatings deposited on multiple vanes by plasma spray-physical vapor deposition technology" *Journal of Engineering Materials and Technology, Transactions of the ASME* **139** (2017)

[4] Y. Tanaka and T. Sakuta : "Investigation of plasma-quenching efficiency of various gases using induction thermal plasma technique: effect of various gas injection on Ar thermal ICP" *Journal of Physics D: Applied Physics* **35** pp. 2149-2158 (2002)

[5] A. Mahmood, S.M. Ramay, Y.S. Al-Zaghayer, S. Atiq, I. Ahmad, M.A. Shar, S.D. Khan : "Study the structure and performance of thermal/plasma modified Au nanoparticle-doped TiO_2 photocatalyst" *Modern Physics Letters B* **28** pp.1450208-1 - 1450208-12 (2014)

[6] P.B. Kuyyadi, K.J. Mahaveer : "Effect of crystallization on humidity sensing properties of sol-gel derived nanocrystalline TiO_2 thin films" *Elsevier* **516** pp. 2175-2180 (2008)

[7] P.-J. Chu, S.-Y. Wu, K.-C. Chen, J.-L. He, A. Yerokhin, A. Matthews : "Nanostructured TiO_2 films by plasma electrolytic oxidation combined with chemical and thermal post-treatments of titanium, for dye-sensitized solar cell applications" *Thin Solid Films* **519** pp. 1723-1728 (2010)

[8] E. Pfender and Y.C.Lee : "Particle dynamics and particle heat and mass transfer in thermal plasma, Part I: The motion of a sigle particle without thermal effects", *Plasma Chem. Plasma Process.* **5** pp. 211-237 (1985)

[9] Y. C. Lee, Y. P. Chyou and E. Pfender: "Particle dynamics and particle heat and mass transfer in thermal plasmas, Part II: Particle heat and mass transfer in thermal plasmas", *Plasma Chem. Plasma Process.* **5** pp. 391-414 (1985)

[10] Y. P. Chyou and E. Pfender : "Behavior of particulates in thermal plasma flows", *Plasma Chem. Plasma Process.*, **9**, pp. 45–71 (1989)

[11] C.T. Crowe, M.P. Sharma and D.E. Stock : "The particle source in cell (PSI-Cell) model for gas droplet flows" *J. Fluids Eng.* **99** pp. 325-332 (1977)

[12] P. Proulx, J. Mostaghimi and M.I. Boulos : "Plasma particle interaction effects in induction plasma modeling" under dense loading conditions *Int. J. Heat Mass Transfer* **28** pp. 1327-1336 (1985)

[13] P. Proulx, J. Mostaghimi and M.I. Boulos : "Heating of powder in an r.f. inductively coupled plasma under dense loading conditions" *Plasma Chem. Plasma Process.* **7** pp. 29-52 (1987)

[14] M.I. Boulos, P. Fauchais and E. Pfender : "Thermal Plasma Fundamentals and Applications" vol. 1 *Plenum Press* pp. 366-369 (1994)

[15] C. Wang, Y. Tanaka and T. Sakuta : "Modeling of Ar Induction Thermal Plasma with an Injection of PTFE Powder" *Trans. IEEJ* **124-PE** pp. 440-446 (2004)

[16] Y. Takeuchi, Y. Tanaka, Y. Uesugi, S. Kaneko and S. Okabe : "Numerical simulation of thermal interaction between polymer and Ar induction thermal plasma" *Trans. IEEJ* **127-PE** pp. 739-746 (2007)

[17] Y. Tanaka, Y. Takeuchi, T. Sakuyama, Y.Uesugi, S. Kaneko, and S. Okabe : "Numerical and experimental investigations on thermal interaction between thermal plasma and solid polymer powders using induction thermal plasma techniquel" *J.Phys.D:Appl.Phys* **41** p. 025203 (2008)

[18] M.Y. Lee, J.S. Nam, I.M. Yang, and J.H Seo : "Equivalent circuit and numerical analyses of an inductively coupled plasma torch with a tapped induction coil" *AIP Advances* **8** pp. 115208 (2018)

[19] R.S. Devoto : "Transport coefficients of partially ionized argon" *Phys. Fluid* **10** pp. 354-364 (1967)

[20] Y. Tanaka, K.C Paul and T. Sakuta : "Thermodynamic and transport properties of N_2/O_2 mixtures at different admixture ratios" *T. IEE of Japan*, **120-PE**, pp. 24-30 (2000)

[21] J.M. Yos : "Transport properties of nitrogen, hydrogen, oxygen and air to 30 000 K", AVCO Technical Memorandum RAD-TM-63-7 (1963)

[22] S. Chapman and T.G. Cowling : "The Mathematical Theory of Non-Uniform Gases Third Edition" *Cambridge University Press* (1970)

Chapter 4

Numerical study of temperature and gas flow fields in Ar-O_2 tandem-type inductively coupled thermal plasma with Ti feedstock powder injection

4.1 Introduction

Inductively coupled thermal plasma (ICTP) has been used widely for materials processing such as diamond film deposition [1,2], transparent conductive oxide deposition [3], thermal barrier spray coating [4,5], and surface modification [6]. The benefits of using ICTP in these materials processing are attributed to the fact that the ICTP has high gas temperature of around 10 000 K, high enthalpy, and high density of chemical active species. Furthermore, the ICTP can offer a clean thermal plasma field without contamination because it is an electrode-less discharge. In light of these benefits, ICTP has been adopted recently for nanomaterial syntheses for materials such as nanoparticle [7]– [12], nanotube [13, 14], and fullerene [15, 16]. During processing, the ICTP is usually established by a single coil located around the plasma torch. To this plasma torch, feedstock powder is injected to the high-temperature field, thereby causing its evaporation. The evaporated materials are subsequently cooled to achieve nucleation and thereafter to synthesize nanomaterials. During these processes, the ICTP sometimes becomes unstable because of disturbance from heavy-load injection of feedstock powder. In the worst case, the ICTP can be extinguished by an overly heavy-load injection of feedstock powder.

To resolve this persistent difficulty, a tandem-type inductively coupled thermal plasma (tandem ICTP) has been developed. The tandem ICTP is established in a dielectric cylindrical tube with two coils. Such a tandem ICTP was first developed by Uesugi [17] to inject feedstock powder along the plasma torch instead of a hybrid dc-rf plasma torch. The temperature distribution in a tandem ICTP was also studied numerically by some researchers [17]– [20]. We have also developed a large volume tandem double-frequency ICTP system with two coils (the upper coil and the lower coil) operated at 400 kHz and 350 kHz, respectively [21]. In this experiment, mutual interacting current among the upper coil to lower coil were suppressed using two resonant circuits for each of coils at different resonance frequencies from each other. We further developed a tandem double-frequency type of pulse-modulated induction thermal plasma (tandem-PMITP) system [21]. In this experiment, the tandem-MITP is sustained with two amplitude-modulated coil currents supplied by two power sources. This tandem-coil arrangement can provide a spatially and temporally modulated thermal plasma field that is useful for new materials processing. Nevertheless, few reports of the relevant literature describe studies of gas flow and temperature field in a tandem double-frequency coil ICTP with feedstock powder injection , although some steady state calculations were done for tandem double-frequency coil ICTP without feedstock powder feeding [20]. Powder injection is well known to affect the temperature field in the ICTP by powder evaporation. The materials evaporated into the thermal plasma can markedly change the thermodynamic and transport properties of the thermal plasma. This marked change in the properties can alter the temperature and the gas flow field in thermal plasmas.

As described in this paper, by updating our numerical model for single-frequency coil ICTP with powder injection [22]– [25], numerical simulation was conducted to obtain temperature and gas flow fields in a tandem double-frequency coil ICTP with powder injection. Tandem double-frequency coil ICTP in this paper is sustained with two separate coils (an upper coil and a lower coil) of equal diameter. The upper and lower coil currents in tandem double-frequency coil ICTP treated are supplied by two separate power sources with mutually different operating frequencies. The high-temperature region in the upper coil region is expected to be used for establishment of stable ICTP, whereas the feedstock powder is fed to the lower coil region of the ICTP to evaporate the feedstock powder. This tandem

double-frequency coil ICTP can be useful for nanoparticle synthesis, for example. The developed model for a tandem double-frequency coil ICTP with powder injection solves the mass, the momentum, and the energy conservation equations for thermal plasma involving thermal interactions with feedstock powder. The powder particle motion was obtained by solving the motion equation for individual particles. Influences of the coil turn numbers and the gap length between the two coils and were investigated for temperature and gas flow fields. Through this study, unique distributions were obtained for the temperature and the feedstock vapour concentration in a tandem double-frequency coil ICTP.

4.2 Configuration of Tandem-coil Induction Thermal Plasma Torch

Coil configurations of two kinds with different turn numbers were assessed for use in the tandem-coil in one plasma torch. Figures 4.1(a) and 4.1(b) portray the configuration of ICTP torch with an 8-turn coil and a 12-turn coil, respectively, for a tandem-coil plasma torch. The plasma torch is made of 320-mm-long quartz tubes with 64 mm inner diameter. The quartz tube wall is water-cooled by flowing water. These torches have two separate coils (tandem-coil) in one plasma torch: an upper coil and a lower coil. The coil pitch is 20 mm for each coil. The distance between the upper coil end and the lower coil top was taken as a parameter. For the study described herein, the gap length between upper coil end and the lower coil top were set to four distances for calculation: 20 mm, 30 mm, 40 mm, and 60 mm. The 20 mm gap length condition corresponds to just a 'single coil' only if the exactly the same currents flow in the two coils. For these coils, two main situations were considered: In one condition, the two separate coils in one plasma torch were connected in series with one power source at one operating frequency. In this case, electromagnetic fields of one frequency are created. In the other condition, two separate coils in one plasma torch were connected with two independent power sources at different frequencies. In this case, the electromagnetic fields have two frequency components. For this study, these two coils were assumed to be connected with two RF power supplies at different operating frequencies of 450 kHz and 300 kHz to provide rf coil currents. Actually, the different operating frequencies are useful to decouple electric circuits for each of the

coils in our experiments [21]. From the head of the plasma torch, a gas mixture of argon (Ar) and oxygen (O_2) is supplied as a sheath gas, which is provided along the inner quartz tube wall with a swirl to prevent the plasma from reaching the inner quartz tube. The electromagnetic field generated in the torch by the tandem double-frequency coil current can accelerate electrons inside the plasma torch to generate a plasma mainly by electron impact ionization. From the top of the torch, a water-cooled pipe for powder feeding is inserted along the centre axis to the 4–5 turns of the lower coil, as shown in figures 4.1(a) and 4.1(b). For TiO_2 nanoparticle synthesis, titanium (Ti) powder feedstock is injected from the top along the torch axis together with the Ar carrier gas through the water-cooled pipe.

As described herein, numerical simulation was conducted to simulate temperature and gas flow fields for the described tandem double-frequency coil ICTP above operated at two frequencies. In addition, for comparison, an ICTP by a so-called single-coil at one frequency and ICTPs by a single coil with a certain gap between the upper and lower side operated with the same frequency were numerically simulated. Figure 4.2 depicts the definition of (a) single-frequency coil and (b) tandem double-frequency coil. The single-frequency coil ICTP was treated as the one with one operating frequencies, even with a gap. The single-frequency coil is defined as the coil having the exactly the same coil current. By contrast, the tandem double-frequency coil ICTP has two separate coils at two operating frequencies.

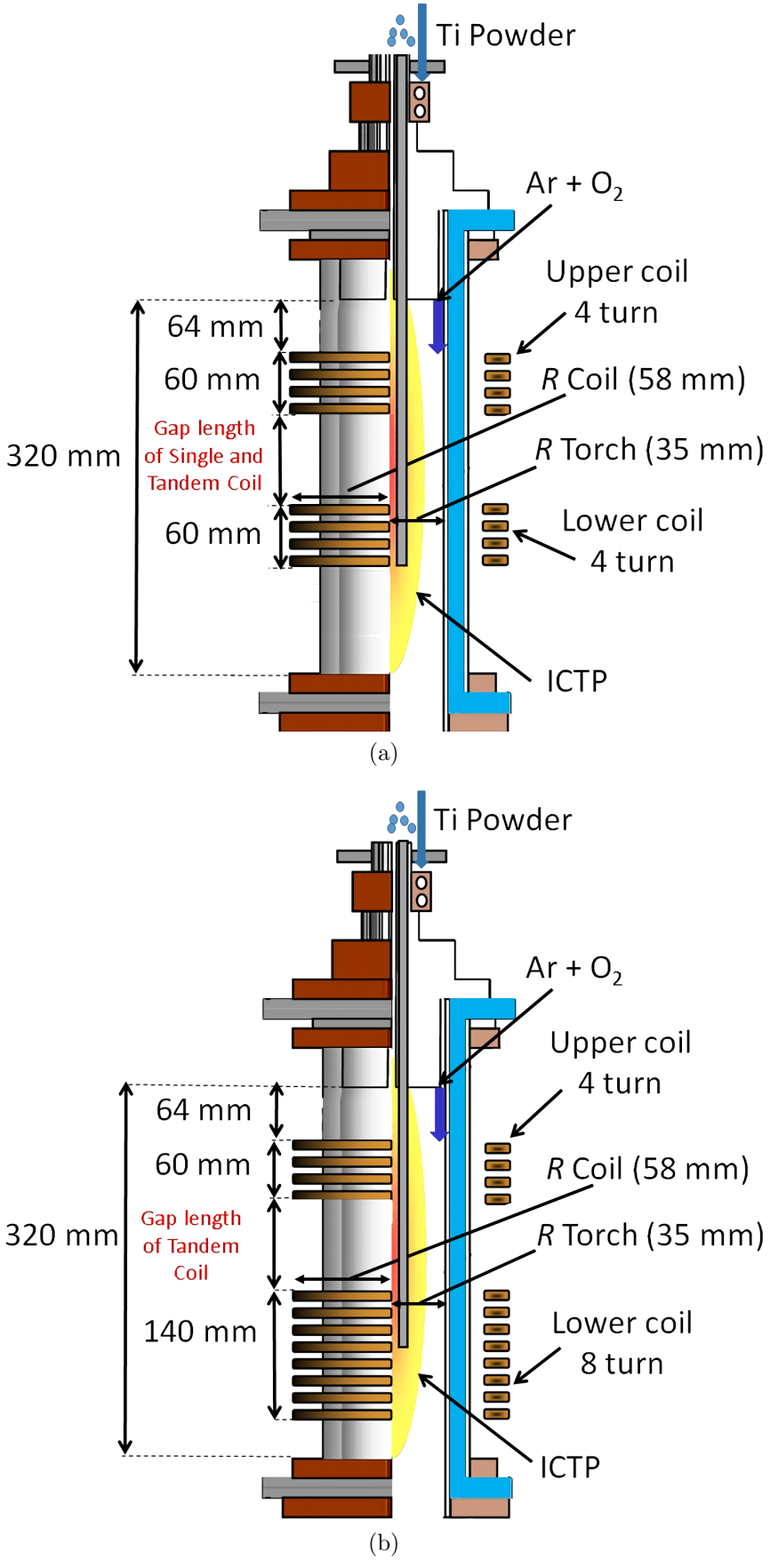

Fig. 4.1: Configuration ICTP torch with (a) 8-turn coil and (b) 12-turn coil.

4.3 Modelling of Tandem-coil Induction Thermal Plasma

4.3.1 Modelling assumptions

The developed tandem double-frequency coil ICTP model is based on the PSI-Cell fundamental reported by Crowe et al. [26]; the method of the PSI Cell were adopted to ICTP by Proulx and co-workers [27, 28]. The model includes the assumption that the following conditions apply for tandem-coil ICTP: (i) The tandem coil ICTP is in a local thermodynamic equilibrium (LTE) state. Consequently, all temperatures such as the excitation temperature, electron temperature, and heavy particle temperature are equal. In addition, chemical equilibrium conditions are established for all reactions. (ii) The condition of being optically thin is assumed for plasma at wavelengths greater than 200 nm. At wavelengths of less than 200 nm, the 20% of total emission coefficient is accounted to consider the effective light absorption for radiative transfer [29]. (iii) Laminar, axis-symmetric and steady flow are assumed with negligible viscous dissipation. (iv) Particle–particle interactions are not neglected for injected feedstock particles. (v) The feedstock particle radius is assumed to be much larger than the mean free path of plasma components. (vi) The feedstock particle always has spherical shape, even during evaporation. (vii) The feedstock particle surface is heated uniformly from the surrounding thermal plasmas. Therefore, evaporation also occurs uniformly around the particle surface. (viii) Influence of electronic charging on the particle is not considered. (ix) The rocket influence from ejected ablation vapour is not considered. (x) Injected titanium feedstock powders are evaporated solely by heat from the thermal plasma. Consequently, evaporation takes place uniformly around the particle surface. (xi) Mutual interacting current among the upper coil to lower coil are neglected because in the actual our experiment they were suppressed to below 10% of the main current, by using two resonant circuits for each of coils at different resonance frequencies from each other. Principle of superposition is simply adopted for electromagnetic fields at different frequencies from the upper coil and the lower coil.

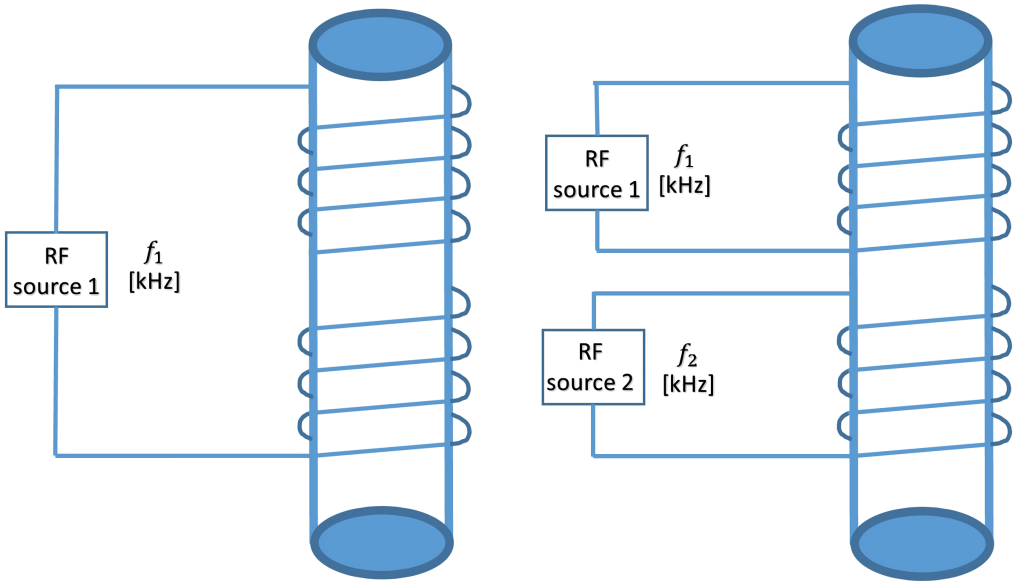

(a) (b)

Fig. 4.2: Definition of (a) Single-frequency coil and (b) Tandem double-frequency coil.

4.3.2 Governing equation for Ti feed powder

For an individual feedstock particle supplied through the water-cooled feeding pipe, the equation of motion was solved with Lagrangian form considering the drag force from the plasma fluid and gravity. In addition, the energy conservation equation of the individual particle was solved considering the heat conduction inside the particle, the heat flux from the plasma, and radiation loss from the particle surface. For consideration of melting and evaporation processes at the particle surface, the following equations were solved simultaneously as presented below.

$$\frac{du_\mathrm{p}}{dt} = -\frac{3}{4} C_\mathrm{D}(u_\mathrm{p} - u) U_\mathrm{R}\left(\frac{\rho}{\rho_\mathrm{p} d_\mathrm{p}}\right) + g \tag{4.1}$$

$$\frac{dv_\mathrm{p}}{dt} = -\frac{3}{4} C_\mathrm{D}(v_\mathrm{p} - v) U_\mathrm{R}\left(\frac{\rho}{\rho_\mathrm{p} d_\mathrm{p}}\right) \tag{4.2}$$

$$U_\mathrm{R} = \sqrt{(u_\mathrm{p} - u)^2 + (v_\mathrm{p} - v)^2}, \tag{4.3}$$

In those equations, the following variables were used: U_R represents the relative velocity between the plasma and Ti particle; C_D is the drag coefficient; ρ_p stands for the mass density of the Ti particle in solid and liquid phases; u_p denotes the axial velocity of the Ti

particle, v_{p} is the radial velocity of the particle; g represents the gravitational acceleration; and d_{p} expresses the Ti particle diameter. The directions of particles at the outlet of the powder feeding pipe were set as disorderly to three angle directions to simulate reflection of particles from the pipe wall.

Definitions of the diameter d_p, the temperature $T_{\mathrm{p}}(r,t)$ and liquid fraction $\chi(r,t)$ inside the titanium particle are presented in figure 4.3. As considered in this calculation, the individual particle was divided into several shells for discretization to simulate the temperature distribution inside the particle. For the individual particles, the following energy conservation equations (4.4)-(4.9) were solved.

To represent the titanium particle interior, equations (4.4) and (4.5) were solved for thermal conduction because of the radial gradient of the temperature in the inner shell.
-Inner shells ($0 < r \leq d_{\mathrm{p}-1}/2$):

$$\rho_{\mathrm{p}} C_{\mathrm{pp}} \frac{\partial T_{\mathrm{p}}(r,t)}{\partial t} = \frac{1}{r^2}\frac{\partial}{\partial r}(r^2 \lambda_{\mathrm{p}} \frac{\partial T_{\mathrm{p}}(r,t)}{\partial r}) \quad (T_{\mathrm{p}}(r,t) < T_{\mathrm{m}},\, T_{\mathrm{m}} < T_{\mathrm{p}}(r,t) < T_{\mathrm{b}}) \tag{4.4}$$

$$\rho_{\mathrm{p}} H_{\mathrm{m}} \frac{\partial \chi(r,t)}{\partial t} = \frac{1}{r^2}\frac{\partial}{\partial r}(r^2 \lambda_{\mathrm{p}} \frac{\partial T_{\mathrm{p}}(r,t)}{\partial r}) \quad (T_{\mathrm{p}}(r,t) = T_{\mathrm{m}}) \tag{4.5}$$

In those equations, the following variables were used: T_{m} signifies the Ti melting temperature; C_{pp} stands for the specific heat of the Ti particle in solid or liquid phase; T_{b} denotes the Ti boiling temperature; $T_{\mathrm{p}}(r,t)$ expresses the shell temperature inside the particle; λ_{p} represents the thermal conductivity of the Ti bulk; $\chi(r,t)$ is the liquid fraction of the shell, and H_{m} denotes the latent heat for melting. When temperature $T_{\mathrm{p}}(r,t)$ at a point inside the particle is less than the melting temperature T_{m}, the temperature can be changed corresponding to equation (4.4). However, when temperature $T_{\mathrm{p}}(r,t)$ reaches T_{m}, temperature $T_{\mathrm{p}}(r,t)$ is kept to the melting temperature, with change of the liquid fraction $\chi(r,t)$ according to equation (4.5).

For the outer shell, we assessed thermal conduction to the inside of the particle, heat transfer from the plasma, and the radiation transfer from the surface. In addition, evaporation was found to change the particle diameter as shown below.

-Outer shell ($d_{\mathrm{p}-1}/2 < r$):

$$\frac{1}{6}\pi(d_{\mathrm{p}}^3 - d_{\mathrm{p}-1}^3)\cdot\rho_{\mathrm{p}}C_{\mathrm{pp}}\frac{\partial T_{\mathrm{p}}(r_{\mathrm{out}},t)}{\partial t} = Q$$
$$(T_{\mathrm{p}}(r_{\mathrm{out}},t) < T_{\mathrm{m}},\, T_{\mathrm{m}} < T_{\mathrm{p}}(r_{\mathrm{out}},t) < T_{\mathrm{b}}) \tag{4.6}$$

$$\frac{1}{6}\pi(d_{\mathrm{p}}^3 - d_{\mathrm{p}-1}^3)\cdot\rho_{\mathrm{p}}H_{\mathrm{m}}\frac{\partial \chi(r_{\mathrm{out}},t)}{\partial t} = Q$$
$$(T_{\mathrm{p}}(r_{\mathrm{out}},t) = T_{\mathrm{m}}) \tag{4.7}$$

$$\frac{\pi d_{\mathrm{p}-1}^2}{2}\cdot\rho_{\mathrm{p}}H_{\mathrm{v}}\frac{\partial(d_{\mathrm{p}})}{\partial t} = Q \quad (T_{\mathrm{p}}(r_{\mathrm{out}},t) = T_{\mathrm{b}}) \tag{4.8}$$

$$\begin{aligned} Q &= -\pi d_{\mathrm{p}-1}^2\lambda_{\mathrm{p}}\left.\frac{\partial T_{\mathrm{p}}}{\partial r}\right|_{r=d_{\mathrm{p}-1}/2} \\ &+ \pi d_{\mathrm{p}}^2 h_c(T - T_{\mathrm{p}}(r_{\mathrm{out}},t)) \\ &- \pi d_{\mathrm{p}}^2\sigma_{\mathrm{s}}\epsilon(T_{\mathrm{p}}(r_{\mathrm{out}},t)^4 - T_{\mathrm{a}}^4) \end{aligned} \tag{4.9}$$

In those equations, the following variables were used: d_{p} represents the outer shell's inner diameter; H_{v} stands for the latent heat for evaporation; r_{out} denotes the radial position of the control volume of the outer shell, which is defined as $r_{\mathrm{out}} = \frac{1}{4}(d_{\mathrm{p}} + d_{\mathrm{p}-1})$; Q expresses heat at the outer shell from the thermal plasma; ϵ signifies the particle surface emissivity; T represents the thermal plasma temperature; σ_{s} is the Stefan–Boltzmann coefficient; T_{a} represents the ambient temperature; and h_{c} denotes the heat transfer coefficient between thermal plasma and titanium. The quantities C_{D} and h_{c} are given as a function of Reynolds number.

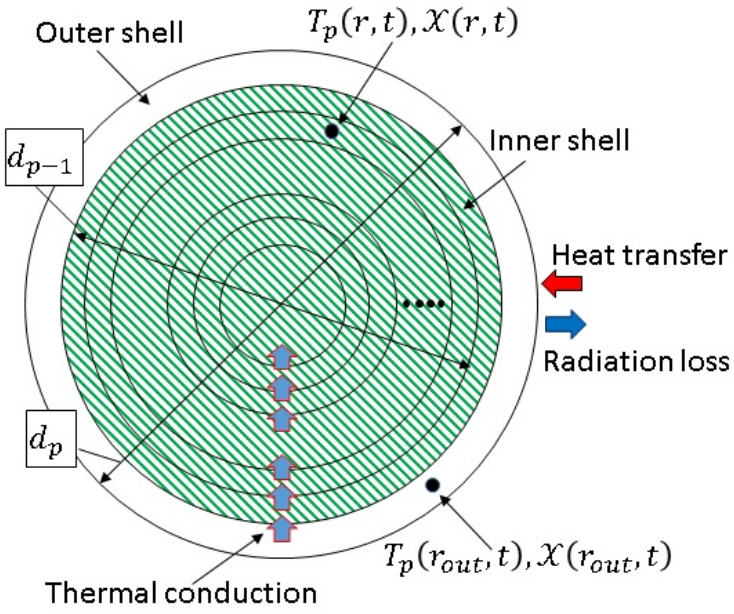

Fig. 4.3: Definition of parameters for temperature inside a titanium particle.

4.3.3 Governing equation for tandem-coil induction thermal plasma

Following the assumptions described in the previous section, the thermal plasma is considered to be governed by the following equations.

Mass conservation.

$$\frac{\partial(\rho u)}{\partial z} + \frac{1}{r}\frac{\partial(r\rho v)}{\partial r} = S_{\mathrm{p}}^{C} \tag{4.10}$$

Momentum conservation in the upper coil and lower coil.

Axial:

$$\begin{aligned} &\rho u\frac{\partial u}{\partial z} + \rho v\frac{\partial u}{\partial r} \\ &= -\frac{\partial p}{\partial z} + 2\frac{\partial}{\partial z}(\eta\frac{\partial u}{\partial z}) \\ &+ \frac{1}{r}\frac{\partial}{\partial r}[\eta r(\frac{\partial u}{\partial r} + \frac{\partial v}{\partial z})] + \mu_0\sigma\Re[\dot{E}_\theta^{*(1)}\dot{H}_r^{*(1)}] + \mu_0\sigma\Re[\dot{E}_\theta^{*(2)}\dot{H}_r^{*(2)}] + S_{\mathrm{p}}^{M_z} \end{aligned} \tag{4.11}$$

Radial:

$$\begin{aligned} &\rho u\frac{\partial v}{\partial z} + \rho v\frac{\partial v}{\partial r} \\ &= -\frac{\partial p}{\partial r} + \frac{\partial}{\partial z}[\eta(\frac{\partial v}{\partial z} + \frac{\partial u}{\partial r})] \\ &+ \frac{2}{r}\frac{\partial}{\partial r}(\eta r\frac{\partial v}{\partial r}) - 2\eta\frac{v}{r^2} + \mu_0\sigma\Re[\dot{E}_\theta^{*(1)}\dot{H}_z^{*(1)}] + \mu_0\sigma\Re[\dot{E}_\theta^{*(2)}\dot{H}_z^{*(2)}] + S_{\mathrm{p}}^{M_r} \end{aligned} \tag{4.12}$$

Swirl:

$$\begin{aligned}\rho u\frac{\partial w}{\partial z}+\rho v\frac{\partial w}{\partial r}&\\ =\ \frac{\partial}{\partial z}\left(\eta\frac{\partial w}{\partial z}\right)+\frac{1}{r}\frac{\partial}{\partial r}\left(r\eta\frac{\partial w}{\partial r}\right)&\\ -\ \frac{\rho vw}{r}-\frac{w}{r}\frac{\partial r\eta}{\partial r}&\end{aligned}\tag{4.13}$$

Energy conservation.

$$\begin{aligned}\rho u\frac{\partial h}{\partial z}+\rho v\frac{\partial h}{\partial r}&\\ =\ \frac{\partial}{\partial z}(\frac{\lambda}{C_{\rm p}}\frac{\partial h}{\partial z})+\frac{1}{r}\frac{\partial}{\partial r}(r\frac{\lambda}{C_{\rm p}}\frac{\partial h}{\partial r})&\\ +\ \sigma|\dot{E}_\theta^{(1)}|^2+\sigma|\dot{E}_\theta^{(2)}|^2-P_{\rm rad}-S_{\rm p}^E&\end{aligned}\tag{4.14}$$

Mass transport equation for Ti vapour.

$$\begin{aligned}\rho u\frac{\partial Y_{\rm Ti}}{\partial z}+\rho v\frac{\partial Y_{\rm Ti}}{\partial r}&\\ =\ \frac{\partial}{\partial z}(\rho D_{\rm Ar/O_2-Ti}\frac{\partial Y_{\rm Ti}}{\partial z})+\frac{1}{r}\frac{\partial}{\partial r}(r\rho D_{\rm Ar/O_2-Ti}\frac{\partial Y_{\rm Ti}}{\partial r})+S_{\rm p}^C&\end{aligned}\tag{4.15}$$

Maxwell equation in the upper coil.

$$\frac{\partial^2\dot{A}_\theta^{(1)}}{\partial z^2}+\frac{1}{r}\frac{\partial}{\partial r}(r\frac{\partial\dot{A}_\theta^{(1)}}{\partial r})-\frac{\dot{A}_\theta^{(1)}}{r^2}=j\mu_0\sigma\omega^{(1)}\dot{A}_\theta^{(1)}\tag{4.16}$$

$$\dot{H}_z^{(1)}=\frac{1}{\mu_0}\frac{1}{r}\frac{\partial}{\partial r}(r\dot{A}_\theta^{(1)}),\quad \dot{H}_r^{(1)}=-\frac{1}{\mu_0}\frac{\partial\dot{A}_\theta^{(1)}}{\partial z}\tag{4.17}$$

$$\dot{E}_\theta^{(1)}=-j\omega^{(1)}\dot{A}_\theta^{(1)}\tag{4.18}$$

Maxwell equation in the lower coil.

$$\frac{\partial^2\dot{A}_\theta^{(2)}}{\partial z^2}+\frac{1}{r}\frac{\partial}{\partial r}(r\frac{\partial\dot{A}_\theta^{(2)}}{\partial r})-\frac{\dot{A}_\theta^{(2)}}{r^2}=j\mu_0\sigma\omega^{(2)}\dot{A}_\theta^{(2)}\tag{4.19}$$

$$\dot{H}_z^{(2)}=\frac{1}{\mu_0}\frac{1}{r}\frac{\partial}{\partial r}(r\dot{A}_\theta^{(1)}),\quad \dot{H}_r^{(2)}=-\frac{1}{\mu_0}\frac{\partial\dot{A}_\theta^{(2)}}{\partial z}\tag{4.20}$$

$$\dot{E}_\theta^{(2)}=-j\omega^{(2)}\dot{A}_\theta^{(2)}\tag{4.21}$$

where the superscripts (1) and (2) denote the element from the upper coil and lower coil, respectively. In those equations, superscripts (1) and (2) respectively denote the elements from the upper coil and lower coil. Also in those equations, the following variables are

used: r, radial position; v, radial flow velocity; u, axial flow velocity; z, axial position; η, viscosity; ρ, mass density; λ, thermal conductivity; p, pressure; h, enthalpy; σ, electrical conductivity; C_{p}, specific heat at constant pressure; Y_{Ti}, mass fraction of Ti vapour; P_{rad}, radiative loss; μ_0, permeability of vacuum; $D_{\mathrm{Ar/O_2-Ti}}$, effective diffusion coefficient of Ti vapour in $\mathrm{Ar/O_2}$ gas; and j, complex factor (j^2=−1). The following must also be noted: $\dot{E}_\theta^{(1),(2)}$ respectively denote phasors of the electric field strength in upper coil and lower coil; $\dot{A}_\theta^{(1),(2)}$, respectively represent phasors of the vector potential in the upper coil and lower coil; $\omega^{(1),(2)}$, respectively stand for frequencies of the upper coil and lower coil current; $\dot{H}_z^{(1),(2)}$ respectively represent phasor axial components of the magnetic field strength in the upper coil and lower coil; and $\dot{H}_r^{(1),(2)}$ respectively denote phasor radial components of the magnetic field strength in the upper coil and lower coil.

The asterisks * in equations (4.11) and (4.12) denote the conjugate. A symbol $\Re$ is the real part of the phasor. The magnitudes of the phasor including $\dot{A}_\theta$, $\dot{E}_\theta$, $\dot{H}_z$, and $\dot{H}_r$ are defined as root mean square values. The quantities S_{p}^C, $S_{\mathrm{p}}^{M_z}$, $S_{\mathrm{p}}^{M_r}$, and S_{p}^E denote source terms by the translation quantities from evaporated material. These quantities are explained in the next section.

4.3.4 Interaction between Ti particles and tandem coil thermal plasma

Evaporated titanium vapour from Ti particles can be a source of mass, momentum, and energy of plasma equations. Letting n_d be the particle size distribution, N_t^0 be the value of particles injected per unit time, and n_r describe the fraction N_t^0 injected at each point over the torch central inlet, then the number of particles per unit time travelling throughout trajectory (l, k) to a particle diameter d_l injected at point r_k is expressed as the following equation.

$$N^{l,k} = n_{d_l} n_{r_k} N_{\mathrm{t}}^0 \tag{4.22}$$

For this calculation, the n_r particle concentration was assumed to be uniform for five positions of the particle in the inlet. The initial particle size distribution and the initial positions of particle injection were as they are depicted in figure 4.4. Particles were assumed to be injected at five radial initial positions of r =0.3 mm, 0.6 mm, 0.9 mm, 1.2 mm, and

1.5 mm. Also, particles were assumed to consist of particles with seven discrete diameters, as presented in the lower panel in figure 4.4. Furthermore, these seven discrete diameter particles were assumed to have a Gaussian distribution fraction. In this case, the following were found: 3% of the particles have diameters of 4.0 μm and 6.0 μm; 7% of the particles have diameters of 4.33 μm and 5.67 μm; 10% of the particles have diameters of 4.67 μm, and 5.33 μm; and the remaining 60% of the whole particles have mean diameter of 5.0 μm. These particles have 35 possible trajectories from the conditions offered: 7×5. Consequently, there are 35 trajectories for particles with five initial positions and seven diameters. The 35 trajectories were finished for statistical calculation on the particle size change and its effects on the thermal plasma temperature. The initial particle injection velocity was set as equal to the carrier gas velocity. The source term in the continuity of mass conservation equation S_{p}^{C} is the net mass efflux rate of the particle mass in a numerical computational cell (control volume). Based on the assumption that the particles are spherical, the mass efflux rate of the particles attributable to the particle trajectory (l,k) traversing a given cell (i,j) is given as shown below.

$$S_{\mathrm{p},ij}^{C(l,k)} = \frac{1}{6}\pi\rho_{\mathrm{p}}N_{ij}^{(l,k)}(d_{ij,\mathrm{in}}^{3} - d_{ij,\mathrm{out}}^{3}). \tag{4.23}$$

The net mass efflux rate from the particle can be derived by summing over all particle trajectories traversing a given cell.

$$S_{\mathrm{p},ij}^{C} = \sum_{l}\sum_{k} S_{\mathrm{p},ij}^{C(l,k)}. \tag{4.24}$$

The momentum source terms are estimated in the same model as the particle mass source terms. For this calculation, the mass efflux rate of particle momentum during the particle trajectory (l,k) traversing a given cell (i,j), which are explained as the quantities $S_{\mathrm{p}}^{M_z}$ and $S_{\mathrm{p}}^{M_z}$, are described as shown below.

$$S_{\mathrm{p},ij}^{M_z(l,k)} = \frac{1}{6}\pi\rho_{\mathrm{p}}N_{ij}^{(l,k)}(u_{ij,\mathrm{in}}d_{ij,\mathrm{in}}^{3} - u_{ij,\mathrm{out}}d_{ij,\mathrm{out}}^{3}) \tag{4.25}$$

$$S_{\mathrm{p},ij}^{M_r(l,k)} = \frac{1}{6}\pi\rho_{\mathrm{p}}N_{ij}^{(l,k)}(v_{ij,\mathrm{in}}d_{ij,\mathrm{in}}^{3} - v_{ij,\mathrm{out}}d_{ij,\mathrm{out}}^{3}) \tag{4.26}$$

The corresponding momentum source terms are presented below.

$$S_{\mathrm{p},ij}^{M_z} = \sum_{l}\sum_{k} S_{\mathrm{p},ij}^{M_z(l,k)} \tag{4.27}$$

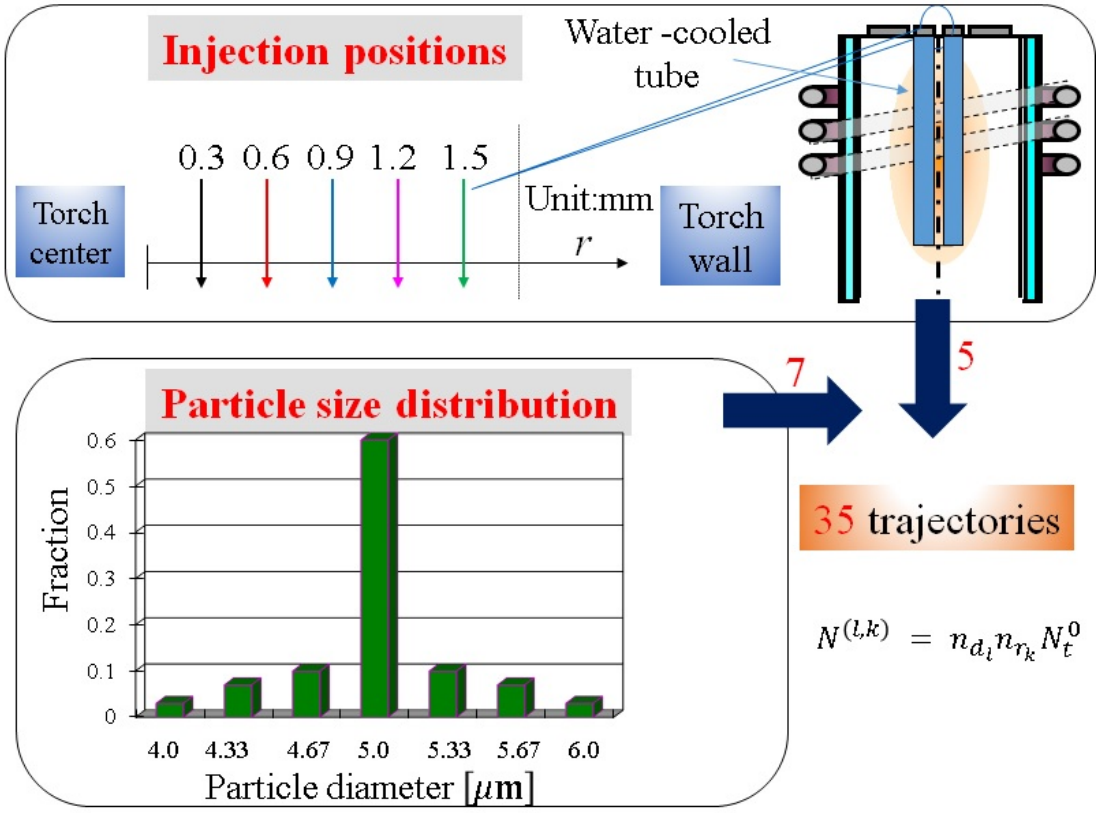

Fig. 4.4: Particle size distribution and particle injection positions.

$$S_{\mathrm{p},ij}^{M_r} = \sum_l \sum_k S_{\mathrm{p},ij}^{M_r(l,k)}. \tag{4.28}$$

The energy source term includes the heat flux given to the particles $Q_{\mathrm{p},ij}^{(l,k)}$, and superheat to bring the particle vapour into thermal equilibrium with the plasma $Q_{\mathrm{v},ij}^{(l,k)}$. The quantity S_{p}^{E} is expressed using $Q_{\mathrm{p},ij}^{(l,k)}$ and $Q_{\mathrm{v},ij}^{(l,k)}$ as given by the following.

$$Q_{\mathrm{p},ij}^{(l,k)} = \int_{\tau_{\mathrm{in}}}^{\tau_{\mathrm{out}}} \pi d_{\mathrm{p}}^2 h_c [T_{ij} - T_{\mathrm{p},ij}^{(l,k)}] dt \tag{4.29}$$

$$Q_{\mathrm{v},ij}^{(l,k)} = \int_{\tau_{\mathrm{in}}}^{\tau_{\mathrm{out}}} \frac{\pi}{2} d_{\mathrm{p}}^2 \rho_{\mathrm{p}} \left(\frac{d d_{\mathrm{p}}}{dt} \right) C_{\mathrm{pp}} [T_{ij} - T_{\mathrm{p},ij}^{(l,k)}] dt \tag{4.30}$$

$$S_{\mathrm{p},ij}^{E} = \sum_l \sum_k N_{ij}^{(l,k)} [Q_{\mathrm{p},ij}^{(l,k)} + Q_{\mathrm{v},ij}^{(l,k)}] \tag{4.31}$$

4.3.5 Thermodynamic and transport properties of Ti bulk, Ar-O_2-Ti system

For this calculation, thermodynamic and transport properties of $Ar/O_2/Ti$ gas mixture are necessary. The thermodynamic and transport properties were calculated in a similar way to our previous work [32]. For this purpose, the equilibrium composition of Ar/O_2 mixture with Ti vapour was first calculated using minimization of the Gibbs' free energy of a system. Figure 4.5(a) presents the calculated equilibrium composition of 90%Ar/10%O_2 thermal plasma without Ti vapour at a pressure of 300 Torr as a function of temperature. As shown there, oxygen molecule O_2 is dissociated at temperatures around 3000 K to produce O atoms, leading to the similar densities 5×10^{22} m^{-3} both for O_2 and O atom. A further increase in the temperature from 8000 K involves the ionization of Ar and O atoms, resulting in increased electron density and ion density. In the case of Ti vapour consideration, species such as Ti, Ti^+, Ti^{2+}, TiO(g) and TiO_2(g) in gas phase were considered in the equilibrium composition. For simplicity, species in liquid and solid phases were neglected because the thermodynamic and transport properties of these gas mixture were used for plasma and gas phase. Figure 4.5(b) depicts the calculated equilibrium composition of 89%Ar/10%O_2 thermal plasma with 1%Ti vapour at a pressure of 300 Torr. At temperatures below 2000 K TiO_2(g) in gas phase is dominant, whereas TiO has high density above 10^{21} m^{-3} around temperatures 3000-4500 K. At temperatures above 4500 K, Ti atoms are present and then it is ionized to produce Ti^+ and electron even above 4500 K. In the temperature range below 8000 K, the electron is supplied from ionization of Ti.

Using the equilibrium composition calculated above, thermodynamic properties of 100%Ar gas, 90%Ar-10%O_2 gas mixture, 100%Ti vapor and Ar-O_2-Ti gas mixture were computed such as the mass density, the enthalpy, the specific heat as a function of temperature at the specified pressure. Furthermore, the transport properties of the electrical conductivity, thermal conductivity, and viscosity were calculated by the first-order approximation of Chapman–Enskog method [30, 31] using the calculated collision integrals between the considered species. The collision integrals between atoms were obtained by Monchick data [34] using interatomic potential [33]. The collision integrals between the same ion-atom with charge exchange were obtained by Rapp data [36] using the expression by Yos [30]. These calculated thermodynamic and transport data were used to calculate the temperature and

gas flow fields in tandem ICTPs. Figures 4.6, 4.7 and 4.8 show the specific heat at constant pressure, thermal conductivity and viscosity of 100%Ar gas, 90%Ar-10%O_2 gas mixture, 100%Ti vapor, and 89%Ar-10%O_2-1%Ti gas mixture at 300 torr, as examples of the calculated thermodynamic and transport properties. Generally, the specific heat has peculiar peaks due to dissociation reactions and ionization reactions. At the same time, there are also similar peculiar peaks in the thermal conductivity from reactional thermal conductivity due to dissociation and ionization reactions. As depicted in figures 4.6 and 4.7, the specific heat and the thermal conductivity for 90%Ar-10%O_2 gas mixture have a peak at temperatures around 3000 K whereas this peak does not appear in the specific heat for 100%Ar. This peak around 3000 K originates from the dissociation reaction of O_2. This peak can be seen in the specific heat and the thermal conductivity of 89%Ar-10%O_2-1%Ti gas mixture around 3000 K. Meanwhile, 100%Ti vapour shows peaks around 7500 K and 16000 K in the specific heat. These peaks arise from the first and second ionization of Ti atoms. Similarly, the thermal conductivity for 100%Ti also has a maximum around 7500 K. Figure 4.8 indicates the viscosity. This figure shows that 100%Ar gas, 90%Ar-10%O_2 gas mixture and 89%Ar-10%O_2-1%Ti gas mixture have similar viscosities. On the other hand, the viscosity of 100%Ti vapor has a peak at 5000 K and then the viscosity decreases with temperature from 5000 K because of Coulomb collisions between electrons and ions.

4.3.6 Boundary condition

Figure 4.9 shows the computational domain. The domain (A-B-C-D-E-F-G-H-I-A) was used for numerical simulation of scalar quantities and fluid parameters except the vector potentials. On the other hand, the domain (A-B-C-D-A) was adopted for the vector potentials. The following conditions were set at the boundary (A-B-C-D-E-F-G-H-I-A) of the calculation domain:

At A-I for the top center of the metal water-cooled pipe wall:

$$u = \frac{Q_{\text{carrier}}}{\pi r_1^2}, \tag{4.32}$$

$$v = 0,\ T = 300\,\text{K} \tag{4.33}$$

where r_1 is the inner radius (A-I) of the water-cooled pipe, Q_{carrier} is the gas flow rate of center carrier gas.

At F-G-H-I for the metal water-cooled pipe wall:

$$u = 0,\ v = 0,\ w = 0,\ T = 300\ \mathrm{K} \tag{4.34}$$

At E-F for the top center of the torch head:

$$u = 0,\ v = 0,\ w = 0,\ \ T = 300\ \mathrm{K} \tag{4.35}$$

At E-D for the top of the torch near the wall:

$$u = \frac{Q_{\mathrm{sheath}}}{\pi(r_{\mathrm{torch}}^2 - r_3^2)}, \tag{4.36}$$

$$v = 0,\ w = u\tan\theta_{\mathrm{swirl}},\ \ T = 300\ \mathrm{K} \tag{4.37}$$

where r_{torch} is the inner radius (D) of the plasma torch, r_2 is the inlet radius (E) for the sheath gas injection, Q_{sheath} is the gas flow rate of sheath gas, θ_{swirl} is the swirl angle at the inlet which was set to 23.5° in the present calculation.

At A-B for the center axis of the torch:

$$\frac{\partial u}{\partial r} = 0,\ v = 0,\ \frac{\partial w}{\partial r} = 0,\ \frac{\partial h}{\partial r} = 0, \tag{4.38}$$

$$\dot{A}_\theta^{(1)} = \dot{A}_\theta^{(2)} = 0 \tag{4.39}$$

At B-C for the bottom of the torch:

$$\frac{\partial(\rho u)}{\partial z} = 0,\ \frac{\partial v}{\partial z} = 0,\ \frac{\partial w}{\partial z} = 0,\ \frac{\partial h}{\partial z} = 0, \tag{4.40}$$

At C-D for quartz torch wall:

$$u = 0,\ v = 0,\ w = 0,\ \kappa\frac{\partial T}{\partial r} = \frac{\kappa_{\mathrm{qua}}}{\delta_{\mathrm{qua}}}(T - T_{\mathrm{water}}),\ T_{\mathrm{water}} = 300\ \mathrm{K} \tag{4.41}$$

For vector potential for C-D, B-C and A-D, we calculated the vector potential from coil currents and current inside the plasmas as boundary condition:

$$\begin{aligned}
\dot{A}_\theta^{(1)} &= \frac{\mu_0 I^{(1)}}{2\pi}\sum_{n=1}^{n_{\mathrm{coil}}^{(1)}}\sqrt{\frac{r_{\mathrm{coil}_n}^{(1)}}{r}}G(k_n) + \frac{\mu_0}{2\pi}\int\int\sqrt{\frac{r'}{r}}\sigma\dot{E}_\theta^{(1)}G(k)dr'dz' \\
\dot{A}_\theta^{(2)} &= \frac{\mu_0 I^{(2)}}{2\pi}\sum_{n=1}^{n_{\mathrm{coil}}^{(2)}}\sqrt{\frac{r_{\mathrm{coil}_n}^{(2)}}{r}}G(k_n) + \frac{\mu_0}{2\pi}\int\int\sqrt{\frac{r'}{r}}\sigma\dot{E}_\theta^{(2)}G(k)dr'dz'
\end{aligned} \tag{4.42}$$

$$k_n^2 = \frac{4r_{\mathrm{coil}_n}r}{(r_{\mathrm{coil}_n} + r)^2 + (z_{\mathrm{coil}_n} - z)^2}$$

$$k^2 = \frac{4r'r}{(r' + r)^2 + (z' - z)^2}$$

$$G(k) = \frac{(2 - k^2)K(k) - 2E(k)}{k}$$

where, κ_{qua} is the thermal conductivity of quartz [W/(m·K)], δ_{qua} is the thickness of quartz tube [m], T_{water} is the cooling water temperature [K], $r^{(1)}_{\mathrm{coil}_n}$ is the radius of the n-th coil in the upper coil, $r^{(2)}_{\mathrm{coil}_n}$ is the radius of the n-th coil in the lower coil, $z^{(1)}_{\mathrm{coil}_n}$ is the axial position of the n-th coil in the upper coil, $z^{(2)}_{\mathrm{coil}_n}$ is the axial position of the n-th coil in the lower coil, r' and z' are the position parameter to calculate the above integration. $K(k)$ and $E(k)$ are respectively the complete elliptic integral of the first kind, and the complete elliptic integral of the second kind.

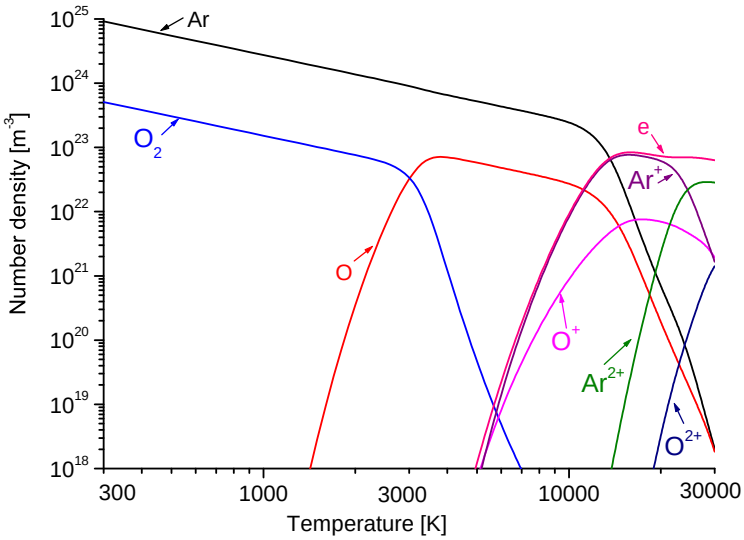

(a)

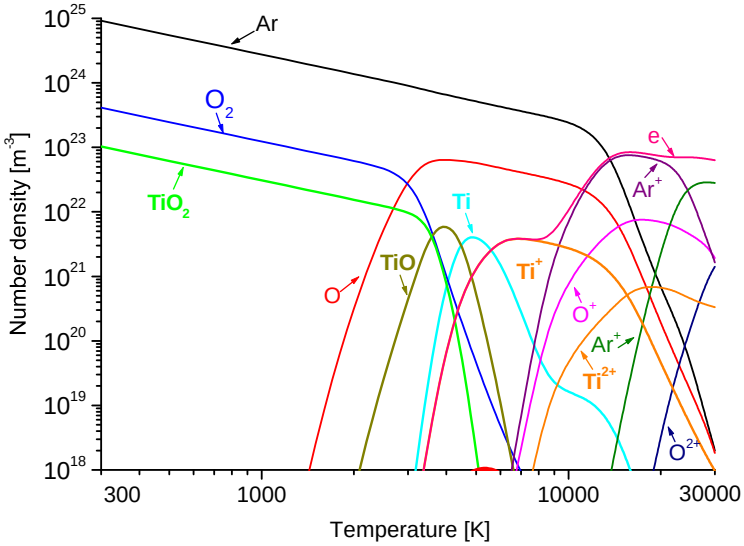

(b)

Fig. 4.5: Number density of (a) 90%Ar-10%O_2 and (b) 89%Ar-10%O_2-1%Ti thermal plasmas at a pressure of 300 Torr.

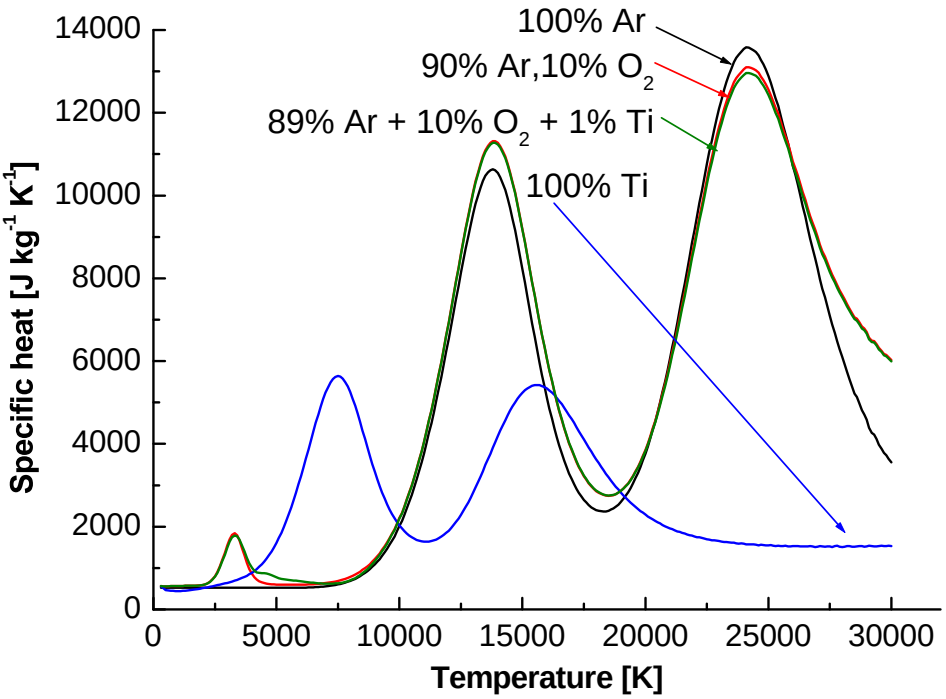

Fig. 4.6: Specific heat of 100%Ar gas, 90%Ar-10%O_2 gas mixture, 89%Ar-10%O_2-1%Ti gas mixture and 100%Ti vapor as a function of temperature at 300 Torr pressure.

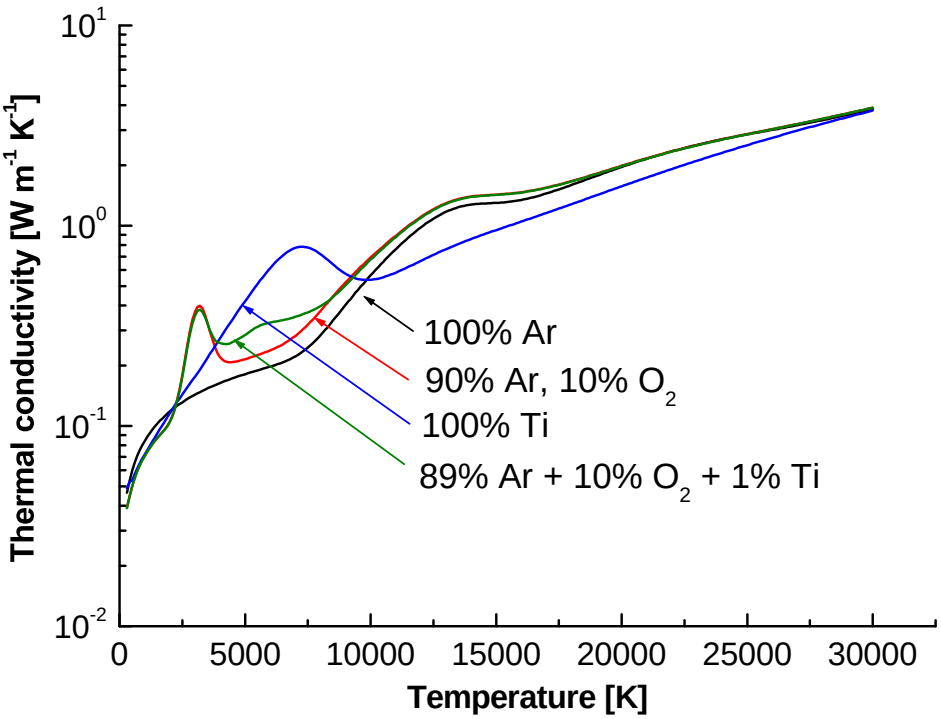

Fig. 4.7: Thermal conductivity of 100%Ar gas, 90%Ar-10%O_2 gas mixture, 89%Ar-10%O_2-1%Ti gas mixture and 100%Ti vapor as a function of temperature at 300 Torr pressure.

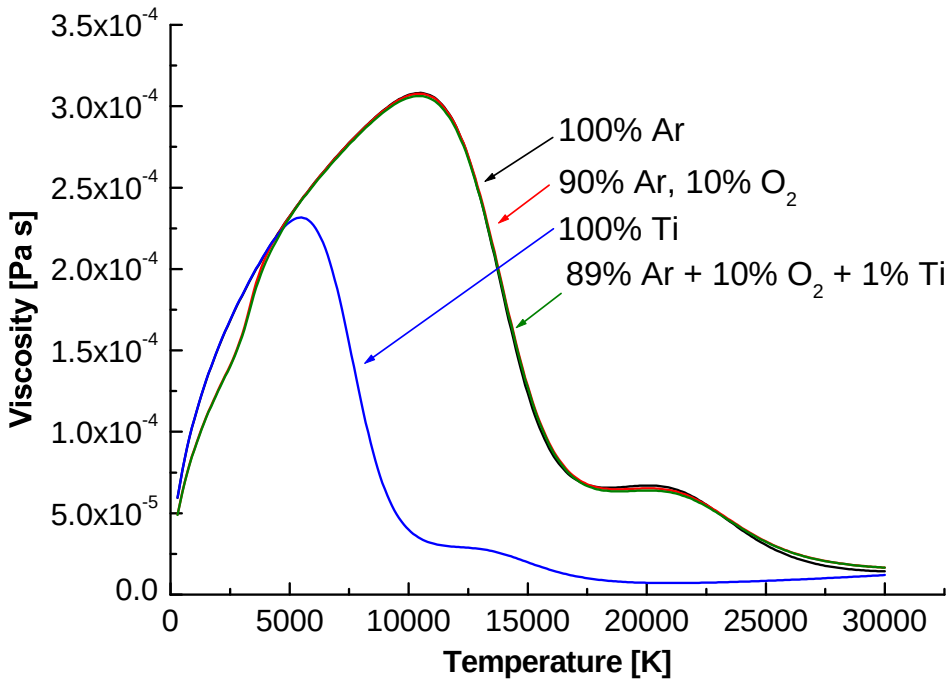

Fig. 4.8: Viscosity of 100%Ar gas, 90%Ar-10%O_2 gas mixture, 89%Ar-10%O_2-1%Ti gas mixture and 100%Ti vapor as a function of temperature at 300 Torr pressure

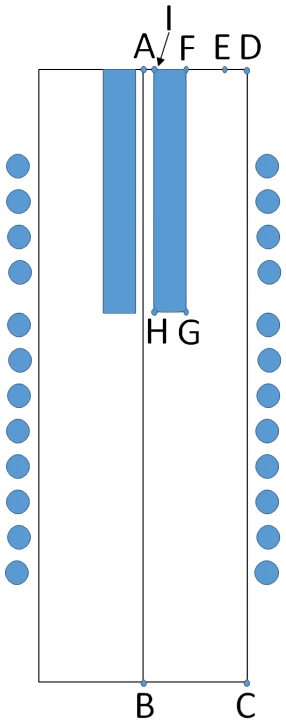

Fig. 4.9: A full-set of boundary conditions.

4.3.7 Calculation conditions for single-frequency coil ICTP and tandem coil ICTP

As explained previously, two main situations were considered: One condition is that in which two separate coils in one plasma torch were connected in series with one power source at a single operating frequency. Thereby, the resulting electromagnetic fields are created with one frequency. This situation is designated herein as a 'single-frequency coil'. The other condition is that in which two separate coils arranged on one plasma torch were connected with two independent power sources at different frequencies. In this case, the resulting electromagnetic fields have two frequency components. This situation is designated herein as 'tandem double-frequency coil' for clarification.

For this calculation, the driving frequencies of the upper coil and lower coil current for the tandem double-frequency coil ICTP were fixed respectively at 450 kHz and 300 kHz. Generally, the input power in the upper coil is 10 kW and that of the lower coil is 15 kW for all conditions of tandem double-frequency coil ICTP. However, the frequency and input power of single-frequency coil were set respectively as 450 kHz and 25 kW. The pressure was set at 300 Torr (=40 kPa) inside the chamber. The calculation conditions are presented in Table 4.1. The flow rates of the Ar and O_2 gas mixture used as sheath gas were set respectively to 90 slpm and 10 slpm. The titanium feedstock powder was assumed to be injected through a water-cooled pipe inserted on the torch axis from the plasma torch head. The injection rate of Ti feedstock powder was set to 0.1 g/min. Table 4.2 presents the thermodynamic properties of titanium feedstock powder used for calculations. From these calculations, we assessed the mutual effects of gap distance between coils in tandem double-frequency coil ICTP. In addition, calculation was done for single-coil ICTP with eight turns for comparison.

Table 4.1: Numerical conditions

Parameter	Single-freq. coil (8-turn coil)	Tandem coil (8 and 12-turn coils)
Input power [kW]	25	
- Upper coil		10
- Lower coil		15
Frequency [kHz]	450	
- Upper coil		450
- Lower coil		300
Sheath gas flow rate [L/min]	90	90
Feeding powder rate [g/min]	0.1	0.1
Carrier gas flow rate [L/min]	10	10
Pressure [Torr]	300	300

Table 4.2: Thermodynamic properties of titanium powder [37].

Parameter	Condition
Injection load [g/min]	0.1
Mass density [kg/m^3]	4506
Melting temperature [K]	1853
Boiling temperature [K]	3535
Latent heat for melting [J/kg]	391000
Latent heat of evaporation [J/kg]	8294000
Specific heat of solid [J/(kg K)]	528
Specific heat of liquid [J/(kg K)]	700
Thermal conductivity [W/(m K)	14

4.4 Calculation Results

4.4.1 Temperature distribution of thermal plasma

4.4.1.1 Temperature distribution of single-frequency coil ICTP

Calculations were first conducted for an Ar-O_2 single-frequency coil ICTP with Ti feedstock powder injection for comparison with a tandem double-frequency coil ICTP as described later. A single-frequency coil has coils that are operated with the same current and the same operating frequency of 450 kHz. In this case, the total input power to the ICTP was set as 25 kW.

Figures 4.10(a)–4.10(d) respectively portray the temperature distribution of the single-frequency coil ICTP with gap lengths of 20 mm, 30 mm, 40 mm, and 60 mm. For gap length of 20 mm, as shown in figure 4.10(a), which corresponds to a situation of a so-called single coil, the single-frequency coil ICTP has a region with temperatures above 13 000 K for radial positions of 16 mm$< r <$30 mm and axial positions of 170 mm$< z <$ 215 mm. The high temperature region is located at the downward of the single coil because of the gas flow from the top of the plasma torch. In this high-temperature region, the current flows inside the thermal plasma to be heated. As portrayed in figures 4.10(b), 4.10(c), and 4.10(d) with respective gap lengths of 30 mm, 40 mm, and 60 mm, the regions with temperatures above 13 000 K are shifted respectively down at axial positions of 185 mm $< z <$ 230 mm, 195 mm $< z <$240 mm and 200 mm$< z <$ 250 mm, without separation of the high-temperature region. This shift indicates that increasing gap length between the single-frequency coils from 20 mm to 60 mm leads to the high-temperature region located down as a lump. However, at the upstream portion around the upper coil, the temperature is low: no thermal plasma is created there. Positioning of the ICTP at the downward region in the plasma torch can make it unstable against disturbance from powder injection. Another important point related to different gap lengths is that the region with temperatures 10 000 K is spread wider by increasing the gap distance. This wide spread of the high-temperature region above 10 000 K is attributable more to the locally input power to this region by joule heating.

The downward positioning of the ICTP by increasing gap length is more readily apparent in figure 4.11. Figure 4.11 presents the axial temperature distribution at r=25 mm for

different gap lengths. This figure displays the increasing gap length shifts clearly in the high-temperature region downward in the axial direction with almost identical maximum temperature. The radial temperature distributions at z =230 mm are shown in figure 4.12. As depicted here, increasing the gap length coil from 20 mm to 60 mm leads to enlargement in the high-temperature region with temperatures higher than 10 000 K. This enlargement in the high-temperature region is again attributable to more locally input power to the localized ICTP by joule heating. To clarify this effect, the power density distributions are presented in figure 4.13 for different gap lengths. As this figure shows, the increasing gap length increases the power density itself; then the high power density region is shifted more downward.

This calculation result indicates that the elongation of gap length between the coils for the single-frequency coil ICTP alone does not yield a separate high-temperature region. The high-temperature region is merely shifted in the axial direction by different gap lengths, although a separate high-temperature region in the ICTP was expected when using a separate coil.

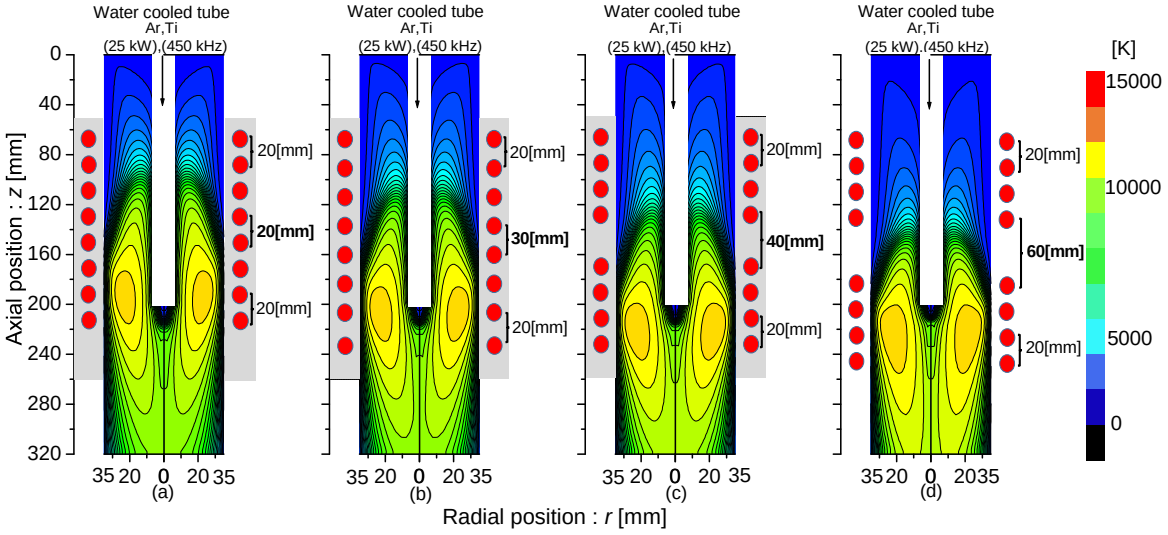

Fig. 4.10: Temperature distribution in Ar-O_2 single-frequency coil ICTP with Ti powder injection at different gap lengths of (a) 20 mm, (b) 30 mm, (c) 40 mm, and (d) 60 mm. The coil is operated at an input power of 25 kW at a frequency of 450 kHz.

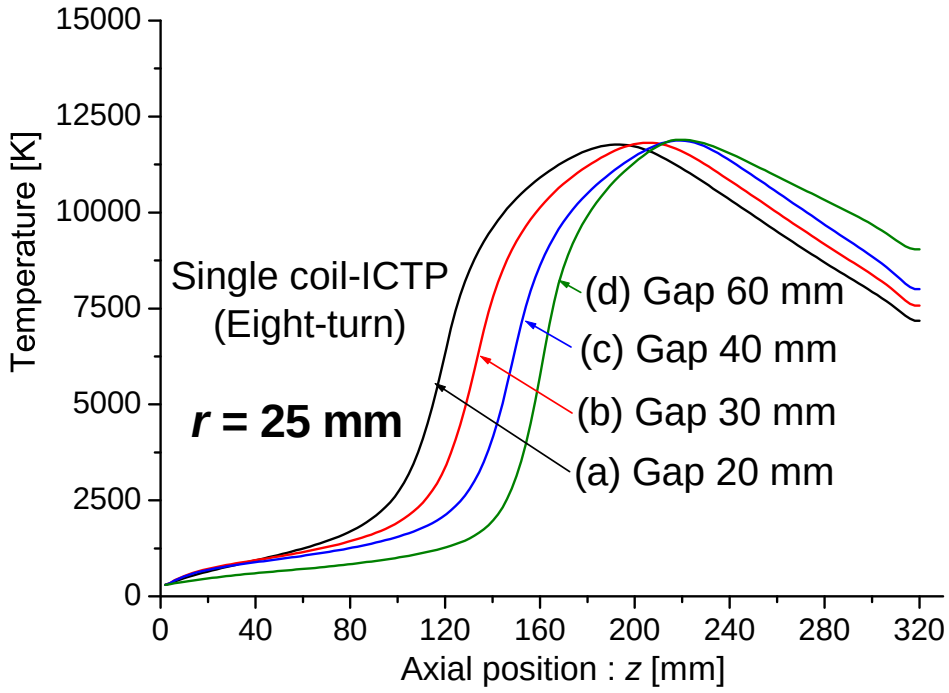

Fig. 4.11: Axial temperature distribution at radial position of 25 mm in Ar-O_2 single-frequency coil ICTP with Ti powder injection at different gap lengths of (a) 20 mm, (b) 30 mm, (c) 40 mm, and (d) 60 mm. The coil is operated at an input power of 25 kW at a frequency of 450 kHz.

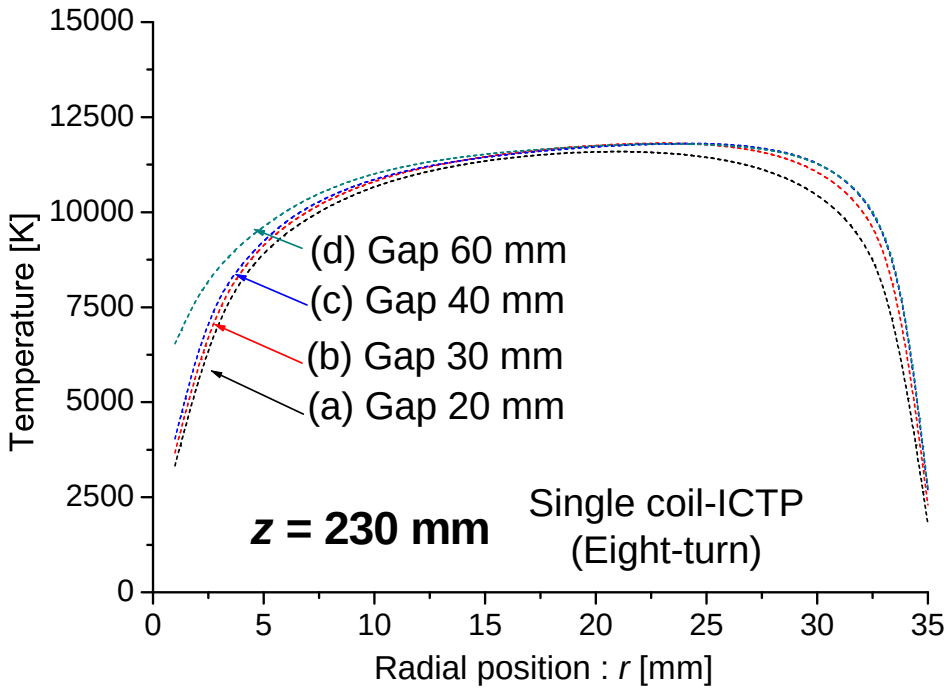

Fig. 4.12: Radial temperature distribution at axial position of 230 mm in Ar-O_2 single-frequency coil ICTP with Ti powder injection at different gap lengths of (a) 20 mm, (b) 30 mm, (c) 40 mm, and (d) 60 mm. The coil is operated at an input power of 25 kW at a frequency of 450 kHz.

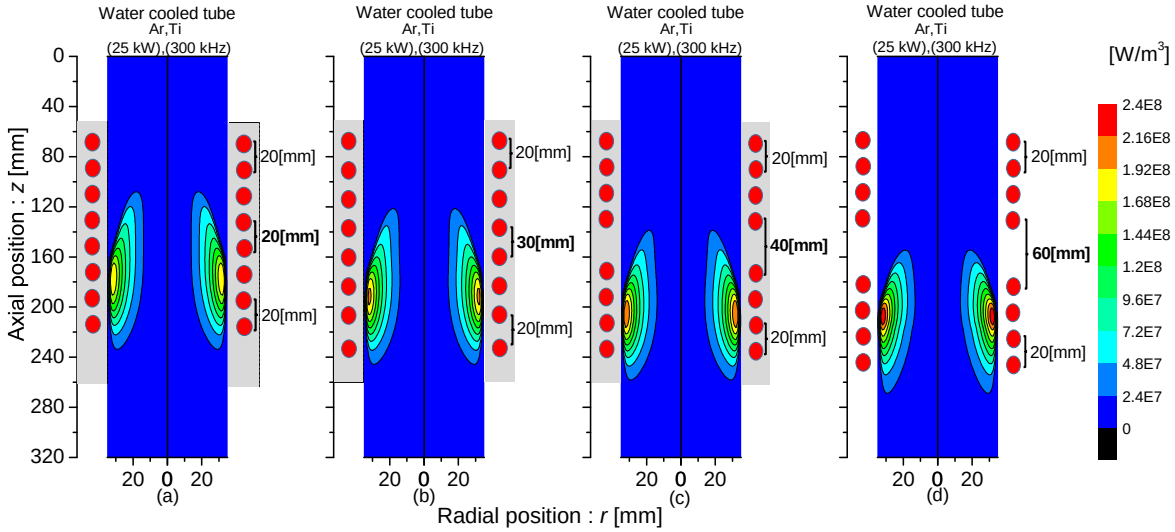

Fig. 4.13: Power density distribution in Ar-O_2 single-frequency ICTP with Ti powder injection at different gap lengths of (a) 20 mm, (b) 30 mm, (c) 40 mm, and (d) 60 mm. The coil is operated at an input power of 25 kW at a frequency of 450 kHz.

4.4.1.2 Temperature distribution of tandem double-frequency ICTP with an 8-turn coil

For a single-frequency coil, not a separate high-temperature region but an aggregated high-temperature region was obtained. As described in this section, different operating frequencies are used for two tandem double-frequency coils.

Figures 4.14(a)–4.14(d) respectively portray the temperature distribution in tandem double-frequency coil ICTP with eight turns, with coil gaps of 20 mm, 30 mm, 40 mm, and 60 mm. As shown in this calculation, the input power from the upper coil was set to 10 kW at 450 kHz, whereas the input power from the lower coil was fixed respectively to 15 kW at 300 kHz. As seen in these figures, the temperature distributions in axial position from z=0 mm to z=100 mm, i.e. in the upper coil region, were almost unchanged with increasing gap length. This indicates that the ICTP in the upper coil region is stably established almost independent of the lower coil region where the ICTP is influenced by feedstock injection. For gap lengths of 20–60 mm, almost one lumped high-temperature region was obtained. The high-temperature region above 10000 K is located more upward than those for a single-frequency coil ICTP indicated in figure 4.10, because the tandem double-frequency coil ICTPs alway form from the upper coil region. In addition, the high-temperature region becomes axially longer by increasing gap length between the coils from 20 mm to 60 mm. At a gap length of 60 mm, the maximum temperature is 10500 K, which is lower than those in single-frequency coil ICTPs. This is due to the fact that input power was spread in a axially wider region in the tandem double-frequency coils than the single-frequency coil. Another important point in figure 4.14(d) with a gap length of 60 mm is that the ICTP has a maximum temperature near the tip of the water-cooled feeing pipe. This can be used for evaporation of feedstock.

Furthermore, the axial temperature distribution at r=25 mm and the radial temperature distribution at z =230 mm are also illustrated respectively in figure 4.15 and figure 4.16, to elucidate differences in the temperatures in each condition. As presented in figure 4.15, the axial temperature in tandem double-frequency coil ICTP (eight turns) has a peak around the axial position of z=140 mm at a gap length of 20 mm. This peak has a temperature around 11200 K, resulting in one lumped high temperature region in the torch. Increasing gap lengths from 20 mm to 40 mm elevates the temperature downstream from z=180 mm to

z=320 mm while maintaining the temperature distribution as almost unchanged from z=0 mm to z = 120 mm. On the other hand, at a gap length of 60 mm, the axial temperature in tandem double-frequency coil ICTP has two peaks at z=115 mm in the upper coil, at z=175 mm in the beginning of the lower coil, as portrayed in figure 4.15(d). These two peaks in axial temperature distribution is attributable to the independent input power from the upper coil and the lower coil in this case. As for the radial temperature distribution at axial position of z=230 mm in figure 4.16, the temperature at 5 mm$< r <$ 35 mm rises generally with increasing gap length. The temperature has a peak at inner radial position around r ∼20 mm from the wall compared with those for a single-frequency ICTP shown in figure 4.12. This inner positioned temperature peak is due to the inner input power from lower frequency of 300 kHz. Figure 4.17 portrays the power density distribution from joule heating in the tandem double-frequency coil ICTP torch with eight turns. As shown there, increasing gap length clearly elongates the high input power density region downward in the axial direction. Finally at 60 mm gap length, the high power density is distributed from z=80 mm to 210 mm in long region.

The two peaked high-temperature region in the ICTP described above might be useful for stable operation during feedstock powder injection processes because the high-temperature region in the upper coil is disturbed only slightly by feedstock powder injection. Also, the high-temperature region in the lower coil might be used for evaporation of the feedstock powder.

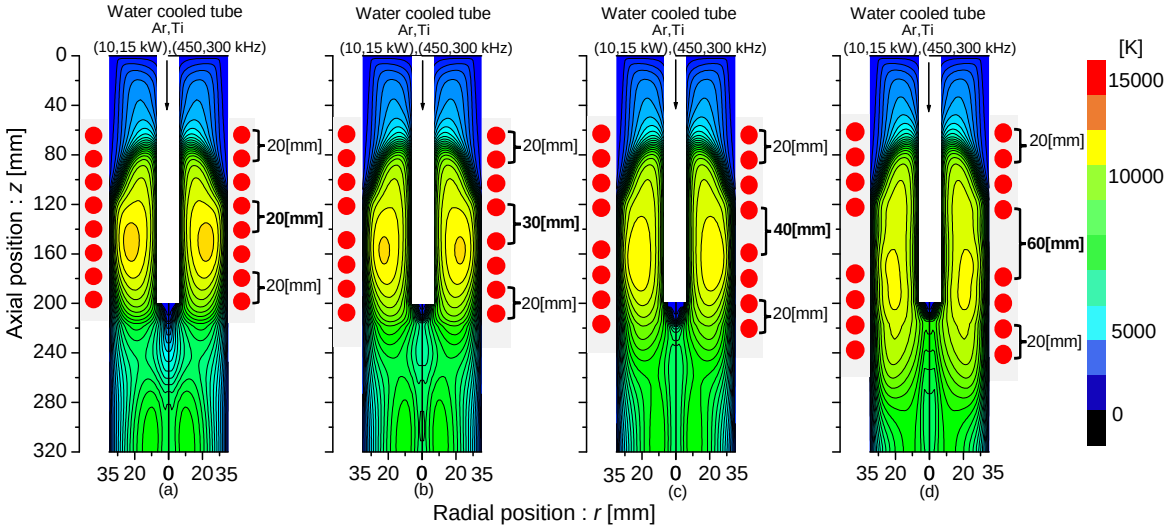

Fig. 4.14: Temperature distribution in Ar-O_2 tandem double-frequency ICTP by an 8-turn coil with Ti powder injection at different gap lengths of (a) 20 mm, (b) 30 mm, (c) 40 mm, and (d) 60 mm. The upper coil is operated at an input power of 10 kW at a frequency of 450 kHz, while the lower coil is operated at 15 kW and 300 kHz.

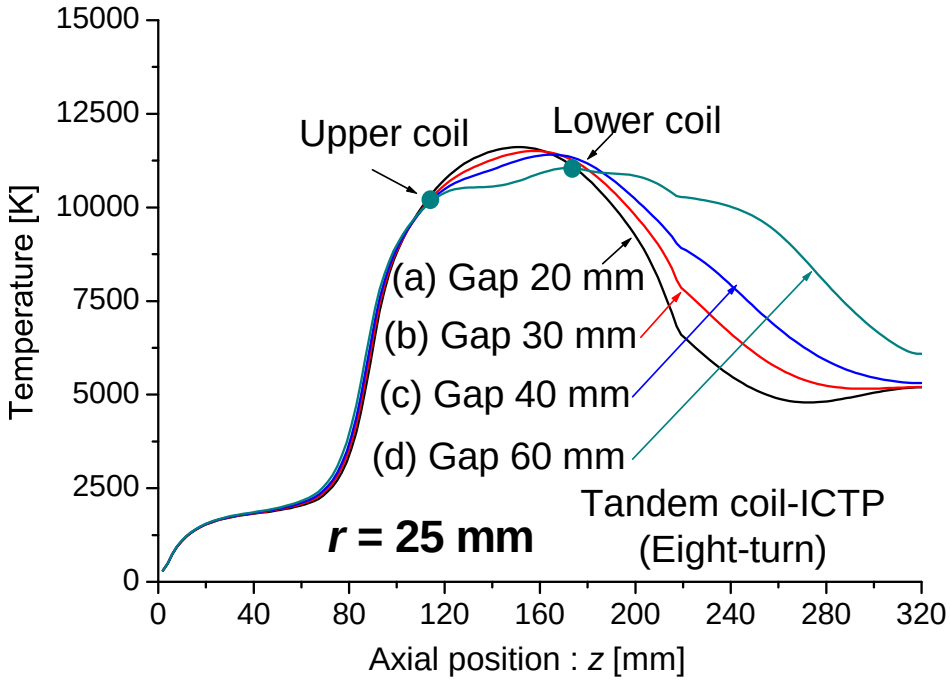

Fig. 4.15: Axial temperature distribution at a radial position of 25 mm in Ar-O_2 tandem double-frequency ICTP by an 8-turn coil with Ti powder injection at different gap lengths of (a) 20 mm, (b) 30 mm, (c) 40 mm, and (d) 60 mm. The upper coil is operated at an input power of 10 kW at a frequency of 450 kHz, while the lower coil is operated at 15 kW and 300 kHz.

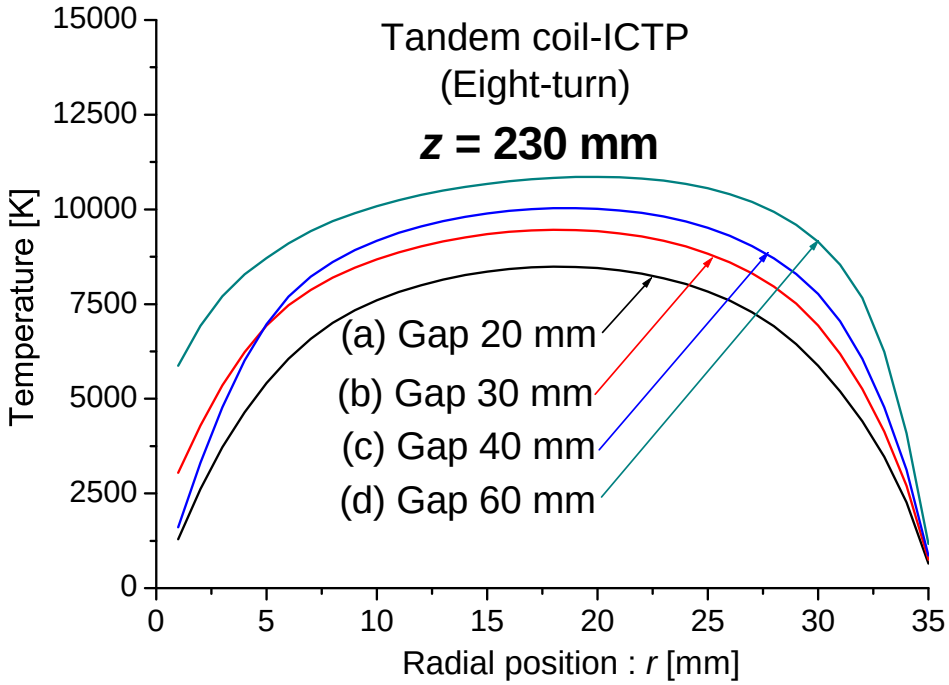

Fig. 4.16: Radial temperature distribution at an axial position of 230 mm in Ar-O_2 tandem double-frequency ICTP by an 8-turn coil with Ti powder injection at different gap lengths of (a) 20 mm, (b) 30 mm, (c) 40 mm, and (d) 60 mm. The upper coil is operated at an input power of 10 kW at a frequency of 450 kHz, while the lower coil is operated at 15 kW and 300 kHz.

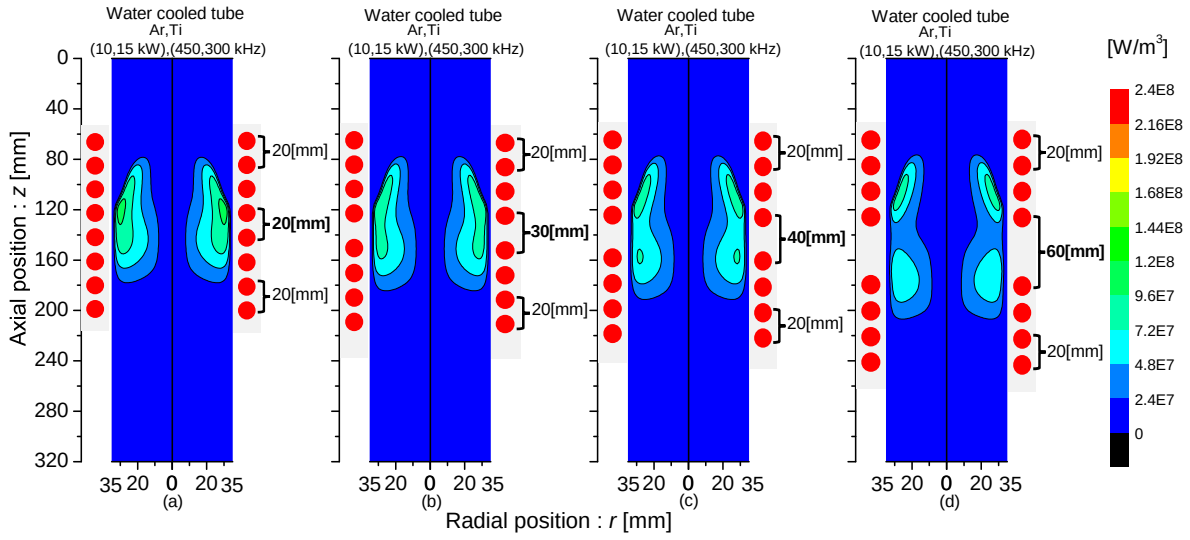

Fig. 4.17: Power density distribution in Ar-O_2 tandem double-frequency ICTP by an 8-turn coil with Ti powder injection at different gap lengths of (a) 20 mm, (b) 30 mm, (c) 40 mm, and (d) 60 mm. The upper coil is operated at an input power of 10 kW at a frequency of 450 kHz, while the lower coil is operated at 15 kW and 300 kHz.

4.4.1.3 Temperature distribution of tandem double-frequency coil ICTP with 12 turns

The number of turns in the lower coil was studied. Figures 4.18(a)–4.18(d) respectively portray the temperature distributions in a tandem double-frequency coil ICTP with 12 turns at gap lengths of 20 mm, 30 mm, 40 mm, and 60 mm. Compared to the temperature distribution in an 8-turn coil in figure 4.14(a), the temperature distribution in a 12-turn coil in figure 4.18(a) at a gap length of 20 mm is axially longer one in terms of high temperature region above 10000 K. Especially, in the lower coil region, the tandem double-frequency coil ICTP with 12 turns has higher temperatures in axial positions of z >200 mm than the tandem double-frequency coil ICTP with 8 turns. With increasing gap length from 20 mm to 40 mm, the high-temperature region in the lower coil region shifts axially downer side in the plasma torch. At gap lengths of 40 mm and 60 mm, the high-temperature region was apparently separated into two parts in the upper coil and the lower coil as portrayed in figure 4.18(d). This separation occurred because the tandem double-frequency coil ICTP is heated both in the upper coil and the lower coil by joule heating independently at different frequencies. Comparison of the temperature distribution in figure 4.18(d) to that in figure 4.14(d) reveals that the high-temperature region in the upper coil is located at almost the same position in the tandem double-frequency ICTP with a 12-turn coil and with a 8-turn coil. This means again that the the ICTP in the upper coil is formed stably independent of the ICTP in the lower coil. On the other hand, the lower coil with 12-turn provides another axially longer high temperature region at more downward position than that with 8-turn.

Figure 4.19 shows the axial temperature distribution at r= 25 mm in 12-turn tandem double-frequency coil ICTP with different gap lengths. The axial temperature in tandem double-frequency coil ICTP of 12 turns with a gap length of 20 mm has a high-temperature region above 11200 K from z=130 mm to z=180 mm. Increasing gap length from 20 mm to 40 mm decreases the temperature around 180 mm < z <210 mm, while it elevates the temperature around z >220 mm. The decreased temperature around 180 mm < z <210 mm arises from decreased power density there because the lower coil is shifted downward. At a gap length of 60 mm, there is a large dip in the temperature around z=200 mm. This is due to the fact that large coils separation makes two separate ICTPs in the torch.

Figure 4.20 depicts the radial temperature distribution of tandem double-frequency coil ICTP with a 12-turn coil at axial position of 230 mm. The tandem double-frequency coil ICTP with a 12-turn coil has a similar radial temperature distribution at gap lengths of 20–60 mm. This temperature is a little higher than those in the tandem double-frequency ICTP with a 8-turn coil in figure 4.16. This is because 12-turn tandem double-frequency coil ICTP can offer the power density just in the lower coil region. The power density distribution by joule heating is displayed in figure 4.21. Combination and configuration of the tandem double-frequency coil can affect the input power density distribution and the temperature distribution. Comparison to figure 4.17 reveals that the high power density region in the lower coil is apparently located more downward separately from the in the upper coil region as the lower coil of 12 turns is positioned in downward region. At a gap length of 60 mm, the two separate high power density region were found so that two separate ICTPs forms there.

In this way, the input power density region and high-temperature region can be controlled by adoption of an adequate coil configuration.

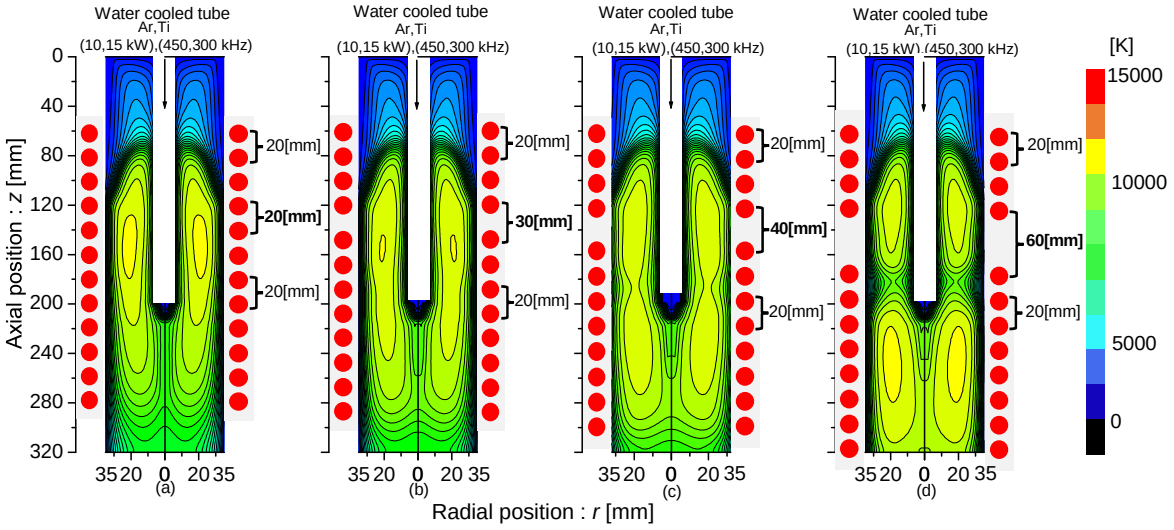

Fig. 4.18: Temperature distribution in Ar-O_2 tandem double-frequency ICTP by a 12-turn coil with Ti powder injection at different gap lengths of (a) 20 mm, (b) 30 mm, (c) 40 mm, and (d) 60 mm. The upper coil is operated at an input power of 10 kW at a frequency of 450 kHz, while the lower coil is operated at 15 kW and 300 kHz.

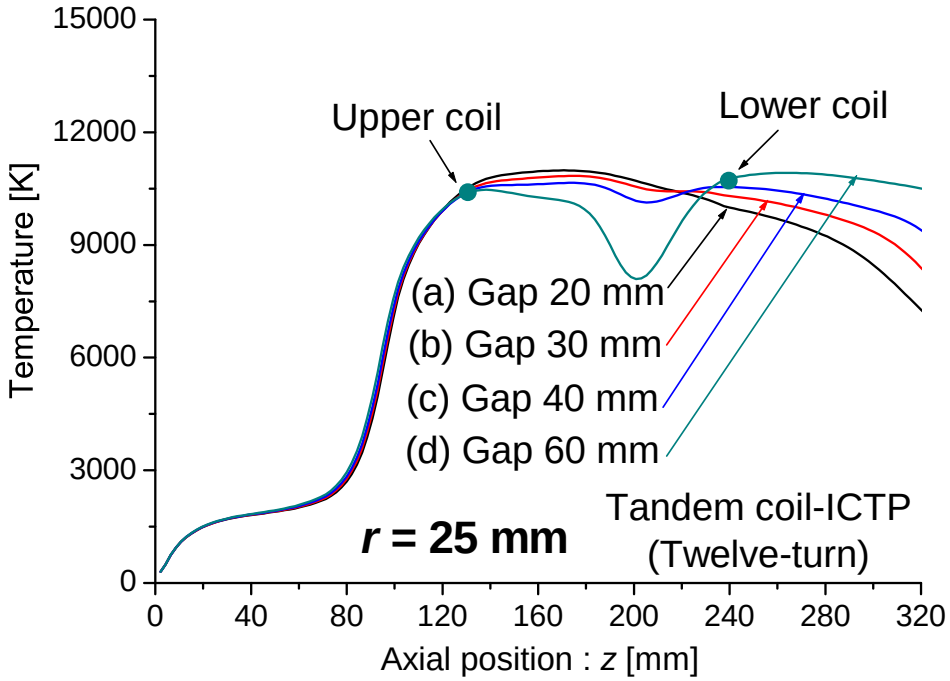

Fig. 4.19: Axial temperature distribution at the radial position of 25 mm in Ar-O_2 tandem double-frequency ICTP by a 12-turn coil with Ti powder injection at different gap lengths of (a) 20 mm, (b) 30 mm, (c) 40 mm, and (d) 60 mm. The upper coil is operated at an input power of 10 kW at a frequency of 450 kHz, while the lower coil is operated at 15 kW and 300 kHz.

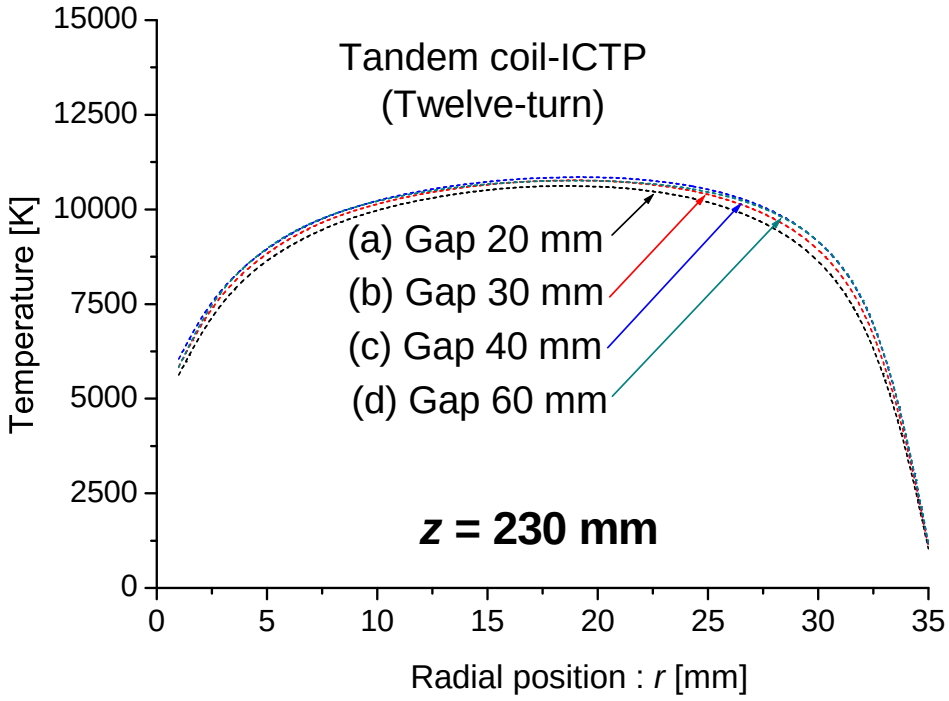

Fig. 4.20: Radial temperature distribution at an axial position of 230 mm in Ar-O_2 tandem double-frequency ICTP by a 12-turn coil with Ti powder injection at different gap lengths of (a) 20 mm, (b) 30 mm, (c) 40 mm, and (d) 60 mm. The upper coil is operated at an input power of 10 kW at a frequency of 450 kHz, while the lower coil is operated at 15 kW and 300 kHz.

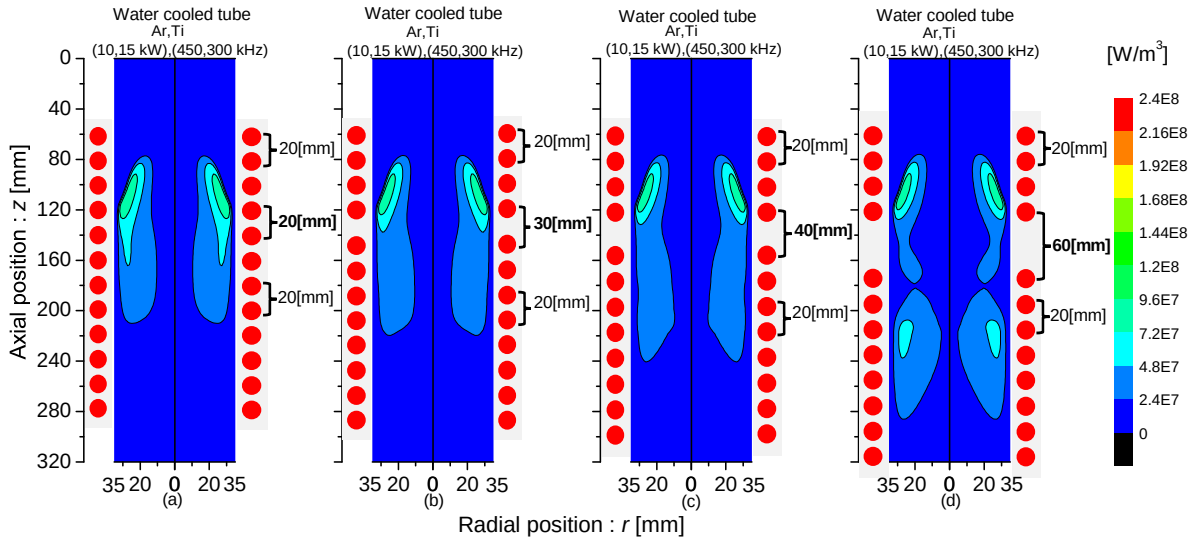

Fig. 4.21: Power density distribution in Ar-O_2 tandem double-frequency ICTP by a 12-turn coil with Ti powder injection at different gap lengths of (a) 20 mm, (b) 30 mm, (c) 40 mm, and (d) 60 mm. The upper coil is operated at an input power of 10 kW at a frequency of 450 kHz, while the lower coil is operated at 15 kW and 300 kHz.

4.4.2 Mass fraction distribution of titanium vapour and gas flow pattern

4.4.2.1 Mass fraction distribution of Ti vapour and gas flow pattern in single-frequency coil ICTP

First, the situation in a single-frequency coil is treated here. The evaporation amount of Ti feedstock and the mass fraction of Ti vapour in the gas phase are influenced by gap length parameters.

Figures 4.22(a)–4.22(d) respectively present the mass fraction distribution of Ti vapour in single-frequency coil ICTP with different gap distances of 20 mm, 30 mm, 40 mm, and 60 mm. As these figures show, the Ti feedstock powder is evaporated to create Ti vapour just below the tip of the water-cooled pipe in the ICTP. The vapour is transported downstream mainly by gas convection with radial diffusion. Moreover, figures 4.22(a)–4.22(c) illustrate that an increase in gap length in single-frequency coil ICTP only insignificantly changes the mass fraction of Ti vapour. Figure 4.22(e) shows the mass fraction of Ti vapour for a 60 mm gap length: it was quite different from those in figures 4.22(a)–4.22(c). Figure 4.22(d) shows that the condition of the gap length of 60 mm offers a higher mass fraction. This point suggests that the evaporation amount of Ti feedstock can be enhanced in single-frequency coil ICTP by a 60 mm gap length. However, gap length of less than 60 mm only slightly affects the mass fraction of Ti vapour, implying that the evaporation amount is elevated only insignificantly.

The plasma flow pattern is influenced by the coil configuration, which transfers Ti vapour in the torch. Figures 4.23(a)–4.23(d) respectively present the streamline inside the single-frequency coil ICTP at different gap lengths of 20 mm, 30 mm, 40 mm, and 60 mm. As might be readily apparent in the streamlines in figure 4.23, a large vortex exists in the upper side region in the plasma torch; then the gas flow bends in the lower coil region because of the Lorentz force. If the gap length is increased from 20 mm to 60 mm, then the gas flow vortex becomes larger. Furthermore, the gas flow bends more strongly in radial direction. This strong bending in the gas flow produces the high-temperature region located closer to the plasma torch axis. This closer high-temperature region on the axis enhances evaporation of Ti feedstock to increase the mass fraction of Ti vapour.

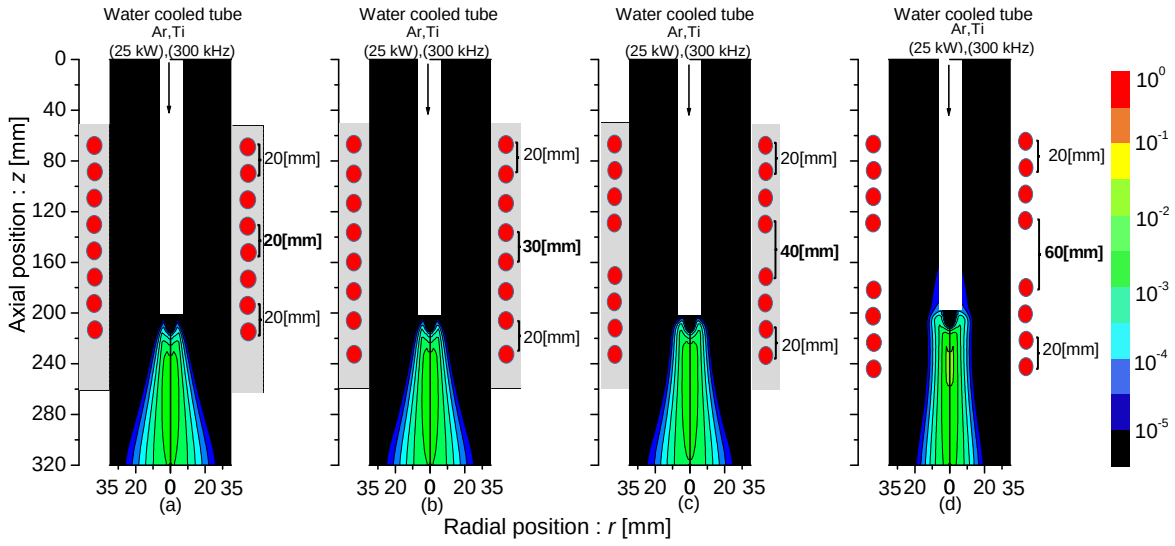

Fig. 4.22: Mass fraction distribution of Ti vapour in Ar-O_2 single-frequency ICTP by an 8-turn coil with Ti powder injection at different gap lengths of (a) 20 mm, (b) 30 mm, (c) 40 mm, and (d) 60 mm. The coil is operated at an input power of 25 kW at a frequency of 450 kHz.

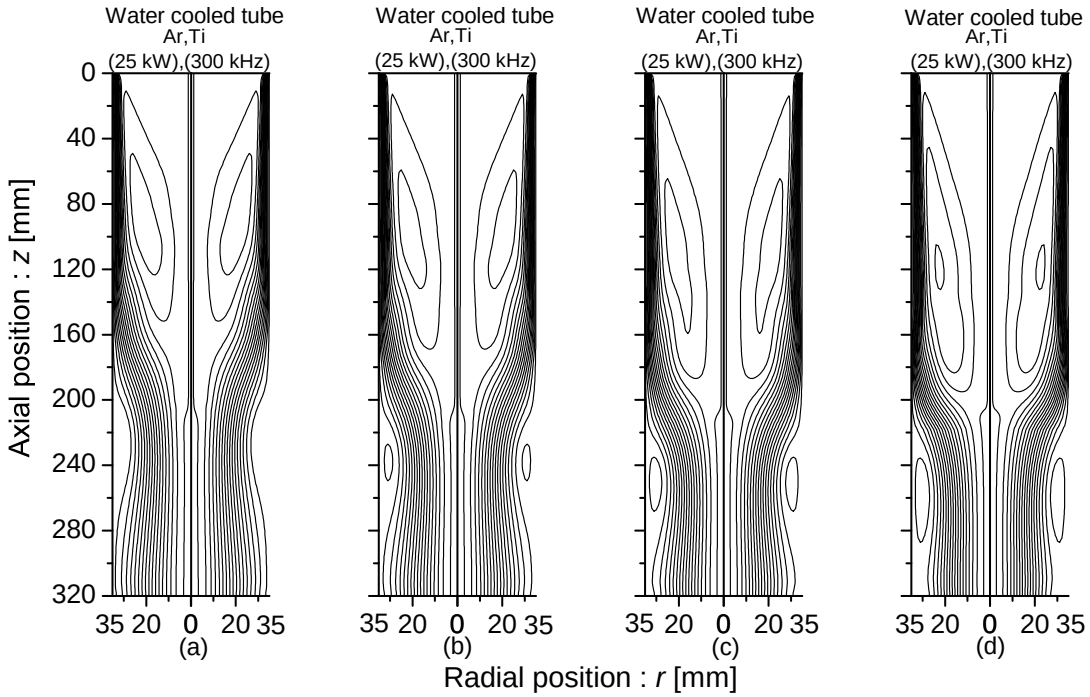

Fig. 4.23: Streamlines in Ar-O_2 single-frequency ICTP by an 8-turn coil with Ti powder injection at different gap lengths of (a) 20 mm, (b) 30 mm, (c) 40 mm, and (d) 60 mm. The coil is operated at an input power of 25 kW at a frequency of 450 kHz.

4.4.2.2 Mass fraction distribution of Ti vapour and gas flow pattern in tandem coil ICTP

For ICTP operated with a tandem double-frequency 8-turn coil, the mass fraction distribution of Ti vapour was calculated under conditions of Ti feedstock powder injection. Figure 4.24 displays the influence of gap length between coils on titanium vapour mass fraction in the tandem double-frequency 8-turn coil ICTP. The gas flow pattern for these ICTP is apparent in figure 4.25. A large difference exists between gas flow patterns for single-frequency coil ICTP in figure 4.23 and for tandem double-frequency coil ICTP in figure 4.25. Single-frequency ICTP in figure 4.10 is established in the lower coil region as one lump at axial positions, while the tandem double-frequency coil ICTP in figure 4.14 forms with axially long shape. This means that tandem double-frequency coil ICTP is formed at upper axial positions compared to single-frequency coil ICTP. Establishment of this tandem double-frequency coil ICTP in the upper coil creates a vortex in the upper region of the torch around axial positions z=10–100 mm, which bends the sheath gas flow in the radial direction by Lorentz force as seen in figure 4.25. In addition, the lower coil current influences the gas flow pattern in downward region of the tandem-ICTP. The gas flows in radial direction to the plasma torch axis at around z=90 mm, and then bends in opposite radial direction to the wall around z=120 mm. The gas flows in radial direction to the plasma torch axis at around z=90 mm is created by Lorentz force arising from the eddy current in the ICTP in the upper coil region. On the other hand, the gas flow in radial direction outward to the wall around z=120 mm is created by pressure gradient from the presence of the ICTP in the lower coil region. The gas flow from the upper region comes to the lower ICTP but it bends avoiding penetration into the lower ICTP. Consequently, around axial position of z=120 mm, the gas flow from the upper coil region has radially outward direction, and then it flows to downward. From this radial outward flow, Ti vapour is transported radially wider in tandem double-frequency coil ICTP in figure 4.24 than in single-frequency coil ICTP in figure 4.22. This indicates that tandem double-frequency coil ICTP is useful to transport Ti vapour in a wider and extended radial region to a downstream reaction chamber. This extention of Ti vapour is enhanced by gap length between the coils from the gas flow pattern. In addition, higher mass fraction of Ti vapour was found at larger gap lengths, indicating that larger amounts of Ti evaporation occurred at

larger gap lengths.

For a 12-turn coil, the mass fraction of Ti vapour and gas flow pattern were calculated in tandem double-frequency coil ICTP. Figures 4.26(a)–4.26(d) respectively show the mass fraction of titanium vapour from evaporation of Ti powder in the tandem double-frequency coil ICTP with 12 turns at gap lengths of 20 mm, 30 mm, 40 mm, and 60 mm. In addition, figures 4.27(a)–4.27(d) respectively portray the gas flow patterns in these cases. As figure 4.27 shows, in a tandem double-frequency coil ICTP with a 12-turn coil, a gas flow bends more strongly than in tandem double-frequency ICTP with an 8-turn coil in figure 4.25. Increasing gap length from 20 mm to 60 mm no changes bending position of the streamline outward in the radial direction around z=120–160 mm. At 60 mm gap length, at around z=220 mm, the gas flow has a radial component that is inward again because of the existence of Lorentz force in the ICTP in the lower coil region. On the other hand, the mass fraction of Ti vapour is similarly distributed around the torch axis for 12-turn coil with gap lengths of 20–40 mm, with 0.02 mass fraction as a peak. This value of mass fraction shows higher density Ti vapour can be created by using 12-turn tandem coil ICTPs.

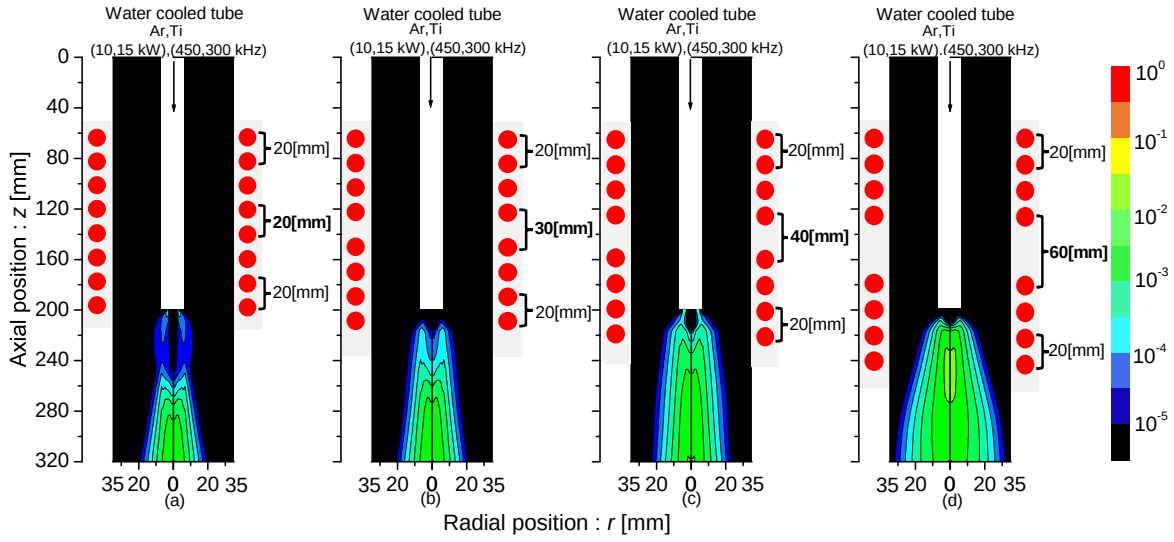

Fig. 4.24: Mass fraction distribution of Ti vapour in Ar-O_2 tandem double-frequency ICTP by an 8-turn coil with Ti powder injection at different gap lengths of (a) 20 mm, (b) 30 mm, (c) 40 mm, and (d) 60 mm. The upper coil is operated at an input power of 10 kW at a frequency of 450 kHz, while the lower coil is operated at 15 kW and 300 kHz.

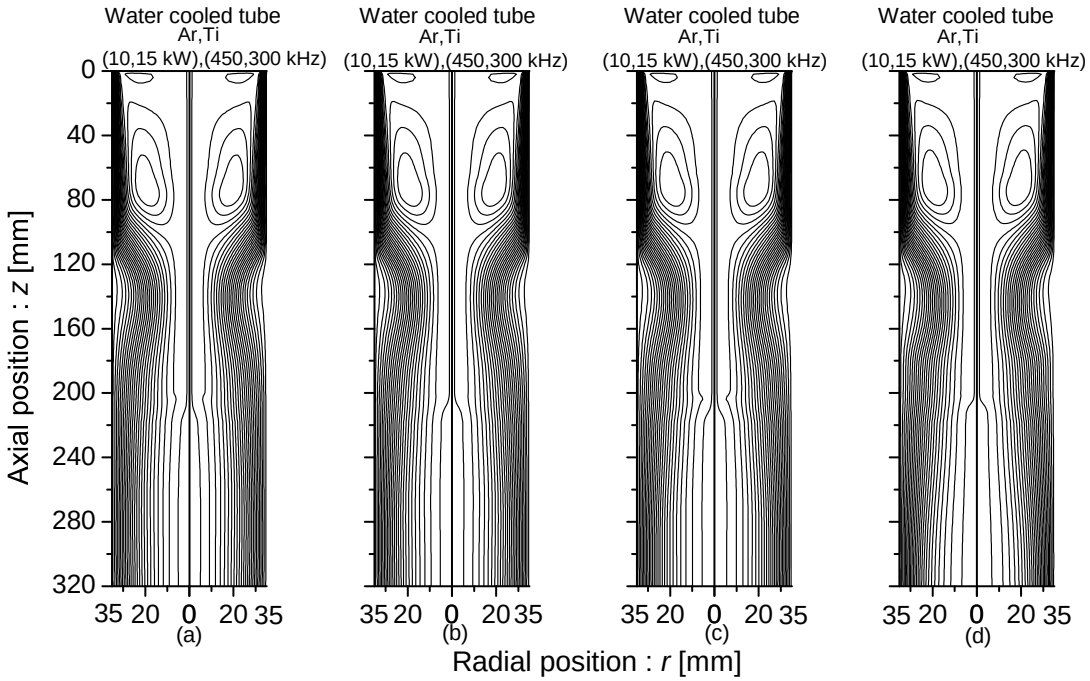

Fig. 4.25: Streamlines in Ar-O_2 tandem double-frequency ICTP by an 8-turn coil with Ti powder injection at different gap lengths of (a) 20 mm, (b) 30 mm, (c) 40 mm, and (d) 60 mm. The upper coil is operated at an input power of 10 kW at a frequency of 450 kHz, while the lower coil is operated at 15 kW and 300 kHz.

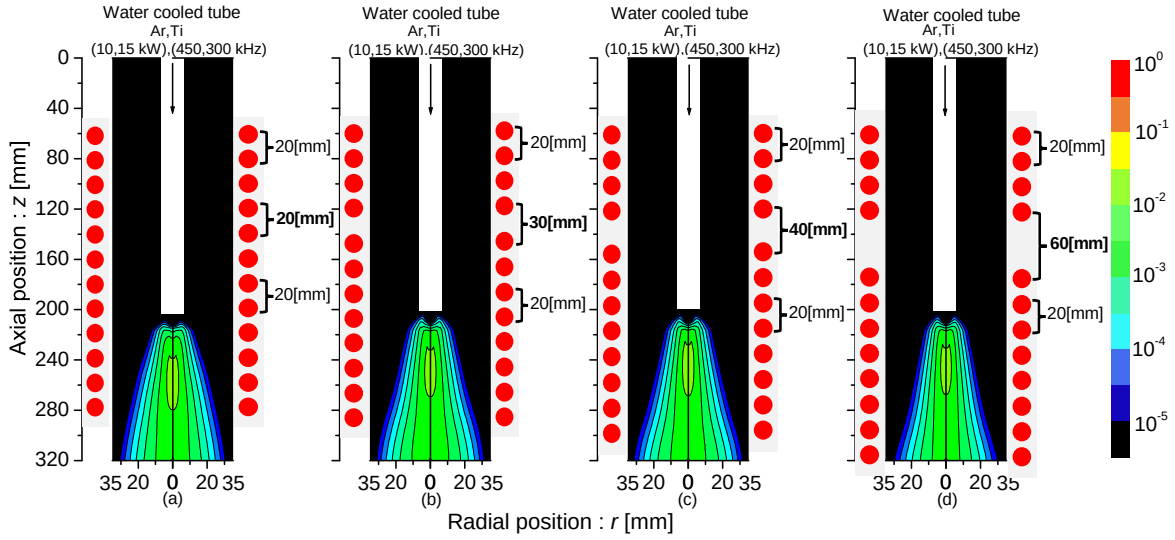

Fig. 4.26: Mass fraction distribution of Ti vapour in Ar-O_2 tandem double-frequency ICTP by a 12-turn coil with Ti powder injection at different gap lengths of (a) 20 mm, (b) 30 mm, (c) 40 mm, and (d) 60 mm. The upper coil is operated at an input power of 10 kW at a frequency of 450 kHz, while the lower coil is operated at 15 kW and 300 kHz.

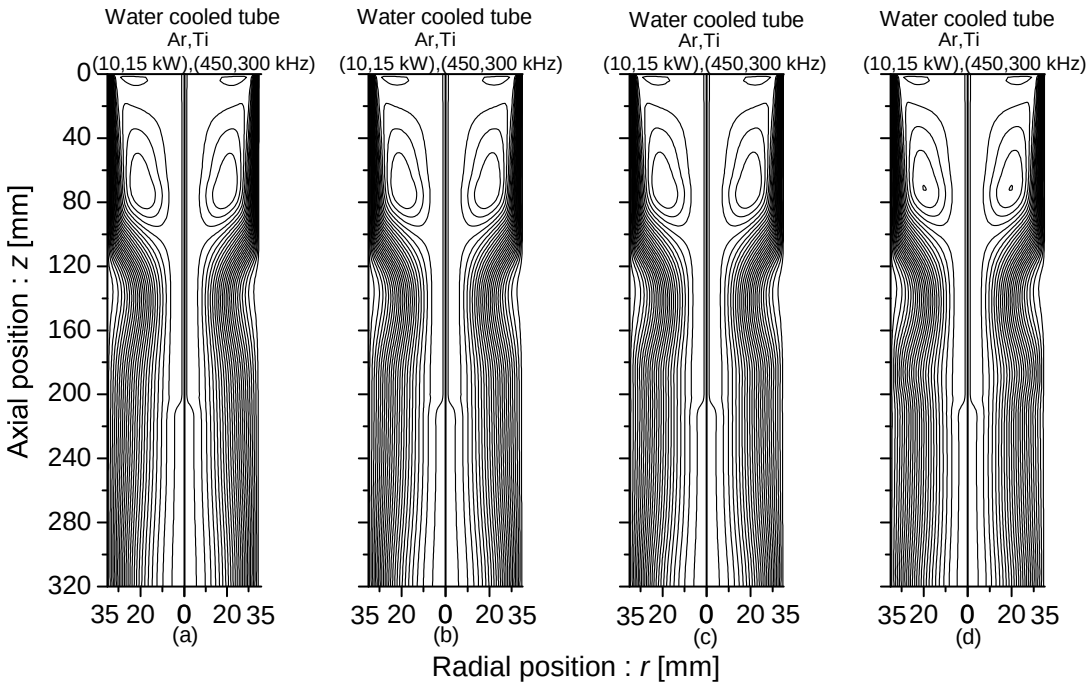

Fig. 4.27: Streamlines in Ar-O_2 tandem double-frequency ICTP by an 12-turn coil with Ti powder injection at different gap lengths of (a) 20 mm, (b) 30 mm, (c) 40 mm, and (d) 60 mm. The upper coil is operated at an input power of 10 kW at a frequency of 450 kHz, while the lower coil is operated at 15 kW and 300 kHz.

4.4.3 Particle behaviour

This behaviour of Ti feedstock particles injected into the ICTP must be calculated considering that the particles are heated, molten, and evaporated through their motion. Moreover, the particle diameter decreases with time and position during the evaporation process. Figure 4.29 presents variations in the diameters of 35 particles as a function of axial position in single-frequency ICTP with an 8-turn coil at a gap length of 60 mm. Behaviours of 35 particles indicated in figure 4.4 were calculated for 7 diameters and 5 initial positions of injected particle for statistical study. In this figure, behaviour of particles at different initial positions were distinguished by different colors: particle behaviour at a radial initial position of r =0.3 mm is denoted by black curves, 0.6 mm by red curves, 0.9 mm by blue curves, 1.2 mm by pink curves, and 1.5 mm by green curves, respectively. Also, feedstock powder was assumed to consist of particles with seven discrete diameters, as presented in the lower panel in figure 4.4.

Figure 4.29 shows that the particle diameters do not change in axial position to 225 mm because all particles are present without evaporatoin inside the water-cooled pipe. From the axial position of 225 mm, the particles start flying into the ICTP. Then they are heated by the ICTP. After some heating during their flight, the Ti particles have decreased diameter due to evaporation. Because the particles are strongly heated from the ICTP, their particle diameter decreases rapidly to 0.25 μm, resulting in generation of Ti vapour into the ICTP. As this figure shows, all particles at 5 initial positions with 7 initial diameters are evaporated completely until the axial position of 300 mm.

Figure 4.28 depicts the temperature variation at each shell inside one particle in single-frequency ICTP with an 8-turn coil at a gap length of 60 mm. Some curves show temperature variation for eight shells inside one Ti particle with initial diameter of 4 μm. The most outer shell of the Ti particle has rising temperature rapidly after particle ejection. After the temperature reaches the melting temperature of the titanium materials of 1953 K, melting occurs maintaining the temperature at 1953 K. This melting involves the liquid phase fraction in the shell increased during melting. During these processes, the heat is transported from the outer side to the inner side of the particle by thermal conduction to increase the interior temperature of the particle. After the liquid fraction of each shell reaches unity, the shell temperature is again increased rapidly. After the temperature

reaches the evaporation/ boiling temperature of 3535 K, particles are evaporated. In this case, evaporation finished at the axial position of 300 mm.

If tandem double-frequency coil ICTP is used, then particle evaporation is changed from cases of single-frequency coil ICTP. Figure 4.30 presents the diameter variation of Ti particles in tandem double-frequency ICTP by 8-turn coils with 60 mm gap length. Some Ti particles in tandem double-frequency coil ICTP are evaporated completely, but some are incompletely evaporated inside the torch. This is because the tandem double-frequency coil ICTP disperses input power density in the upper coil region and in the lower coil region. For evaporation, 12-turn tandem double-frequency coil ICTP may be useful. Figure 4.31 shows the particle diameter variation in 12-turn tandem double-frequency coil ICTP. Apparently, the diameter for all the particles injected decreases to 0 μm inside the torch, showing complete evaporation. It is noted that tandem double-frequency coil ICTP has one ICTP in the upper coil region for stable operation, and another ICTP in the lower coil region for evaporation of feedstock. The above result implies again that tandem double-frequency coil ICTP provides a temperature field that is favourable for evaporation while maintaining ICTP in the upper region of the plasma torch for stable operation.

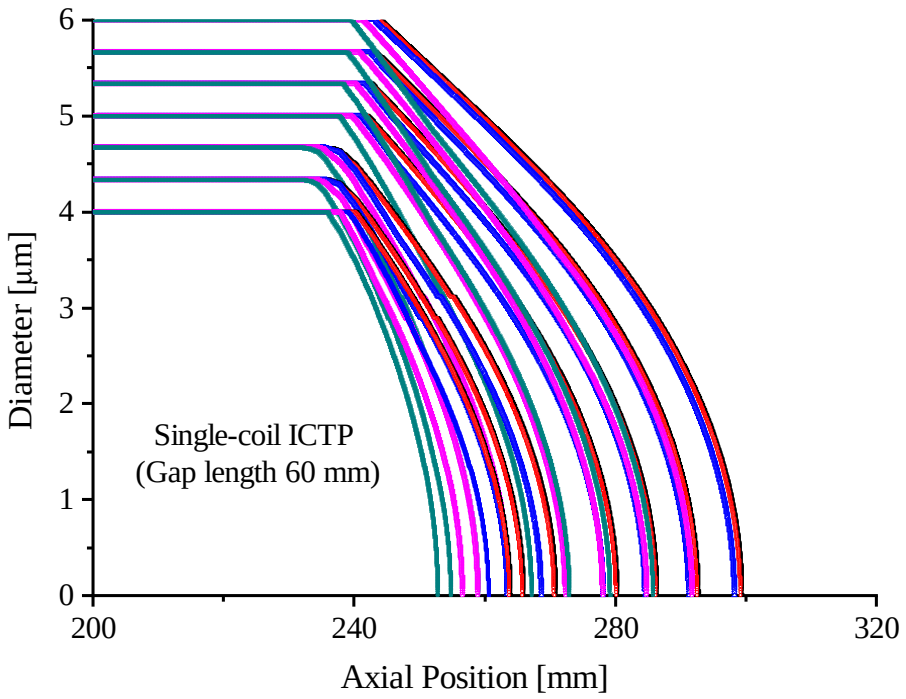

Fig. 4.28: Variation in diameters of 35 Ti particles in Ar-O_2 single-frequency ICTP by an 8-turn coil with 60 mm gap length.

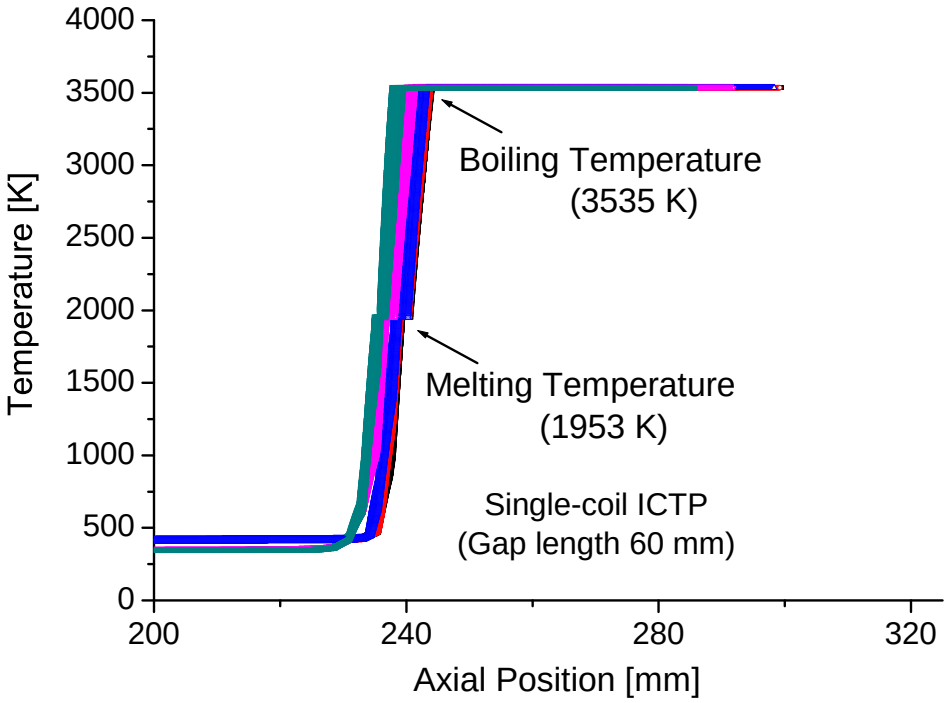

Fig. 4.29: Temperature history of Ar-O_2 in single-frequency coil ICTP with 60 mm gap length.

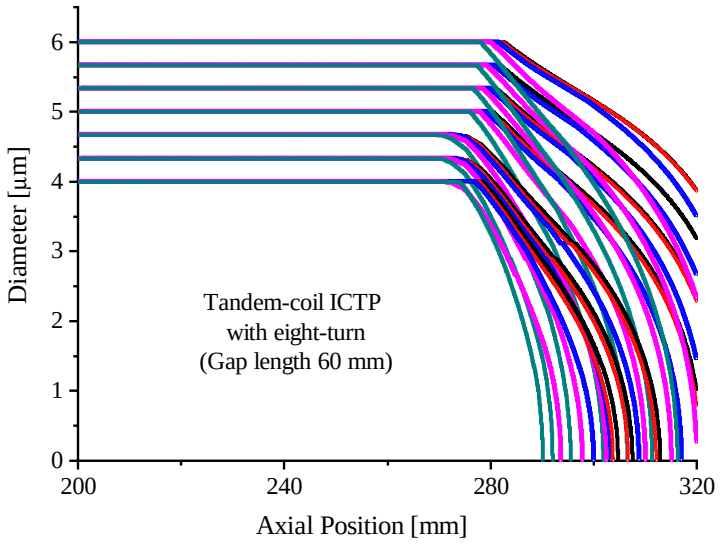

Fig. 4.30: Variation in diameters of 35 Ti particles in Ar-O_2 tandem double-frequency ICTP by an 8-turn coil with 60 mm gap length.

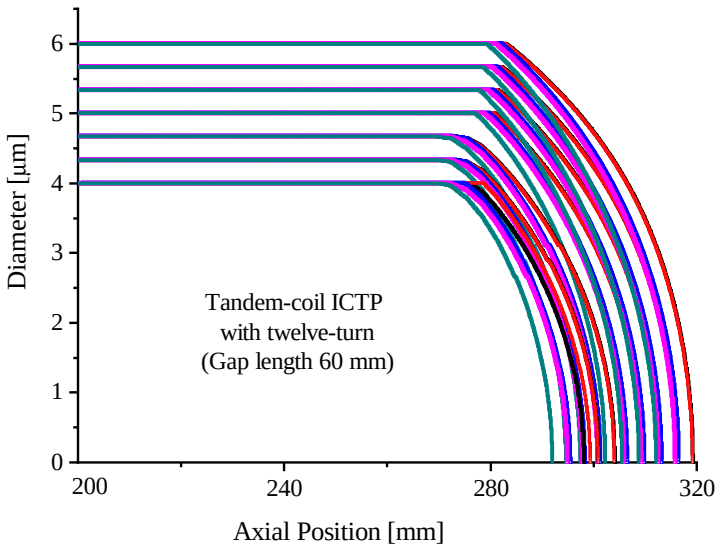

Fig. 4.31: Variation in diameters of 35 Ti particles in Ar-O_2 tandem double-frequency ICTP by 12-turn coil with 60 mm gap length.

4.5 Summary of chapter 4

As described herein, temperature and gas flow fields were calculated numerically for tandem-type inductively coupled thermal plasma (tandem ICTP). Tandem ICTP is established by two coil currents (upper coil and lower coil) in one plasma torch, which had been developed already for nanoparticle synthesis. The temperature distribution of the tandem ICTP and evaporation of feedstock Ti powder were obtained for different gap lengths between the upper and lower coil and coil turn numbers. Results show that increased gap length between the upper and lower coil produces two high-temperature areas that can be controlled separately in tandem ICTP. This result suggests that tandem ICTP provides a temperature field that is favourable for evaporation while maintaining ICTP in the upper region of the plasma torch for stable operation. This favourable temperature field is anticipated as one benefit of tandem ICTP beyond those provided by single-frequency ICTP.

References

[1] J. O. Berghaus, J. L. Meunier, and F. Gitzhofer : "Monitoring and control of RF thermal plasma diamond deposition via substrate biasing" *Meas Sci Technol* **15** pp. 161–4 (2010)

[2] S. Matsumoto, M. Hino, and T. Kobayashi : "Synthesis of diamond films in a rf induction thermal plasma" *Appl Phys Lett* **51** pp. 737–9 (1987)

[3] J. D. Pedersen, H. J. Esposito, and K. S. Teh : "Direct synthesis and characterization of optically transparent conformal zinc oxide nanocrystalline thin films by rapid thermal plasma CVD" *Nanoscale Res Lett* **6**(568) pp. 1–12 (2011)

[4] G. Nutsch : "Atmospheric induction plasma spraying" *High Temp Mater Processes* **15** pp. 61–74 (2011)

[5] K. Shinoda, Y. Kojima, and T. Yoshida : "In situ measurement system for deformation and solidification phenomena of yttria-stabilized zirconia droplets impinging on quartz glass substrate under plasma-spraying conditions" *J Thermal Spray Technol* **14**(4) pp. 511–7 (2005)

[6] H. Tanaka, T. Osawa, Y. Moriyoshi, M. Kurihara, S. Maruyama, and T. Ishigaki : "Improvement of the anode performance of graphite particles through surface modification in RF thermal plasma" *Thin Solid Films* **457** pp. 209–16 (2004)

[7] S. Choi, J. Matsuo, and T. Watanabe : "Synthesis of AlB_{12} and YB_{66} nanoparticles by RF thermal plasmas" *J Phys: Conf Ser* **441** pp. 012030 (2013)

[8] V. Colombo, E. Ghedini, M. Gherardi, and P. Sanibondi : "Evaluation of precursor evaporation in Si nanoparticle synthesis by inductively coupled thermal plasmas" *Plasma Sources Sci & Technol* **22** pp. 035010 (2013)

[9] V. Colombo, E. Ghedini, M. Gherardi, and P. Sanibondi : "Modelling for the optimization of the reaction chamber in silicon nanoparticle synthesis by a radio-frequency induction thermal" plasma *Plasma Sources Sci & Technol* **21** pp. 055007 (2012)

[10] R. Pristavita, N. Y. Mendoza-Gonzalez, J. L. Meunier, and D. Berk : "Carbon nanoparticle production by inductively coupled thermal plasmas: Controlling the thermal history of particle nucleation" *Plasma Chem & Plasma Process* **31** pp. 851–66 (2011)

[11] M. Shigeta and T. Watanabe : "Growth model of binary alloy nanopowders for thermal plasma synthesis" *J Appl Phys* **108** pp. 043306 (2010)

[12] J. G. Li, M. Ikeda, R. Ye, Y. Moriyoshi and T. Ishigaki : "Control of particle size and phase formation of TiO_2 nanoparticles synthesized in RF induction plasma" *J Phys D: Appl Phys* **40** pp. 2348–53 (2007)

[13] Y. Alinejad, N. Faucheuxa, and G. Soucyb : "Preosteoblasts behavior in contact with single-walled carbon nanotubes synthesized by radio frequency induction thermal plasma using various catalysts" *J Appl Toxicology* **33** pp. 1143–55 (2013)

[14] A. Shahverdi and G. Soucy : "Thermogravimetric analysis of single-walled carbon nanotubes synthesized by induction thermal plasma" *J. Thermal Analysis & Calorimetry* **110** pp. 1079–85 (2012)

[15] J. Szepvolgyi, Z. Markovic, B. Todorovic-Markovic, Z. Nikolic, I. Mohai, Z. Farkas, M. Toth, E. Kovats, P. Scheier, S. Feil : "Effects of precursors and plasma parameters on fullerene synthesis in RF thermal plasma reactor" *Plasma Chem & Plasma Process* **26** pp. 597–608 (2006)

[16] C. Wang, A. Inazaki, T. Shirai, Y. Tanaka, T. Sakuta, H. Takikawa, and H. Matsuo : "Effect of ambient gas and pressure on fullerene synthesis in induction thermal plasma" *Thin Solid Films* **425** pp. 41–8 (2003)

[17] T. Uesugi, O. Nakamura, T. Yoshida, and K. Akashi : "A tandem radio-frequency plasma torch" *J Appl Phys* **64** pp. 3874 (1988)

[18] St. Kolev , A. Shivarova, Kh. Tarnev, and Ts. Tsankov : "2D fluid-plasma model of a tandem-type plasma source" *J Phys: Conf Series* **113** pp. 012011 (2008)

[19] W. Li, R. Yang, J. Zheng, and X. Li : "Tandem plasma reactions for Sn/C composites with tunable structure and high reversible lithium storage capacity" *Nano Energy* **2** pp. 1314–21 (2013)

[20] D. Bernardi, V. Colombo, E. Ghedini, and A. Mentrelli : "Numerical simulation for the characterization of operating conditions of RF-RF hybrid plasma torches" *Eur. Phys. J. D* **28** pp. 399-422 (2004)

[21] K. Kuraishi, M. Akao, Y. Tanaka, Y. Uesugi, and T. Ishijima : "Temperature Behavior in a Tandem Type of Modulated Induction Thermal Plasma for Materials Processing" *J Phys: Conf Series* **441** pp. 012016 (2013)

[22] Y. Tanaka and T. Sakuta : "Investigation of plasma-quenching efficiency of various gases using induction thermal plasma technique: effect of various gas injection on Ar thermal ICP" *J Phys D: Appl Phys* **35** pp. 2149–58 (2002)

[23] Y. Tanaka, Y. Takeuchi, T. Sakuyama, Y. Uesugi, S. Kaneko and S. Okabe : "Numerical and experimental investigations of thermal interaction between thermal plasma and solid polymer powders using induction thermal plasma technique" *J Phys D: Appl Phys* **41** pp. 025203 (2007)

[24] Y. Takeuchi, Y. Tanaka, Y. Uesugi, S. Kaneko and S. Okabe : "Numerical simulation of thermal interaction between polymer and Ar induction thermal plasma" *Trans IEEJ* **127-PE** pp. 739–46 (2007)

[25] Y. Siregar, Y. Tanaka, T. Ishijima and Y. Uesugi : "Influence of sheath gas flow rate in Ar induction thermal plasma with Ti powder injection on the plasma temperature by numerical calculation" *MATEC Web of Conf* **218** pp. 043 (2018)

[26] C. T. Crowe, M. P. Sharma and D. E. Stock : "The particle source in cell (PSI-Cell) model for gas droplet flows" *J Fluids Eng* **99** pp. 325–32 (1977)

[27] P. Proulx, J. Mostaghimi and M. I. Boulos : "Plasma-particle interaction effects in induction plasma modeling under dense loading conditions" *Int J Heat Mass Transfer* **28** pp. 1327–36 (1985)

[28] P. Proulx, J. Mostaghimi and M. I. Boulos : "Heating of powder in an r.f. inductively coupled plasma under dense loading conditions" *Plasma Chem Plasma Process* **7** pp. 29–52 (1987)

[29] M. I. Boulos, P. Fauchais and E. Pfender : "Thermal Plasma Fundamentals and Applications vol. 1" *Plenum Press* **7** pp. 366–9 (1994)

[30] J. M. Yos : "Transport properties of nitrogen, hydrogen, oxygen and air to 30 000 K" *AVCO Technical Memorandum RAD-TM* **63** pp. 7 (1963)

[31] S. Chapman and T. G. Cowling : "The Mathematical Theory of Non-Uniform Gases Third Edition" *Cambridge University Press* (1970)

[32] Y. Tanaka, N. Yamachi, S. Matsumoto, S. Kaneko, S. Okabe, M. Shibuya : Thermodynamic and transport properties of CO_2, CO_2-O_2 and CO_2-H_2 mixtures at temperatures of 300-30000 K and at pressures of 0.1-10 MPa *Electr. Eng. in Japan* **163** pp. 18-29 (2008)

[33] A. A. Abrahamson : "Born-Mayr-type interatomic potential for neutral ground-state atoms with Z=2 to Z=105" *Phys. Rev.* **178** pp. 76-79 (1969)

[34] L. Monchick : "Collision integrals for the exponential repulsive potential" *Phys. Fluids* **2** pp. 695–700 (1959)

[35] J. O. Hirschfelder, C. F. Curtiss, R. B. Bird : *Molecular Theory of Gases and Liquids* p 168 John Willey and Sons (1968)

[36] D. Rapp and W. E. Francis : "Charge exchange between gaseous ions and atoms" *J. Chem. Phys* **37** pp. 2613–45 (1962)

[37] R. Nenpyo : "Chronological Scientific Tables National Astronomical Observatory of Japan, Maruzen Co., Ltd" (2010).

Chapter 5

Conclusions

5.1 Introduction

In this thesis, the high-pressure and high-power inductively coupled thermal plasma (ICTP) is widely used as a chemical reaction source and an effective heat source for various materials processing. One benefit of the ICTP can offer a clean thermal plasma field without contamination because it is an electrode-less discharge. Another benefit of the ICTP in materials processing is that such an ICTP can provide a one-step direct processing including rapid evaporation of injected raw materials and then rapid cooling of evaporated materials. In light of these benefits, ICTP has been adopted recently for nanomaterial syntheses for materials.

In this work, the ICTP is usually established by a single coil located around the plasma torch. To this plasma torch, feedstock powder is injected to the high-temperature field, thereby causing its evaporation. The evaporated materials are subsequently cooled to achieve nucleation and thereafter to synthesize nanomaterials. During these processes, the ICTP sometimes becomes unstable because of disturbance from heavy-load injection of feedstock powder. In the worst case, the ICTP can be extinguished by an overly heavy-load injection of feedstock powder. In this chapter, the results derived in this thesis are briefly summarized as following sections.

5.2 Summary of results

5.2.1 Influence of input power in Ar/H_2 thermal plasma with Si powder by simulation

In this chapter, High-power and high-pressure inductively coupled thermal plasma (ICTP) has been widely used for various materials processing. The ICTP can be a sufficient heat and chemical source to various materials processing with no contamination. In addition, the ICTP gives one-step direct processing with rapid evaporation of injected raw materials and also rapid cooling of evaporated materials. The rapid cooling of evaporated material can enhance nucleation of vapor and produce nanoparticles in metastable phase or a non-equilibrium during nanoparticle synthesis with input power by numerical simulation. In this work, we studied the influence of input power on thermal interactions between 99% Ar+1%H_2 ICTP and silicon (Si) feedstock powder injection. The input power was set to three values of 20 kW, 30 kW, and 40 kW. This numerical calculation research was made to obtain temperature field and gas flow field and evaporated mass fraction from very complicated interactions between thermal plasma and particle injection, which cannot be understood only by experiments. Results indicated that higher input power increases the temperature of the thermal plasma but it slightly enhances evaporation of the powder at the center axis of the plasma torch.

5.2.2 Numerical Parametric Investigation on Temperature Distribution in Ar/O_2 Induction Thermal Plasmas with Ti Powder Injection-Inclusion of Particle Evaporation-

In this chapter, The inductively coupled thermal plasma (ICTP) simulation was made for 90%Ar-10%O_2 ICTP with Ti powder injection and Ti powder is used for TiO_2 nanoparticle synthesis. Inclusion of O_2 in Ar ICTP elevates the enthalpy, which may increase the evaporation of Ti powder. The thermal plasma temperature field is much influenced by many physical parameters such as input power, sheath gas flow rate and also Ti powder feeding rate. Here, we researched influences of these physical parameters on the thermal

plasma temperature field and gas flow field. From the reference condition, only one condition was changed to study the influence of specified parameter on the thermal plasma temperature field. . As a result, the temperature distribution can be affected by these operation parameters. Increasing sheath gas flow rate can changes the gas flow velocity and then convective transport of hot region. On the other hand, the feedstock can influence the temperature only on the axis through the evaporation of Ti feedstock and the affected temperature area is small. The input power can change the value and distribution of the temperature in the ICTP but the evaporation amount of Ti feedstock is hardly affected. This is because the ICTP is heated by eddy current on off-axis region. These calculation can provide fundamental data to understand the ICTP field with powder feeding.

5.2.3 Numerical study of temperature and gas flow fields in Ar-O_2 tandem-type inductively coupled thermal plasma with Ti feedstock powder injection

This chapter describes about the tandem ICTP in Ar, O_2 and Ti powder injection with Influences of the coil turn numbers and the gap length between the two coils. For this calculation, we have two condition about configuration of ICTP. One condition is that in which two separate coils in one plasma torch were connected in series with one power source at a single operating frequency. Thereby, the resulting electromagnetic fields are created with one frequency. This situation is designated herein as a 'single-frequency coil'. The other condition is that in which two separate coils arranged on one plasma torch were connected with two independent power sources at different frequencies. In this case, the resulting electromagnetic fields have two frequency components. This situation is designated herein as 'tandem coil' for clarification. The high-temperature region in the upper coil region is useful for establishment of stable ICTP, whereas the feedstock powder is fed to the lower coil region of the ICTP to evaporate the feedstock powder. This tandem ICTP can be useful for nanoparticle synthesis, for example. Through this study, unique distributions were obtained for the temperature and the feedstock vapour concentration in a tandem ICTP. Results show that increased gap length between the upper and lower coil produces two high-temperature areas that can be controlled separately in tandem ICTP. This result

suggests that tandem ICTP provides a temperature field that is favourable for evaporation while maintaining ICTP in the upper region of the plasma torch for stable operation. This favourable temperature field is anticipated as one benefit of tandem ICTP beyond those provided by single-frequency ICTP.

5.3 Future researches

Nanomaterials receiving great attention in various fields because of their unique characteristics. In this thesis, only Al^{3+}-doped TiO_2 nanoparticle and pure-TiO_2 nanoparticle were treated and synthesized. These nanoparticle has very simple spherical structure and simple crystalline composition. Besides these simple structures, many kinds of nanomaterials have been investigated and studied for various applications. Thus, following topic should be included as future work:

(1) Ar/H_2 and Si powder injection.

In the present work, we numerically investigated on thermal plasma temperature fields and powder evaporation by influence of input power in ICTP. In the future, the simulation for Ar/H_2 and Si powder should make to compare the experimental results, and then factor of drag coefficient is important for calculation.

(2) Ar/O_2 and Ti Powder Injection.

As this developed temperature behaviour in ICTP system is expected not only of particle evaporation process but also other materials processing such as zirconium. It can be conducted with ArO_2- Zr to generate ICTP plasma of ArO_2- Zr for a large-area materials processing. Further more, In the present research, the calculation condition is steady state, for the future is better to use transient calculation..

(3) Ar-O_2 tandem-type ICTP with Ti feedstock powder injection.

As the purpose that mentioned in section 4, this tandem coil ICTP is better use with other material processing such as, Ar/H_2 and Si powder injection and then calculation by influence of input power in upper coil and lower coil for a further temperature behavior and stable operation in plasma torch. Perhaps, these may lead to a new and advance technology for a tandem coil processing using a inductively coupled thermal plasma.